Maximizing the Energy Conversion of a U-Oscillating Water Column in the Low Wave Energy Climate of Gwadar, Pakistan

MSC Thesis

Azeem Ahmed

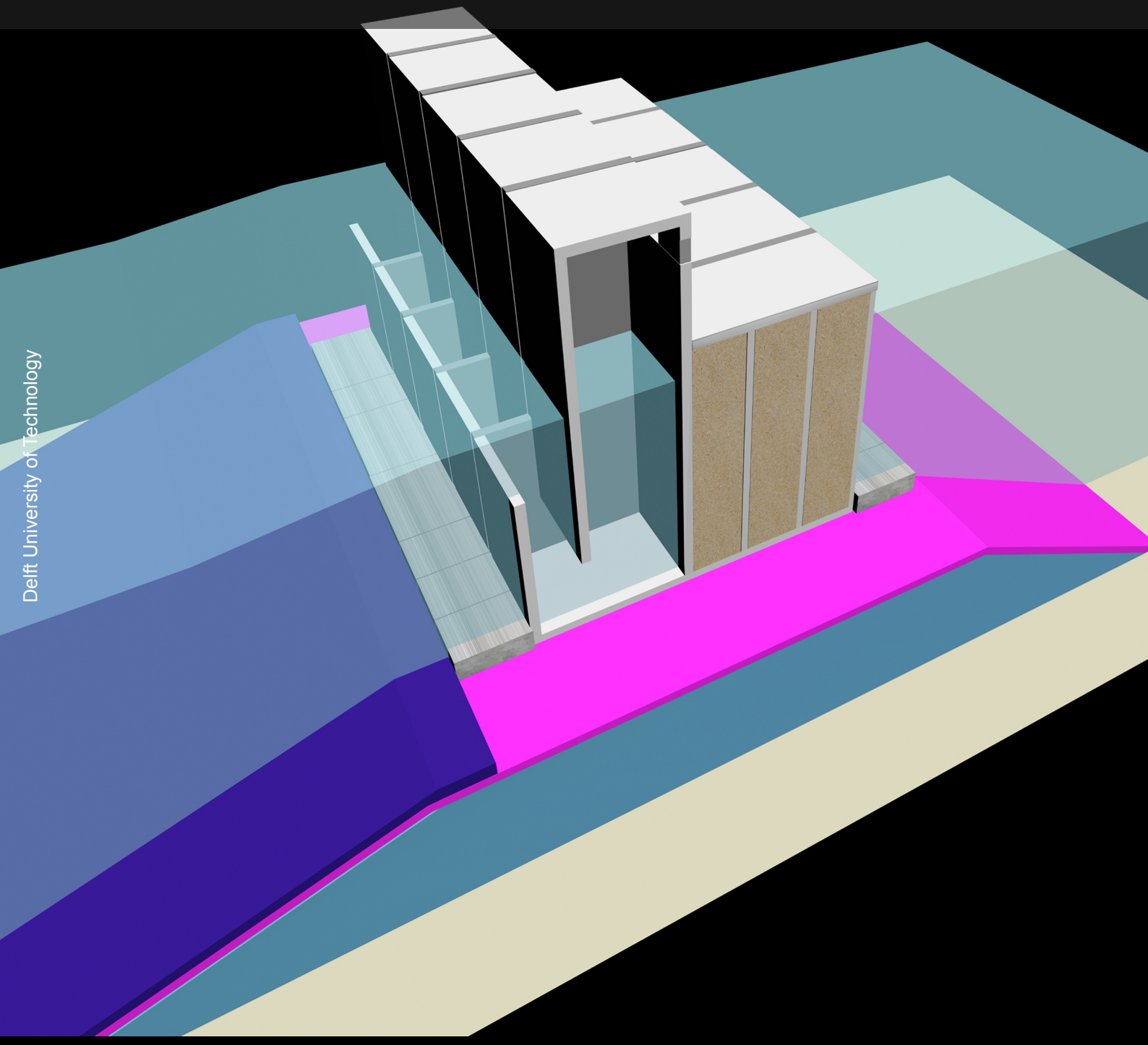

Delft University of Technology

TU Delft

Maximizing the Energy Conversion of a U-Oscillating Water Column in the Low Wave Energy Climate of Gwadar, Pakistan

by

Azeem Ahmed

To obtain the degree of Master of Science in Hydraulic Engineering
at the Delft University of Technology,
to be defended publicly on 9th May, 2022.

Student number: 5145325
Project duration: May 17, 2021 – April 11, 2022
Thesis committee:

Dr.ir, A. Antonini,	TU Delft, Chair
Dr.ir, G. Lavidas	TU Delft, Supervisor
Dr.ir, P. Taneja	TU Delft, Supervisor
Dr.Ir, G. Malara,	Mediterranea University of Reggio Calabria

This thesis is confidential and cannot be made public until 9th May, 2022.

Style: TU Delft Report Style, with modifications by Daan Zwaneveld

An electronic version of this thesis is available at: http://repository.tudelft.nl/.

TU Delft

Acknowledgements

The completion of this report fulfills my last and final requirement to obtain a degree of masters of science in hydraulic engineering at the Delft Institute of Technology. My quest to obtain this degree has not been easy and is best described as jumping over hurdles, with each one taller than the next. Over the course of my journey I have had many stumbles from which I have learned valuable lessons that have helped me to push my self and reach new heights. In this regard, I would like to thank my family for their endless support and encouragement during tough times where self doubt clouded my judgement and no end appeared in sight. In particular, I would like to mention my sister who would always motivate me with her calm and reassuring demeanour, through thick and thin.

This thesis is the largest hurdle I have overcome during my time at Delft and I would like to give credit to my supervising committee that provided me with continuous guidance and technical expertise without which I would stumble. I would like to thank Dr. Alessandro Antonini my chair, for introducing me to relevant researchers and always willing to assist me in a swift and strategic manner. Next, I would like to give special thanks to Dr. Giovanni Malara from the Mediterranea University of Reggio Calabria for his crucial guidance and numerical codes without which this thesis would not be possible. I would also like to thank Dr. George Lavidas for assisting me with SWAN related problems and Dr. Poonam Taneja for useful insights regarding engineering economics. Lastly, I would like to mention my previous employer, in particular Mr. Arif Hussain from the hydrography department for providing me with valuable site information for Gwadar to further my final graduation project. In all, I am very grateful for my time at Delft and even more grateful for the remarkable individuals I have had the opportunity of meeting.

Azeem, Ahmed
Delft, April 2022

Abstract

The purpose of this report is to design a wave energy converter, in particular a U-oscillating water column (U-OWC), to maximize energy conversion in the low wave energy environment of Gwadar, Pakistan. At present Pakistan's 1000km coastline is largely undeveloped and the county is devoid of any wave energy harnessing devices or studies. However, recent years have seen an influx of Chinese investment being made under the China-Pakistan economic corridor agreement, which is stimulus for the near future construction of a large rubble mound breakwater to shelter an assistance vessel basin in the city of Gwadar.

Typically, a WEC is not feasible in low incident wave energy environments because the economic return from minimal energy generation cannot offset the capital cost of the structure. However, the opportunity in Gwadar is unique in the sense that a substantial investment is already envisaged for the creation of a breakwater. Therefore, it is worth investigating if re-designing this structure with vertical caissons embedded with U-OWC chambers is feasible. In this way, the structure can fulfill the dual role of sheltering the assistance vessel basin against wave attack, and produce renewable energy over its design life.

To assist with this task, existing data and methods available in literature along with numerical codes have been utilized. A 10 year SWAN hindcast has been performed, the result of which have been condensed into 60 representative design sea-states on the basis of which the U-OWC chamber geometry and turbine configuration have been optimized. This was achieved by employing a random sampling technique to determine which combinations produce the most power and by identifying the ideal turbine operating revolutions for each sea-state.

Next, the approximate cost of the caisson breakwater integrated with U-OWC chambers is calculated and compared against the currently proposed rubble mound design. It is expected that despite an attempt to maximize the energy generation by the device, its levelized cost of energy will be high, given the low wave energy in the region. Nevertheless, if the design proves cheaper than its rubble mound counterpart, it goes to show that wave energy converter can be deployed in low energy environments provided an opportunity exists where they can be integrated into proposed marine structures. This will be an important finding, considering that the majority of the global coastline is subjected to moderate to low incident wave energy, and neglected from WEC deployment considerations.

Contents

Acknowledgements i

Abstract ii

Nomenclature viii

1 Introduction 1
- 1.1 Background and Scope . . . 2
- 1.2 Motivation and Objective . . . 2
- 1.3 Research Questions . . . 3
- 1.4 Research Method . . . 3
- 1.5 Report Structure . . . 4

2 Wave Energy 5
- 2.1 Theory . . . 5
- 2.2 Wave Energy Converters . . . 6
- 2.3 Levelized Cost of Energy . . . 8

3 Literature Review 10
- 3.1 The Oscillating Water Column . . . 10
- 3.2 Types of Oscillating Water Columns . . . 11
- 3.3 Turbines . . . 14
- 3.4 Case Study . . . 16

4 U-OWC Theory 17
- 4.1 Fundamentals . . . 17
- 4.2 Implementation . . . 21

5 Site Description 23
- 5.1 Gwadar Breakwater . . . 23
- 5.2 Met-Ocean Investigation . . . 25
- 5.3 Data Available . . . 26

6 SWAN Model 29
- 6.1 Model Introduction . . . 29
- 6.2 Model Setup . . . 29
- 6.3 Validation . . . 32
  - 6.3.1 Base Case Simulation . . . 32
  - 6.3.2 SWAN Calibration Runs . . . 34
- 6.4 Results . . . 39

7 Extreme Value Analysis 47
- 7.1 Introduction and Methodology . . . 47
- 7.2 Results . . . 48

8 Tide 52
- 8.1 Tidal Results . . . 52

9 Design of the U-Oscillating Water Column 55
- 9.1 Methodology . . . 55
- 9.2 Geometric Optimization . . . 56
- 9.3 Chamber Coupling and Turbine Optimization . . . 59
- 9.4 Optimization of Submergence . . . 61
- 9.5 Final Power Output . . . 62

9.6 Vertical Breakwater Design 64
9.6.1 Inner Chamber Water Level Fluctuation 65
9.7 Final Design Layout Drawings 66

10 Economics **72**
10.1 Design Cost Comparison 72
10.2 Levelized Cost of Energy and Return on Investment 74

11 Conclusion **77**
11.1 Answers to Research Questions 77
11.2 Future Recommendations 78

A Off-Shore Extreme Value Analysis **80**

B T-Tide Results **84**

C Raw Power Results U-OWC Device **85**

D Design Calculations **90**

E Material Rates and Costing Calculations **101**

References **108**

List of Figures

1.1 Global wave energy resource, taken from [1] . . . 2
1.2 Gwadar coastline satellite image, NASA Earth Observatory . . . 3
1.3 Gwadar port, image courtesy of local consultants . . . 4

2.1 Wave energy flux . . . 5
2.2 WEC possible configurations . . . 7
2.3 Types of WEC's . . . 8

3.1 Generic oscillating water column . . . 11
3.2 Description of oscillating water column energy conversion . . . 11
3.3 Types of OWC's . . . 12
3.4 Comparison of conventional versus U-OWC . . . 13
3.5 Wells turbine schematic [32] . . . 14
3.6 Impulse turbine schematic . . . 15
3.7 Efficiency curve of wells and impulse turbines for normalized non-dimensional flow rate ϕ [23] . . . 15

4.1 Diagram of U-OWC geometric parameters . . . 17
4.2 Basic flow chart of code algorithm . . . 22

5.1 Gwadar site overview . . . 24
5.2 Breakwater options and assistance vessel basin layout, depths taken from GEBCO . . . 25
5.3 Cross section of rubble mound breakwater, re-created based on information provided by local consultants . . . 25
5.4 Met-ocean investigation campaign, instrument deployment locations . . . 26
5.5 ADCP-10m location, plot of Hs and Tm against ECMWF (ERA-5) . . . 27
5.6 ADCP-20m location, plot of Hs and Tm against ECMWF (ERA-5) . . . 27
5.7 Plot of tide gauge data for 1 year . . . 28

6.1 Plot of outer, middle, and inner SWAN computational grids . . . 30
6.2 SWAN model bathymetry . . . 31
6.3 SWAN boundary conditions for wave and wind forcing, outer grid . . . 32
6.4 Base case simulation result plots of SWAN, ADCP, and ECMWF data . . . 33
6.5 Base case simulation scatter plot for 10 and 20m locations, SWAN versus ADCP . . . 34
6.6 Final calibration time series plot for SWAN, ADCP and ERA-5 data . . . 37
6.7 Final calibration scatter plot for SWAN and ADCP data . . . 37
6.8 Variance density spectrum of WESTH minus KOMEN for timestep 2018-10-10 0000HR 39
6.9 SWAN output point(s) location displayed on model bathymetry . . . 40
6.10 Wave roses for offshore and nearshore locations, direction coming from. . . . 41
6.11 Hs plot with direction for time step 2018-07-16 2200 hours . . . 42
6.12 Variation of wave parameters along breakwater alignment . . . 43
6.13 Monthly average distribution of Hs over 10 years (2011-2020) at mid-breakwater location 43
6.14 Monthly average distribution of TM01 over 10 years (2011-2020) at mid-breakwater location 44
6.15 Monthly average distribution of D_m over 10 years (2011-2020) at mid-breakwater location 44
6.16 Year wise total incident wave power (KW/m) at mid-location of breakwater alignment from 2011-2020 . . . 45
6.17 Gwadar wave climate occurrence matrix (2011-2020) . . . 45
6.18 Design sea-states bubble chart plot. . . . 46

7.1 Threshold sensitivity analysis for the near-shore, confidence intervals depicted as lines. 48

7.2 Scatter plot of selected extrema based for the near-shore 49
7.3 Fit of the Generalized Pareto distribution at the near-shore, Hs $>$ 1.9m 50
7.4 Return period and corresponding Hs value for the near-shore. 51

8.1 Plot of the tidal residual, observations subtracted from predicted data. 53
8.2 Joint occurrence probability diagram of tidal amplitude and Hs from 10 year dataset. Here the magnitude is expressed as a probability, all bins add up to 1 54

9.1 Breakwater option-3 alignment 56
9.2 Geometric parameters for U-OWC device 57
9.3 Visual depiction of random sampling technique 57
9.4 Power output (absorbed and converted) for simulated combinations 58
9.5 Capture width ratio (CWR) for coupled air chambers across varying wells turbine diameters 59
9.6 Conversion efficiency for varying rotational speeds across design sea-states 60
9.7 Submergence combinations for h= 1.7, un-submerged conditions correspond to a value of 1 61
9.8 Effect of array length j on q factor 63
9.9 Incident and converted power per chamber (b3 = 4m), for final U-OWC design across 60 design sea-states 64
9.10 Water level fluctuation ζ clearance, dimensions in meters 66
9.11 Water level fluctuation ζ exceedance probability 66
9.12 Final design cross section at 15m depth, dimensions in meters 67
9.13 Final design cross section at 10m depth, dimensions in meters 68
9.14 3d model view 1 69
9.15 3d model view 2 69
9.16 3d model view 3 70
9.17 3d model view 4 70
9.18 3d model view 5 71

10.1 Breakwater section cost with depth, where each section is 4.8m in width. 74
10.2 Sensitivity of LCOE for various OEM cost expressed as a % of the total cost for different discount rates - assuming fixed Design life of 50 years 75
10.3 Sensitivity of LCOE on structure design life for different discount rates - assuming fixed OEM of 2% 75

List of Tables

2.1 Technology readiness levels (TRL's) of various WEC's [19] . . . 8
2.2 LCOE ranges of various energy generation methods listed in units of $/kWh [19] . . . 9

3.1 Kinetic energy swirl loss, diameter, and rotational speed ratios for well and impulse turbine for identical work per unit mass, taken from [23] . . . 15
3.2 Various oscillating water column deployments in the world . . . 16

6.1 Description of SWAN computational grids . . . 30
6.2 Base case simulation calibration coefficients for Hs(m) . . . 33
6.3 Base case simulation calibration coefficients for TM01(s) . . . 34
6.4 ERA5 versus ADCP calibration coefficients for Hs(m) . . . 34
6.5 ERA5 versus ADCP calibration coefficients for TM01(s) . . . 34
6.6 SWAN model calibration performance for various KOMEN c_{ds2} values at the 10m and 20m ADCP location. Value of $c_{ds2} = 0.0000236$ is default . . . 35
6.7 SWAN model calibration performance for JANSSEN at the 10m and 20m ADCP location. Values of $\delta = 0.5$ and $c_{ds1} = 4.5$ are default . . . 36
6.8 SWAN model calibration performance for WESTH (Yan, Alves and Banner) at the 10m and 20m ADCP location. The parameters $c_{ds2} = 0.00005$ and $br = 0.00175$ are default values . . . 36
6.9 Correlation (R) and root mean square error (RMSE) improvement, base case versus final simulation at 10m ADCP location . . . 38
6.10 Correlation (R) and root mean square error (RMSE) improvement, base case versus final simulation at 20m ADCP location . . . 38

7.1 Statistical model performance for a threshold $u = 1.9m$ at the near-shore . . . 49
7.2 Return period and corresponding Hs value at the near-shore . . . 51
7.3 Return period and corresponding Hs value at the off-shore . . . 51

8.1 Tidal harmonic analysis results for 10 primary constituents . . . 53
8.2 Tidal character classification based on form factor F [61] . . . 53

9.1 Range of values for various geometric parameters to be stored in column vectors . . . 57
9.2 Annual energy production for various submergence (h) and duct length values (l_i) . . . 62
9.3 Total U-OWC converted power and energy for north-eastern breakwater segment, Gwadar 63
9.4 Final U-OWC design, device power and efficiency per meter width . . . 63
9.5 Design parameters for U-OWC vertical caisson breakwater . . . 65
9.6 Goda safety factor for design . . . 65
9.7 Layer breakdown of shallow rubble mound foundation . . . 65

10.1 Rubble mound breakwater cost for north-eastern segment, bill of quantity and material rates for the year 2018. . . . 72
10.2 U-OWC caisson breakwater cost for north-eastern segment, bill of quantity and material rates for the year 2018. . . . 73
10.3 Return on Investment for various buy back rates. Buy back rates taken from [68] . . . 76

Nomenclature

Abbreviations

Abbreviation	Definition
WEC	Wave Energy Converter
OWC	Oscillating Water Column
U-OWC	U-Oscillating Water Column
PTO	Power Take-Off System
CAPEX	Capital Expenditure
OPEX	Operating Expenditure
AEP	Annual Energy Production
LCOE	Levelized Cost of Energy
MSL	Mean Sea Level
DWL	Design Water Level
HAT	Highest Astronomical Tide
LAT	Highest Astronomical Tide
RMSE	Root Mean Square Error
SI	Scatter Index
R	Pearson Correlation Coefficient
EI	Extremal Index
NLL	Negative Log Likelihood
AIC	Akaike Information Criterion
BIC	Bayesian Information Criterion
rpm	Revolutions per Minute

Symbols

Symbol	Definition	Unit
J	Wave energy flux	$[w/m^2]$
g	Gravity	$[m/s^2]$
S	Variance density	$[m^2/Hz]$
H_{m0}	Spectral significant wave height	$[m]$
T_e	Energy period	$[s]$
ρ	Density	$[kg/m^3]$
θ	Direction	$[rad]$
ω	Angular frequency	$[rad/s]$
k	Wave number	$[rad/m]$
d	Local water depth	$[m]$
h	Submergence of U-duct	$[m]$
h_c	Air chamber height from MSL	$[m]$
l_i	Length of U-duct	$[m]$
b_1	Outter chamber width	$[m]$
b_2	Inner Chamber width	$[m]$
b_3	Transverse chamber width	$[m]$
ζ	Inner chamber water level fluctuations	$[m]$
D	Turbine diameter	$[m]$
Δp	Net excitation pressure	$[N/m^2]$

Symbol	Definition	Unit
H_∞	Added mass at infinite frequency	$[m]$
$\overline{K}$	Retardation function	$[m/s^2]$
K_w	Duct loss coefficient	[-]
p_c	Air chamber pressure	$[N/m^2]$
p_{atm}	Atmospheric pressure	$[N/m^2]$
$\rho_{c,n}$	Air density of n connected air chambers	$[kg/m^3]$
$V_{c,n}$	Volume of n connected air chambers	$[m^3]$
γ	Specific heat ratio	[-]
N	Rotational speed	$[rad/s]$
ρ_{in}	Stagnation air density	$[kg/m^3]$
R_p	Return period	$[years]$

Notes:

Symbols and definitions for base variables are presented above, remaining variables mentioned in the text can be derived.

Figures presented in this report are the authors illustration, unless indicated otherwise by means of a reference.

1

Introduction

Of the renewable energy sources available, wave energy is described as having the highest potential for development and production amongst all renewables [1]. It can be approximated that the global wave resource is around 2 terawatt [1]. Typically, wave energy converters have been deployed in regions of the world where the energy resource is valued at 25 kW/m or greater [2], however these regions are far and scarce accounting for only 2% of the global 800,000 km shoreline [3] as can be seen in figure 1.1. Their implementation is often preceded by expensive scale model testing involving the complex interaction of multiple systems in an attempt to quantify the output power generated. However, continued advances in computer modelling techniques have made WEC power estimations much more efficient, thereby allowing for the determination of power numbers at the feasibility level with relative ease. This allows for an increased potential for implementation of WEC's around the world, even assessing their feasibility in regions of low incident wave energy with minimal cost, in terms of time and finance.

With climate change on the rise, the push for green energy generation is greater than ever. Energy generation from renewable sources such as wind, solar, tidal, and wave energy, play a pivotal role in the fight against climate change and are increasingly at the centre point of international agreements to de-carbonize [4]. If the path laid out in the Paris agreement is to be followed, 85% of global energy generation will have to be derived from renewable sources by the year 2050 [5].

The assessment and potential for deployment of WEC's across shorelines subject to moderate to low incident wave energy can help increase the global share of renewable energy generation. Traditionally, WEC's have been met with the problem of harnessing energy in an effective and cost efficient manner [1]. However, their feasibility can be drastically improved if they can be integrated into existing or proposed marine structures such as breakwaters. Also, WEC's deployed in environments of higher wave energy are subject to greater wave forces and thus must be designed accordingly which adds to the capital cost of the structure, not to mention the additional issues which may arise in terms of robustness and survivability resulting in increased maintenance costs. For the reasons mentioned above this report will investigate the option of implementing a WEC in a low wave energy environment and assess its feasibility compared to a traditional rubble mound breakwater.

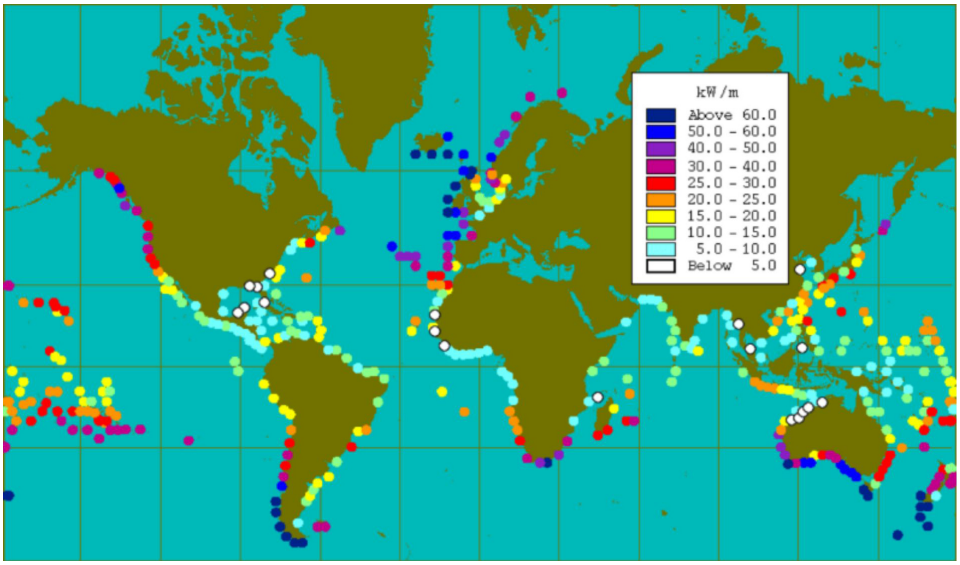

Figure 1.1: Global wave energy resource, taken from [1]

1.1. Background and Scope

Having established the importance of renewables in the near future, the focus of this thesis will be on the feasibility of harvesting wave energy by means of an oscillating water column device (OWC) in the low wave energy climate of Gwadar, Pakistan.

The city of Gwadar is located in Pakistan's Balochistan province in the south-west and can be easily recognized by its iconic tombolo formation that has created an east and west bay as seen in figure 1.2. Having naturally deep and warm waters, Gwadar is home to the third major port of Pakistan depicted in figure 1.3. The city also holds strategic importance from a geographical perspective as it is located at the bottleneck point along the Strait of Hormuz in the Persian Gulf and serves as a critical link for China's maritime silk route [6]

For this reason the Chinese government, under their one belt one road initiative, signed the China-Pakistan Economic Corridor (CPEC) agreement in 2013 [7]. As part of this agreement, a significant expansion of Gwadar port is envisaged which requires the creation of a basin for the berthing of security and assistance vessels. To provide shelter for the basin, the lead consultants have proposed constructing a large rubble mound breakwater with armor units.

This report will investigate at the feasibility level the option of re-designing the breakwater with a U-OWC device harvesting wave energy. By doing so, the breakwater can fulfill a dual role of sheltering the basin against waves and generate renewable electricity over its design life as opposed to a singular function a traditional breakwater would accomplish. An effort will be made to quantify and maximize the power output of the device for the low wave energy climate of Gwadar, and a comparison in terms of cost will be done against the traditional breakwater. Detailed breakwater design including alignment, structure, wave penetration, and geo-technical aspects are beyond the scope of this report.

1.2. Motivation and Objective

Despite having a coastline of about 1000km [8], Pakistan is completely devoid of any wave related renewable energy generation facilities or long term wave climate studies. Although renewable sources do account for a small fraction of the country's power generation, the majority of the 18.54 gigawatts are generated from fossil fuels [9].This reports aims to be the first to investigate the feasibility of harnessing wave energy along the county's coastline, given the low value of the resource, on the order of 5-10 KW/m based on figure 1.1 - subject to further refinement.

For the purpose of this report, the proposed armour unit breakwater suggested by the lead consultants provides an ideal opportunity to assess if re-designing it as a structure with vertical caissons incorporating a U-OWC to generate energy proves to be beneficial or not. Additionally, it is important to mention that the breakwater structure proposed by the lead consultants is long having a length of



Figure 1.2: Gwadar coastline satellite image, NASA Earth Observatory

approximately 1-2 km, and it is of interest to examine if the large capture width that it provides is enough to offset the disadvantage of low incident wave energy in the region.

1.3. Research Questions

While remaining within the scope of this report, the following questions and aspects will be investigated:

- To determine the long term wave statistics for the region and find which sea states contain the most energy along with their frequency of occurrence
- To determine the ideal chamber geometry and power-take-off configuration to maximize annual energy generation of the U-OWC device
- To check if the long breakwater length providing a large capture width is enough to offset the disadvantage of low incident wave energy.
- To quantify the financial cost of the vertical breakwater embedded with a U-OWC
- To determine the LCOE of the device and assess its financial feasibility.

1.4. Research Method

In order to investigate the items mentioned above, relevant met-ocean information indigenous to the region of Gwadar is required. Fortunately, local consultants working along side lead consultants have agreed to share site information for this thesis, solely to be used for academic purposes. The shared information will be used in conjunction with two numerical tools, namely, the SWAN wave model to determine local long term wave statistics and numerical codes developed by Professor Giovanni Malara, a senior marine researcher at the 'Mediterranea' University of Reggio Calabria, to model the power production of the U-OWC device. The financial feasibility stage of the thesis will make use of local material costs provided or mentioned in previous reports of the local consultants, along with information pertaining to interest rates.



Figure 1.3: Gwadar port, image courtesy of local consultants

1.5. Report Structure

The first part of this report will be a literature review followed by the theory of an oscillating water column. After this, an overview will be provided on the information available for Gwadar along with breakwater design plans proposed by the lead consultants. The next stage will be on the development and validation of a SWAN wave model after which the long term wave simulation results will be described. The third stage will focus on the design and power maximization of the U-OWC device leading to the last stage which will describe the financial feasibility of the device and future recommendations.

2

Wave Energy

The primary objective of this section is to introduce the reader to the concept of wave energy and the various devices that have been developed to harness it. Discussed briefly are the common configurations, operating principles, and technological stage of development of wave energy harvesters.

2.1. Theory

A wave can be defined as a disturbance generated by the wind which in turn is driven by thermal differences that arise from incident solar energy [1]. The interaction of the wind with the ocean surface results in the transfer of energy, which coupled with the forces of friction and gravity help to create waves [1]. The waves contain kinetic energy due to the motion of the water particles within them and potential energy from the contribution of work being done against gravity to create crests and troughs [10]. The energy contained in a sea state comprising of irregular waves can be characterized by its spectrum and quantified by the energy flux J in units of W/m which is depicted visually in figure 2.1. A mathematical representation of the wave energy flux is given by equation 2.1[10] and its deep water approximation by equation 2.2 [11]. Here S is the variance density, $\theta 1$ and $\theta 2$ the directional bounds, ρ the density, H_{m0} the spectral significant wave height, g is gravity, and T_e is the energy period which is equal to $0.9T_p$ based on the JONSWAP representation of the spectrum [11] .

$$J = \frac{\rho g^2}{4\pi} \int_0^{\infty} \int_{\theta 1}^{\theta 2} f^{-1} S(f,\theta) cos(\theta - \theta_0) df d\theta \tag{2.1}$$

$$J = \frac{1}{64\pi} \rho g^2 H_{m0}^2 T_e \tag{2.2}$$

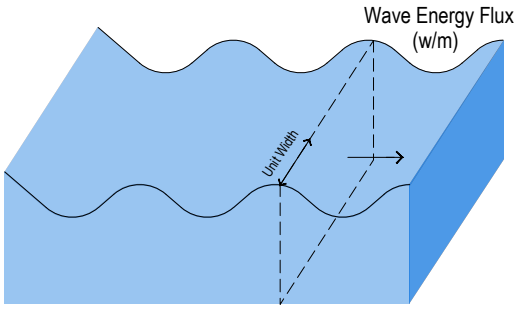

Figure 2.1: Wave energy flux

2.2. Wave Energy Converters

Based on the information presented above, the idea of extracting energy from waves is not a recent one with patents reaching back to the 1960's and numbering over a 1000 [12] for various types of devices. However, despite numerous developments the industry has not been able to converge on a single design which has hindered their commercial development [12]. A few reasons exists for this and they mainly pertain to inefficient extraction of wave energy over continuously varying sea states, survivability issues due to their operation in the harsh marine environment, and the lack of standard procedures in the industry [12]. Listed below are the various benefits and hindrances pertaining to WEC's as mentioned in the work of Drew et al [13]

Advantages

- Ocean waves can be attributed with the highest energy density compared to other renewable energy sources. For instance, waves are generated by winds triggered by thermal differences as a consequence of solar intensities of 0.1-3 KW/m2 of horizontal sea surface. This translates into flow intensities of 2-3 KW/m2 in a vertical plane perpendicular to the wave propagation direction.
- Wave energy transmission can take place across large distances with minimal attenuation. For example, storm energy from the western Atlantic can make its way to the western coast of Europe aided by prevailing westerly winds.
- Reports indicate that wave power generation can take place over 90% of the time which is greater compared to wind and solar energy sources with little to no environmental impacts.

Drawbacks

- Difficulty in converting random and low frequency oscillatory motion of waves, subject to great variability in height, period and direction, into useful motion to drive a turbine and generator.
- Harnessing efficiently the power of irregular waves is a challenge. Often to ensure efficient power conversion the WEC's are tuned for the most frequent sea states. However, the energy converters must also withstand extreme design conditions over their life. This results in unique structural and economic challenges.
- With over a 1000 design patents the industry has a very wide research focus and has not been able to invent the most efficient wave energy harvester.

In general all wave energy converters (WEC's) extract energy from the waves based on the law of conservation. To do so they must interact destructively with the sea waves by generating a wave of their own by displacing water through the movement of their body or by means of an oscillating water column [10]. The destructive interference between the incident wave and WEC results in the maximum energy extraction that can be used to perform mechanical work to spin a turbine and produce energy [10]. The primary components that all wave energy converters share are, a device or mechanism to capture energy, a mooring or structure to keep it in place, a power take-off system comprising of a turbine connected to a generator, and a control system with safety relief valves if necessary [3]. Keeping the following components in minds, WEC's can be identified as a combination of two categories, namely, their configuration and dimensions with respect to the wave ray, and their method of energy extraction. The categories have been described below and are shown in figure 2.2 and 2.3.

WEC Configurations

- **Attenuators (A):** Are WEC's that are oriented in a direction parallel to the wave ray as shown in figure 2.2, and can capture wave energy along a single axis [14]. Theses devices extract energy along their length due to the wave induced water level variations and usually comprise of long multi-segmented structures [14]. The passing of the crest and trough result in a time varying motion of the segments which is converted to mechanical power by means of a power module and hydraulic circuit [14].
- **Point Absorbers (P):** These devices are described as being axis-symmetric as they can harness energy with equal efficiency from all directions [14]. Figure 2.2 shows that their physical dimensions are small compared to the incident wave length to the extent that they are not sensitive to

wave direction [13]. Point absorbers usually operate in isolation and are not connected to one another allowing freedom of movement [14].

- **Terminators (T):** Harness energy by orienting their principal axis perpendicular to the wave ray [13] as seen in figure 2.2. Terminators are direction dependent and most effective at extracting wave energy head on.

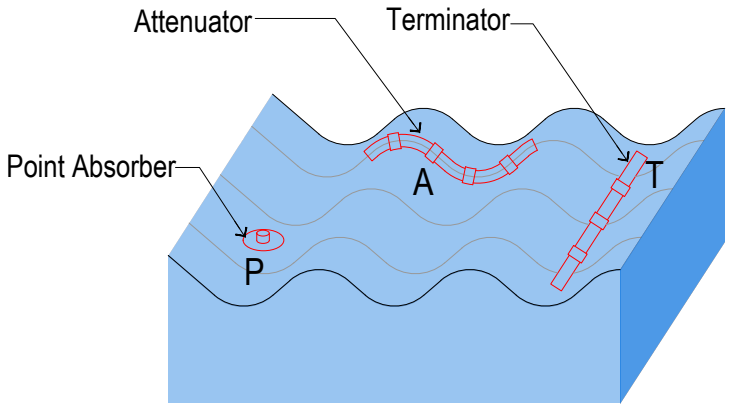

Figure 2.2: WEC possible configurations

WEC Methods of Extraction

- **Wave Overtopping:** Operates on the principle of gathering water due to the overtopping of waves into a reservoir above mean sea level [15]. The collection of the water is facilitated by ramps which face the wave crest and focus it towards the reservoir opening. The static head of the water collected in the reservoir is used to drive it through a turbine connected to a generator for electricity production [15]. Figure 2.3a below depicts the operating principle of a wave overtopping device which may be fixed or floating.
- **Oscillating Water Column:** Comprises of a chamber with a submerged opening facing the sea side, which by the action of wave excitation pressure forces water inside the chamber to alternately compress and dilate a pocket of air creating flow to drive a turbine and generate energy [16]. These devices can be floating or fixed and depicted in figure 2.3b below.
- **Wave Actuated Bodies:** These devices rely on the motion induced by waves to move physical objects in primarily heave, pitch and roll motions [17]. For instance, Wave crests and troughs create a submerged pressure differential which can oscillate a device in the vertical direction, or the horizontally alternating wave particle velocity can be used to rock a hinged deflector back and fourth [13]. Both are examples of wave activated bodies which can be floating or fixed. An example is depicted in figure 2.3c below.

The state of development or maturity of the WEC's mentioned above can be systematically ranked based on the Technology Readiness Levels (TRL) index conceived by NASA [18]. This index comprises of levels from 1 to 9 where level 1 denotes the device is in its infancy and only basic principles have been observed, and level 9 indicates that the device has been successfully deployed at a commercial level multiple times [18]. The table 2.1 below lists the current max TRL's for each category of WEC mentioned.

The performance of wave energy converters can also be defined by the capture width (CW) which is a ratio of absorbed or converted power to that of the incident wave flux J mentioned in section 2.1 [20]. This metric was conceived in 1975 and only quantifies the hydrodynamic performance of

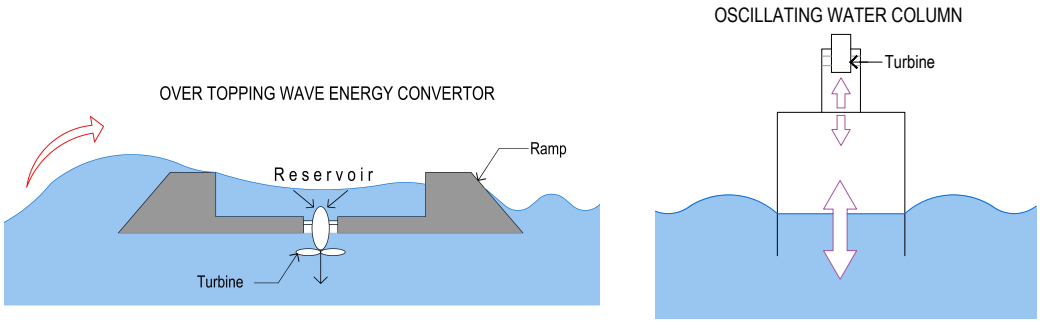

(a) Overtopping Device

(b) Oscillating water column

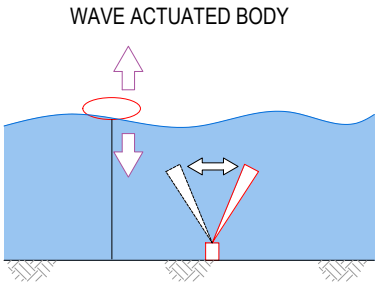

(c) Wave actuated body

Figure 2.3: Types of WEC's

WEC Type	Max TRL	Description
Overtopping Device	5	Component validated in relevant environment
Wave Activated Bodies	7	Device prototype demonstration
Oscillating Water Column	8	Actual device tested and qualified for deployment

Table 2.1: Technology readiness levels (TRL's) of various WEC's [19]

the device [20] but does not say much about the economic performance. Based on well established theory the wave resource increases in deeper water as attenuation from bottom friction and wave breaking are not present. The trade-off between increased wave energy harvesting potential versus cost cannot be generalized in the favor of off-shore installments, instead must be weighed against site and project specific conditions to determine near-shore or off-shore feasibility. Despite lower energy in shallow water, the feasibility of the device can be significantly improved if its costs can be shared by incorporating it into an existing or proposed marine structure. This leads to a useful metric called the levelized cost of energy (LCOE) described in section 2.3 below to assess jointly the power and economic performance of a WEC.

2.3. Levelized Cost of Energy

A metric upon which energy generating technologies such as wave energy converters (WEC's) are assessed is the levelized cost of energy. It can be described as the net present value of the unit cost of electricity produced over the design life of the device, typically in units of $/kWh [21]. The LCOE can be expressed in mathematical terms in equation 2.3, where CAPEX and OPEX are defined as the capital expenditure and the recurring costs, AEP is the annual energy yield with r being the discount rate and N the design life of the device [21].

$$LCOE = \frac{CAPEX + \sum_{t=1}^{N} \frac{OPEX^t}{(1+r)^t}}{\sum_{t=1}^{N} \frac{AEP_t}{(1+r)^t}} \tag{2.3}$$

The LCOE can be significantly influenced by the magnitude of the wave energy farm due to the

economies of scale effect [21]. Generally, the larger the rated power output of the project, the lower the installation costs due to factors such as cost sharing during construction and discounts from various manufacturers due to the bulk purchasing of components. Listed in table 2.2 are the common values of LCOE found for various energy generation techniques which immediately show the commercial advantages of fossil fuel based generation along with wind and solar from the renewable energy sector.

WEC Initial	WEC Commercial	Wind and Solar	Fossil Fuels
0.25-1.75	0.12-0.47	0.03-0.22	0.05-0.28

Table 2.2: LCOE ranges of various energy generation methods listed in units of $/kWh [19]

Traditionally, the ocean energy sector has not been in the eye of commercial interest due to problems related to the availability of the resource, survivability issues when working in the harsh marine environment and reliability problems [22], this is reflected in the high values of LCOE for WEC's. However, with the goals of near future de-carbonization, wave energy has been given a renewed interest, an example of which is its identification in the strategic energy technology plan for the European Union [22].

3

Literature Review

This section aims to introduce the reader to the concept of the oscillating water column (OWC) as a wave energy converter. The operating principles of the device will be described below along with possible configurations that exist, both in terms of structural design and turbine options. Next, various implementations of the device in the world will be discussed with a focus on the incident wave energy in the deployment environment. Locations where the incident wave energy is similar to that of Gwadar will be identified as case studie(s) for which more specific details will be mentioned.

3.1. The Oscillating Water Column

The oscillating water column (OWC) is a type of wave energy converted that was conceived in 1965 by Yoshio Masuda, regarded as the father of wave energy [23]. Being an officer in the Japanese Navy, Masuda developed the worlds first floating OWC in the form of a wave powered navigation buoy which was later commercialized in large numbers [23]. His success led him to develop an OWC on a much larger scale called the Kaimei which was a barge integrated with 13 chambers deployed off Japan's western coast in 1978 [23].The OWC device is typically configured to operate as a point absorber or terminator and since its inception in 1965 [23] it has seen much experimentation and development resulting in the progression of its technology, as reflected by a TRL score of 8 [19]. This type of device also has the advantage of having very few moving parts which make it relatively easy to maintain compared to other wave energy converters [24]. Additionally, this device can be integrated into existing, proposed or floating marine structures that benefit the financial feasibility of the device [24].

An OWC device is depicted in figure 3.1 and this device harnesses the energy of waves based on the phenomenon of incident wave excitation pressure. From the well established linear wave theory, the hydrodynamic pressure alternates beneath the ocean surface due to the passing of crests and troughs and decays with depth as represented by equation 3.1 [25], where k is the wave number, ω the angular frequency, d the depth of the water column, and z the reference location beneath the free surface.

$$p_{wave} = \rho g \frac{cosh[k(d+z)]}{cosh(kd)} sin(\omega t - kx) \tag{3.1}$$

The forcing generated from hydrodynamic wave pressure causes the inner chamber free surface to fluctuate, resulting in the compression and dilation of an air pocket, which invokes an alternating flow across a turbine to generate power [23]. Figure 3.2 below shows the stages of operation that occur in an OWC device. The efficiency of an OWC can be represented by the capture width ratio which can be defined as the power captured by the device over the wave resource available [26]. In an ideal situation, the pneumatic power of the device should be maximized by creating the largest pressure differential between the air chamber and atmosphere, thereby allowing the turbine to extract the greatest amount of energy. This typically occurs when the OWC dynamics are in resonance with the incident waves and are subject to vary depending on geometric properties such as, the device submergence, duct length, chamber width, air chamber height, and damping induced by the turbine [26] power take-off unit.

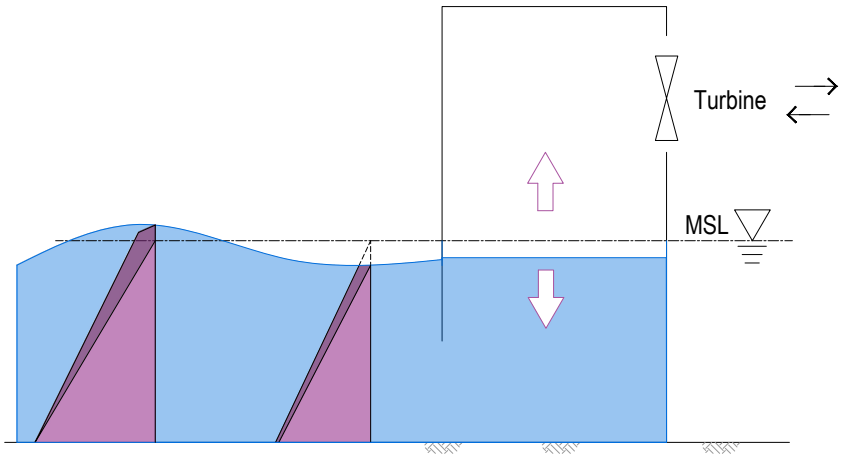

Figure 3.1: Generic oscillating water column

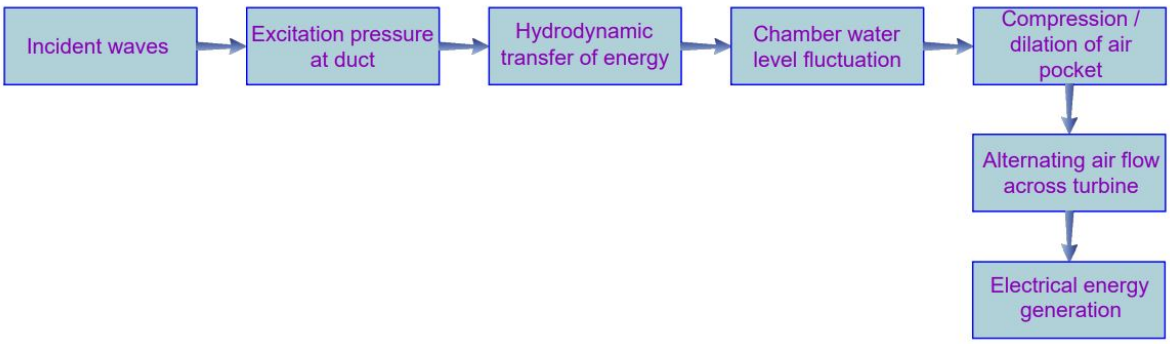

Figure 3.2: Description of oscillating water column energy conversion

3.2. Types of Oscillating Water Columns

Over the course of time OWC's as a type of wave energy converter has evolved into many forms subject to project specific and deployment location requirements. The main categories of OWC's as mentioned in Falcao 2015 are **fixed structures** which can placed on the seabed or embedded in the shoreline, **breakwater integrated structures**, or **floating OWC's** that are typically deployed offshore. Examples of the three main types of OWCs can be see in figures 3.3a, 3.3b and 3.3c below.

Both fixed and floating OWC's cater to the singular purpose of generating energy, with fixed structures limited to deployment in regions at or close to the shoreline and floating structures at locations of sufficient depth [27]. Fixed structures benefit from the advantage of being close to the shore due to cheaper constructions costs, close proximity to the electrical grid and ease of access for maintenance issues [27]. However, the near-shore region has relatively less wave energy compared to deep water due to bottom friction and depth induced wave breaking, for this reason floating OWC's installed offshore offer the best energy harvesting potential [27]. However this comes at the expense of unfavourable economics related to construction and accessibility costs [27].

The next major option of OWC, which is the focus of this report, is the one that is integrated into a breakwater, thereby serving the dual function of energy generation and the sheltering of a harbour or bay from wave action. Deployed in the near-shore region, WEC's integrated into existing or proposed

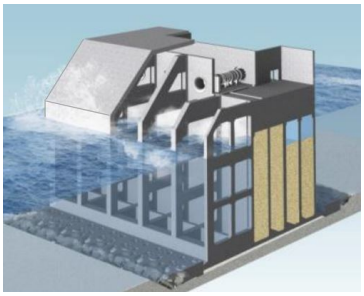

(a) Fixed OWC in Jeju, South Korea [23]



(b) Breakwater integrated OWC in Mutriku, Spain [23]



(c) Floating OWC, the Mighty Whale in Japan [23]

Figure 3.3: Types of OWC's

marine structure can significantly reduce the initial capital expenditure as the costs can be shared thus improving the financial feasibility of the device [27], possibly making it commercially competitive with wind and solar based energy generation. The OWC is the most favoured choice of WEC when it comes to integration with another marine structure with the first example dating back to 1990 in the port of Sakata, Japan [23]. The OWC's ease of integration stems from the fact it has primarily one moving component, the turbine, and a rather simple design with a rigid structure [27]. Based on prior studies it has been found that OWC integration adds an additional 4% of the total project cost for a conventional vertical breakwater [27].

Having established the economic benefits of OWC integration in a breakwater, its integration also results in added hydraulic benefits that improve the performance of vertical breakwaters when compared to traditional ones without WEC integration. Takahashi (1988) investigated the stability of OWC integrated caissons with physical scale models and concluded that this type of device is subject to lower total wave forces due to the phenomenon of wave phase dispersion, thus increasing the structures overall stability [28]. Conventional vertical breakwaters suffer from the problem of high incident wave reflection which can create disturbances in navigation channels, however the implementation of OWC's can reduce the reflection coefficient of the vertical breakwater structure to values of 0.55 [28]. Additionally, based on studies, the presence of OWC's also help to reduce wave transmission and overtopping, resulting in calmer back water conditions favourable for vessel operations [28].

It is important of introduce a sub-category of OWC's that can be integrated into a marine structure or built in a stand alone configuration. This is the U-OWC configuration developed by Boccotti in 2003 as depicted in figure 3.4b where the opening duct is facing vertically upwards with a much lower level of submergence compared to the horizontally facing duct of a conventional OWC, figure 3.4a [29]. The addition of a vertical wall on the wave beaten side of the structure gives the U-OWC much better performance compared to a conventional OWC, as its lower value of submergence expose it to greater amplitudes of wave excitation pressure as defined in equation 3.1 and make it ideal for deployments in environments of low incident wave energy [30]. Additionally, the extra wall elongates the duct length of the device resulting in greater eigen periods that provide a benefit in terms of easier tuning of the device [30]. Boccotti defines the resonance coefficient R a range of values between [-1,1], where negative values imply the device period is less than that of the incident waves, and positive values indicating the device periods larger than those of the waves [30]. An R value of 0 means that perfect resonance conditions between the waves and structure have been achieved leading to the maximization of energy extraction. Based on experiments Boccotti concluded that for significant wave heights of 1m the U-OWC had an absolute R value of 0.38 whereas for the conventional OWC it was 0.75, confirming the superior performance of U-OWC's in low wave energy environments but also extending to more energetic sea states [30]. Hence it can be said that the U-OWC design provides a wider band width of operating conditions over varying sea states due to its better resonance achieving characteristics. Typically, in OWC's the incident waves create a pressure differential that introduces water inside the inner chamber and in doing so, this water imparts a vertically downward force on the caisson, which is approximately 13% larger for U-OWC's compared to conventional OWC's providing greater resistance against sliding of the caisson [30]. The U-OWC design also allows for lower wave heights at the sea beaten wall by about 2.5% in contrast to the traditional OWC, thus enhancing the safety of the structure further [30]. Figure 3.4c below shows the performance curves for a U-OWC and OWC as taken from Boccotti (2007) in terms of converted power for sea states ranging from Hs [1, 6m] and Tp [4, 9.9s], the

advantages of the U-OWC configuration are immediately evident.

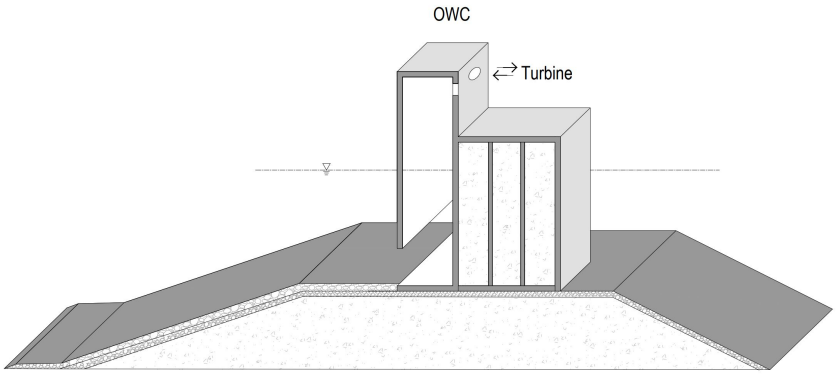

(a) Breakwater integrated OWC

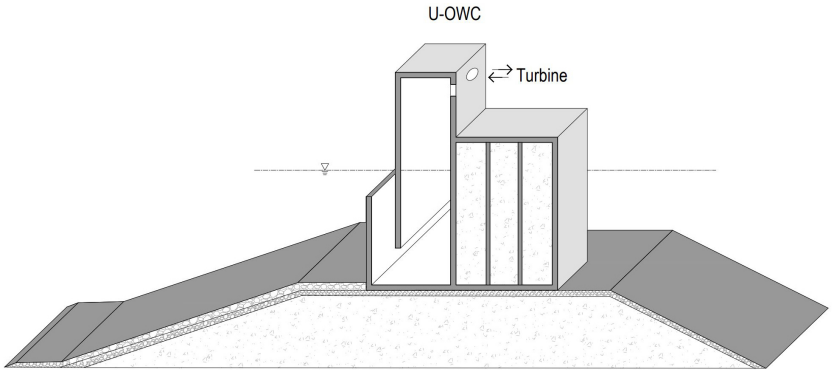

(b) Breakwater integrated U-OWC

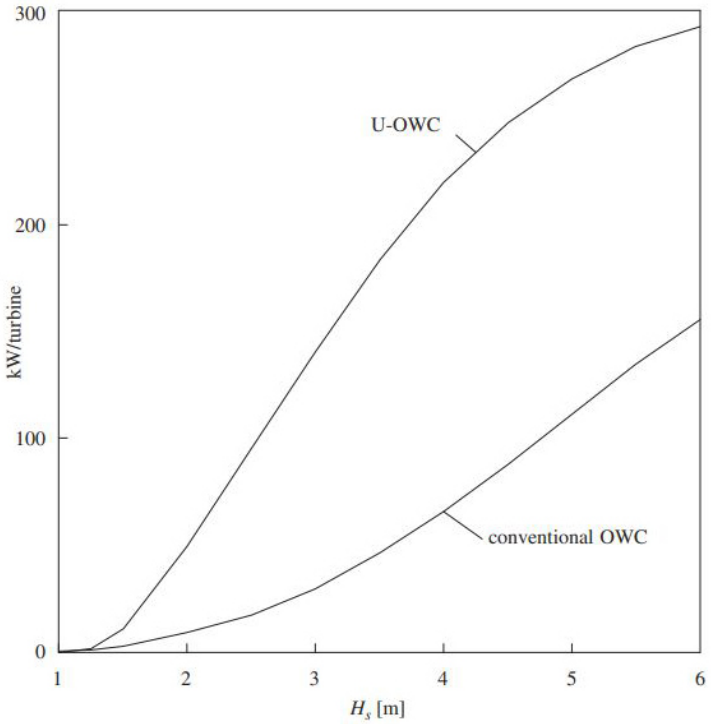

(c) Performance comparison, taken from [30]

Figure 3.4: Comparison of conventional versus U-OWC

3.3. Turbines

The energy extraction process of an OWC (both traditional and U type) can be broken down into two primary stages, namely, the energy absorbed in the inner chamber based on incident waves and resonance characteristics of the device, and the energy successfully converted by the turbine to drive a generator and produce usable electricity. It is the second conversion stage that is the Achilles heel of the OWC, as it is responsible for the bulk of the efficiency loss. The operation of an OWC device induces an axially alternating air flow across the turbine from compression and dilation of the inner chamber air pocket. The design of a turbine to cater to bi-directional flow is not a trivial task, and hence suffers from efficiency loss that effects the final converted power of the device.

In the past attempts have been made to convert the bi-directional air flow to a uni-directional one by means of non-return valves making up a rectifying system but have proven to be unpractical for air flows over 100 m^3/s, as found by the experiments of the Kaimei OWC [23]. Although uni-directional turbines such as a Francis turbine [23] offer greater efficiency compared to bi-directional turbines, the manipulation of the pneumatics to produce uni-directional flow involve the use of valves that impose headlosses and damping that create extra complications in the design [26]. Therefore, bi-directional turbines that are of a self rectifying nature are typically used in OWC's with the most popular options being the wells and impulse turbine [23].

The wells turbine was developed in 1976 by Dr. Alan Arthur Wells and is regarded as a linear turbine in the sense that its flow rate is proportional to the pressure head [31]. It achieves self-rectifying behaviour by having blades with a symmetric aerofoil where the choral plane is perpendicular to the axis of rotation as shown in figure 3.5 below. Therefore this turbine spins in the same rotational direction irrespective of the axial air flow direction. To achieve good efficiency the lift force on the blade, which forces the rotational direction, should be larger than the drag force and based on experiments this turbine has attained a max efficiency of 75% [31]. However, it is important to note that this turbines efficiency is sensitive to changes in the Reynolds number which makes small scale testing difficult [23]. Due to its blade design, the wells turbine exhibits hard stall characteristics for certain flows and only operates at optimal efficiency over a narrow bandwidth and often control systems need to be put in place to ensure the turbine operates within prescribed ranges to maximize power conversion [23].

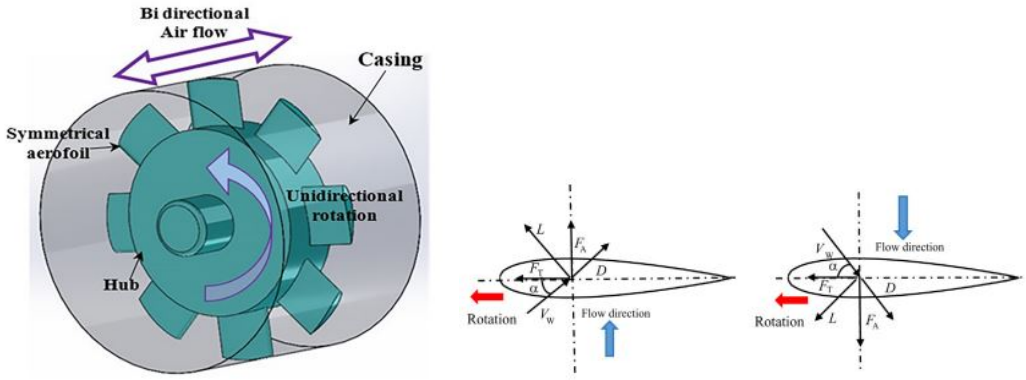

(a) Wells turbine **(b)** Wells turbine blade

Figure 3.5: Wells turbine schematic [32]

The impulse turbine is the next popular option for situation where bi-directional flow is encountered. This turbine was invented in 1975 by Ivan A.Babintsev [31] and achieves self rectifying behaviour by the presence of two rows of symmetrical guide vanes on either side of a hub where the central rotor blade has the same inlet and outlet angle as shown in figure 3.6 [26]. The operating range of the impulse turbine is wider compared to the wells turbine as it does not have a hard stall limit for certain combinations of pressure and flow, however, it has a lower operating efficiency of about 50% which can be increase to 60% by the addition of variable geometry vanes to minimize aerodynamic losses [23].

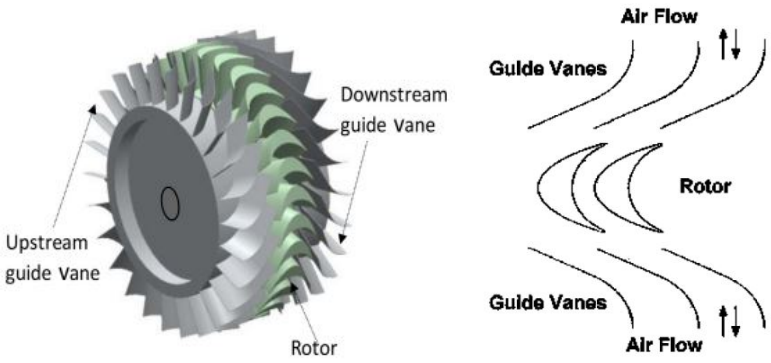

(a) Impulse turbine [26] **(b)** Impulse turbine blade [33]

Figure 3.6: Impulse turbine schematic

The figure 3.7 show the operating ranges for both wells and impulse turbines for the non dimensional flow rate ϕ which is normalized by the flow rate at max efficiency η. Based on this figure the performance difference between the two turbines becomes quite clear. A comparative analysis of both turbines has been done using an identical value of work per unit mass in table 3.1 below. It shows that impulse turbines have much larger kinetic energy swirl losses (V^2) compared to wells turbines, which can be attributed to the presence of guide vanes at the downstream end [23]. Also important to note is that wells turbines require a large diameter (D) to perform work on a unit mass compared to impulse turbines and rotate at higher revolutions (ω) [23]. The higher rotating speed of wells turbines can lead to noise and vibration issues not to mention high centrifugal stresses in energetic sea states [23].

The turbine is coupled with a generator to create a system that is called a power take off unit (PTO) which is responsible for converting the absorbed wave power to electricity. The generator is used to govern the rotational speed of the turbine through torque based on its efficiency curve to maximize power conversion. More information on how to keep the turbine within its optimal rotational speed by means of control and generator induced torque is described in section (9.3) of this report.

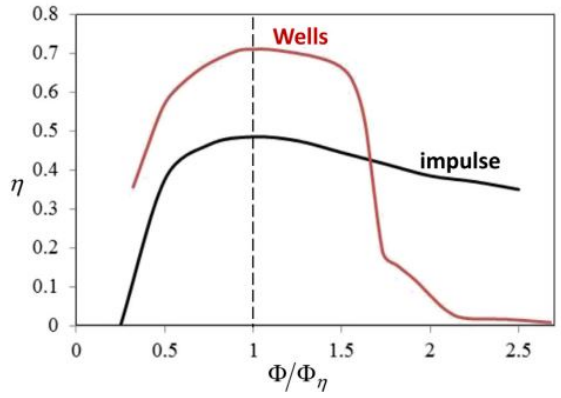

Figure 3.7: Efficiency curve of wells and impulse turbines for normalized non-dimensional flow rate ϕ [23]

$\frac{V_w^2}{V_{imp}^2}$	$\frac{D_w}{D_{imp}}$	$\frac{\omega_w}{\omega_{imp}}$
0.27	1.4	1.7

Table 3.1: Kinetic energy swirl loss, diameter, and rotational speed ratios for well and impulse turbine for identical work per unit mass, taken from [23]

3.4. Case Study

Having presented the reader with an introduction to the various types of OWC's with regard to their configurations and turbine options, table 3.2 [1] has been compiled to highlight noteworthy deployments of OWC's around the world. Based on this table it can be seen that the most dominant categories are fixed stand alone and breakwater integrated OWC's, with the latter being more financially feasible due to cost sharing benefits with the breakwater. The table shows that the wells turbine is the preferred option for most deployments and more importantly highlights that U-OWC's are implemented in regions of low incident wave energy (P_i) which support the literature mentioned in section 3.2 favouring the U-OWC design over traditional OWC's.

Breakwater Integrated							
Location	Type	Commissioned	Turbine	$P_i(KW/m)$	$P_{rated/potential}(KW)$	Chambers	Total Length (m)
Rocella Jonica, Italy [34]	U-OWC	Planned	Wells	3.06	200	8	30
Civitavecchia, Italy [35]	U-OWC	2014	Wells	5.1[36]	25/2500 [37]	124	524
Mutriku, Spain [38]	OWC	2011	Wells	6.67	296	16	70
Sakata, Japan [39]	OWC	1990	Wells	20.3 [28]	60	5 [24]	20 [28]
Fixed Structures							
Pico, Portugal [40]	OWC	1998	Wells	13.4	400	1	12
LIMPET, Scotland [41]	OWC	2000	Wells	17.9	500	3	21
Shanwei, China [42]	OWC	2001 [43]	Impulse [37]	5	100	Unknown	20
Jeju, South Korea [44]	OWC	2012	Impulse [37]	6	500	5	37
Kreavner, Norway [45]	OWC	1985	Wells	27.1	500	1	10
Oceanlinx, Australia [46]	OWC	2014	Wells	46.1 [2]	1000	3	24
Floating Structures							
Mighty Whale, Japan [23]	OWC	1998	Wells	9.1 [3]	110	3	50

Table 3.2: Various oscillating water column deployments in the world

Based on table 3.2, the Rocella Jonica U-OWC is planned for deployment in the current lowest incident wave energy climate of 3.06 KW/m [34]. This helps make a case for the deployment of a U-OWC integrated breakwater in Gwadar, Pakistan, the feasibility of which is investigated in this report. Based on a preliminary estimate using ECMWF data the incident wave energy in Gwadar is 4 KW/m which is subject to change based on results from a SWAN hindcast (see section 6.4). It is predicted that the value will most likely decrease based on the SWAN model results due to bottom friction effects. Hence the Rocella Jonica U-OWC has been selected as a reference model for the U-OWC integrated breakwater design in Gwadar. The key features of the Rocella Jonica U-OWC, asides from the ones mentioned in table 3.2, have been listed below.

- The device is planned to have two connected air chambers feeding to a single wells turbine with an optimal diameter of 0.9 m [34]
- Air relief valve system implemented to prevent turbine to rotate at speeds exceeding the generator limit of 50 KW [34]
- the device will be deployed at a depth of 7.2 m with an outer chamber width of 2m, inner chamber width of 4m, transversal width of 3.2 m, air chamber height of 5.5 m, and a submergence of 2 m due to the low tidal amplitude of 0.3 m [29]

[1] This is not an exhaustive table for all OWC's depolyed in the world. It only mentions the main ones for which information could be found. The information reference has been mentioned in the location column unless explicitly shown otherwise. For Kreavner, Oceanlinx and Mighty Whale, the incident wave energy (P_i) has been approximated using ECMWF data

4

U-OWC Theory

Described in this section are the fundamental equations used for modelling the U-OWC dynamics to the extent that is relevant for this report. Greater details regarding U-OWC modelling techniques can be found in references [47], [48], [49], and [50].

4.1. Fundamentals

The U-OWC concept was developed by Boccotti in 2003 [29] along with the necessary mathematical background to describe its dynamics and those of the interacting wave field [49]. However his approach was augmented by Malara and Arena within the realm of 2D linear wave theory and did not require iterations to be performed, therefore extending its applicability to assess turbine control algorithms. This section will describe the approach used by Malara et al and all equations shown below can be found at reference [50] unless otherwise specified. A generic U-OWC model is shown in figure 4.1 and will be the starting point for the equation derivations. For ease of understanding, various geometric parameters have been listed below.

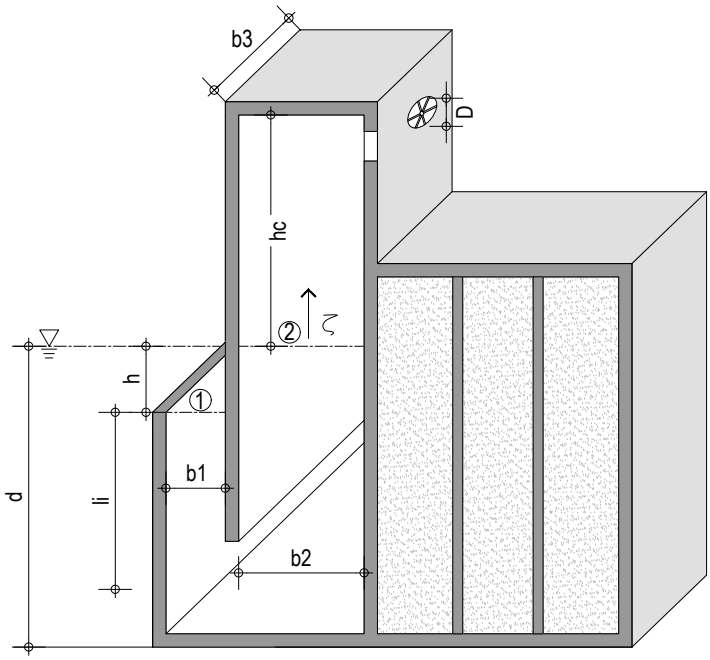

Figure 4.1: Diagram of U-OWC geometric parameters

- $d =$ local water depth
- $h =$ submergence of the U-duct
- $h_c =$ height of the air chamber above mean sea level
- $l_i =$ length of the duct
- $b_1 =$ outer chamber width
- $b_2 =$ inner chamber width
- $b_3 =$ transverse width
- $\zeta =$ inner chamber water level fluctuations
- $D =$ turbine diameter

The fundamental equation on which the dynamics of the model are based is the unsteady Bernoulli equation. This equation is used as a bridge to link the effect of the wave induced excitation pressure at the U-duct opening to the inner chamber water level fluctuations. The equation is applied between points 1 and 2 as shown in figure 4.1 and captures the behaviour of real fluid flow with the assumption that the inner chamber water surface experiences no horizontal variations, only vertical, replicating the motion of a rigid piston. The rigid piston approximation allows only 1 degree of freedom to describe the variation of ζ [49].

The total pressure head at points 1 and 2 is defined by equation 4.1 and 4.2, where Δp is the wave induced pressure, ρ is the density of sea water, g is gravity, $\dot{\zeta}$ is the first time derivative of the water level fluctuations, p_c the inner chamber air pressure, and p_{atm} the ambient atmospheric pressure.

$$H^1 = \frac{\Delta p}{\rho g} \tag{4.1}$$

$$H^2 = \zeta + \frac{1}{2 * g}\dot{\zeta}^2 + \frac{p_c - p_{atm}}{\rho g} \tag{4.2}$$

The net induced wave excitation pressure (Δp) can be defined as the sum of the diffracted pressure (Δp^D) which is described by the pressure spectrum for an irregular sea state, and the radiation pressure (Δp^R) which is a loss of energy transferred to the surrounding fluid due to the vertical movements of the water column in the inner chamber. Equation 4.3 shows this below, where $H(\infty)$ and $\overline{K}$ are hydrodynamic parameters representing the added mass at infinite frequency and the retardation function. Both these parameters play a role in calculating the radiation pressure and their calculation procedure is detailed in reference [49]. As a brief introduction, they are calculated by performing domain decomposition of the problem into regions of fluid such as the far field, at the duct, and the chamber walls. Then velocity potential functions, which are spatial derivatives equal to the velocity of the water particles in respective directions, are defined. The solutions to the velocity potential boundary equations are calculated with the help of eigen function expansions. These are then used to quantify the hydrodynamic parameters.

$$\Delta p = \Delta p^D + \Delta p^R = \Delta p^D + \left[-\rho\frac{b_2}{b_1}H(\infty)\ddot{\zeta} - \rho\frac{b_2}{b_1}\int_0^t \dot{\zeta}(\tau)\overline{K}(t-\tau)d\tau\right] \tag{4.3}$$

The unsteady Bernoulli equation is then written from point 1 to 2 as shown in equation 4.4. Here $\ddot{\zeta}$ is the second time derivative of the inner chamber water level and ΔH_w is the head loss encountered along the vertical duct which is a function of K_w, the U-duct loss coefficient [49].

$$\frac{1}{g}\frac{b_2}{b_1}l_i\ddot{\zeta} + \frac{1}{g}[l_i + h + \zeta]\ddot{\zeta} = H^2 - H^1 - \Delta H_w \tag{4.4}$$

$$\Delta H_w = \frac{1}{2g}\frac{b_2^2}{b_1^2}K_w\dot{\zeta}|\dot{\zeta}| \tag{4.5}$$

Putting everything together, the **equation of motion (EOM) for the oscillations of an independent water column** is given by equation 4.6. The parameters $M(\zeta)$ and $C(\dot{\zeta})$ are defined in equation 4.7 and 4.8.

$$M(\zeta)\ddot{\zeta} + C(\dot{\zeta})\dot{\zeta} + \zeta + \frac{p_c - p_{atm}}{\rho g} + \frac{b_2}{gb_1}\int_0^t \dot{\zeta}(\tau)\overline{K}(t-\tau)d\tau = \frac{\Delta p^D}{\rho g} \tag{4.6}$$

$$M(\zeta) = \frac{1}{g}\left[\frac{b_2}{b_1}l_i + l_i + h + \zeta + \frac{b_2}{b_1}H(\infty)\right] \tag{4.7}$$

$$C(\dot{\zeta}) = \frac{1}{2g}\left[\frac{b_2^2}{b_1^2}K_w|\dot{\zeta}| - \dot{\zeta}\right] \tag{4.8}$$

Now it is important to link the motions of the inner chamber water surface to the compression and dilation of the air pocket which forces air across the turbine for energy extraction. The work of Malara et al mention the equations to do this, however they are written in the form of a singular air chamber and water column. Based on the case study of the Rocella Jonica U-OWC, the possibility of multiple connected air chambers needs to be investigated. This can allow for cost savings as less turbines can be used and connecting multiple air chambers might improve the energy conversion efficiency of the device, both important aspects to consider for a wave energy converter. For this reason the equations have been modified to allow for the connection of N air chambers to the same turbine, while keeping the oscillations of each water column independent. By doing so, the system is characterized by $n+1$ degrees of freedom where n is the number of number of oscillating water columns operating independently and the plus one represents the inter connected air chamber.

Using the basic definition of density and volume, equations 4.9, 4.10, 4.11, and 4.12 can be derived. The quantities $m_{c,n}$, $\rho_{c,n}$, and $V_{c,n}$ denote the mass, density, and volume of air across n connected air chambers. Each of the water columns, from 1 to n, are modelled independent of one another and can take a different value at a particular instance of time denoted by ζ_i

$$m_{c,n} = \rho_{c,n}V_{c,n} \tag{4.9}$$

$$\dot{m}_{c,n} = \dot{\rho_{c,n}}V_{c,n} + \rho_{c,n}\dot{V}_{c,n} \tag{4.10}$$

$$V_{c,n} = b_2 b_3 \sum_{i=1}^{n}(h_c - \zeta_i) \tag{4.11}$$

$$\dot{V}_{c,n} = -b_2 b_3 \sum_{i=1}^{n}\dot{\zeta}_i \tag{4.12}$$

It is assumed that the air in the chamber behaves as an ideal gas during stages of compression and dilation, and that no heat energy is lost or gained by the surrounding environment [49]. Therefore, the process is described as being isentropic with the air density of n connected chambers, $\rho_{c,n}$ given by equation 4.13 where γ is the specific heat ratio [29].

$$\rho_{c,n} = \rho_{atm}\left(\frac{p_{c,n}}{p_{atm}}\right)^{\frac{1}{\gamma}} \tag{4.13}$$

Next it is assumed that the air mass flow rate of the chamber $\dot{m}_{c,n}$ is equal and opposite the turbine air flow rate $\dot{m}_t$. The turbine dynamics in response to the pressure differential (Δp), between chamber and atmosphere, are captured by equation 4.14 where Λ is the turbine specific coefficient, D its diameter and N the rotational speed. The turbine coefficient is defined as a ratio of the dimensionless pressure (Ψ) and flow rate (Φ) where ρ_{in} is the stagnation air density [29]. These terms are defined in equation 4.15, 4.16, and 4.17

$$\dot{m}_t = \frac{\Lambda D}{N}(p_{c,n} - p_{atm}) \tag{4.14}$$

$$\Lambda = \frac{\Psi}{\Phi} \tag{4.15}$$

$$\Psi = \frac{\Delta p}{\rho_{in}N^2D^2} \tag{4.16}$$

$$\Phi = \frac{\dot{m}_t}{\rho_{in}ND^3} \tag{4.17}$$

The equations mentioned above can be put together to derive the relationship necessary for modelling the air chamber dynamics, as presented in equation 4.18.

$$\dot{p}_{c,n} = -\gamma p_{c,n} \left(\frac{\dot{m}_t}{m_{c,n}} + \frac{\dot{V}_{c,n}}{V_{c,n}} \right) \tag{4.18}$$

Now equation 4.6 and 4.18 can be written as a system of 1st order differential equations in matrix notations with the form $\dot{X} = AX + B$ for a system with $n+1$ degrees of freedom, representing the number of connected air chambers and independent water columns. For this case, ζ will be replaced with ζ_i, where i can range from 1 to n, and dummy variable substitution will be used to transform the 2nd order equation to a system of 1st order equations as shown in 4.19 where $i = 1, 2, 3, \ldots n$

An example of two coupled air chambers with independent water columns has been written in matrix notation below. This is the case for $n = 2$, and for more connected air chambers the same procedure would be performed and the dimensions of the matrices would increase according to the number of degrees of freedom of the system.

$$\dot{\zeta}_i = U_i \tag{4.19}$$

$$\dot{X} = \frac{d}{dt} \begin{bmatrix} p_{c,n} \\ \zeta_1 \\ U_1 \\ \zeta_2 \\ U_2 \end{bmatrix}$$

$$A = \begin{bmatrix} -\gamma \left[\frac{\dot{m}_t}{m_{c,n}} + \frac{\dot{V}_{c,n}}{V_{c,n}} \right] & 0 & 0 & 0 & 0 \\ 0 & 0 & 1 & 0 & 0 \\ -\left[\frac{1}{\rho_{c,n} g M(\zeta_1)} \right] & -\left[\frac{1}{M(\zeta_1)} \right] & -\left[\frac{C(\dot{\zeta}_1)}{M(\zeta_1)} \right] & 0 & 0 \\ 0 & 0 & 0 & 0 & 1 \\ -1 \left[\frac{1}{\rho_{c,n} g M(\zeta_2)} \right] & -\left[\frac{1}{M(\zeta_2} \right] & -\left[\frac{C(\dot{\zeta}_2)}{M(\zeta_2)} \right] & 0 & 0 \end{bmatrix}$$

$$X = \begin{bmatrix} p_{c,n} \\ \zeta_1 \\ U_1 \\ \zeta_2 \\ U_2 \end{bmatrix}$$

$$B = \begin{bmatrix} 0 \\ 0 \\ \frac{\Delta p^D}{\rho g M(\zeta_1)} + \frac{p_{atm}}{\rho_{c,n} g M(\zeta_1)} - \frac{b_2}{g b_1 M(\zeta_1)} \int_0^t \dot{\zeta}_1(\tau) \overline{K}(t-\tau) d\tau \\ 0 \\ \frac{\Delta p^D}{\rho g M(\zeta_2)} + \frac{p_{atm}}{\rho_{c,n} g M(\zeta_2)} - \frac{b_2}{g b_1 M(\zeta_2)} \int_0^t \dot{\zeta}_2(\tau) \overline{K}(t-\tau) d\tau \end{bmatrix}$$

It is important to note that the above mentioned equations do not capture array effects that are responsible for interaction amongst the radiated and diffracted wave fields of the U-OWC which impact the energy production of the system. Equations accounting for array effects are mentioned in reference [51] and in the interest of brevity have not been shown here. The fundamental equations remain the same however the hydrodynamic parameters such as the mass at infinite frequency and retardation function are no longer singular but matrices accounting for interaction effects [51]. The impact of array effects on power production is described in section 9.

4.2. Implementation

To model the complete form of the equations [1] mentioned above capturing the interaction effects of an array configuration, the proprietary codes of Malara have been utilized. Malara's codes make use of a semi-analytical approach that is advantageous in terms of computational time and can serve as benchmark solutions preceding expensive CFD models [51]. Using Malara's codes as a tool allows for the relatively quick assessment and optimization of OWC type devices at any location in the world and are a noteworthy step towards creating a sustainable and greener energy future. The codes play a crucial role in this thesis and are used to assess and maximize the energy generating potential of a breakwater embedded U-OWC in Gwadar, Pakistan.

A brief overview of the code algorithm can be seen in figure 4.2. In its as received condition, the codes could only simulate independent water and air chambers, not accounting for the coupling of multiple inter connected air chambers feeding to a single turbine. The aspect of air chamber coupling has advantages in cost reduction as less turbines are required and can sometimes lead to increased power conversion. Therefore, modifications to the codes were made by the author to model multiple inter connected air chambers. This was done assuming the water columns of each chamber fluctuate independently, where each is described by its own degree of freedom, while the coupled air chambers act as one body of uniform pressure and density characterized by a single degree of freedom. To incorporate this change, the size of certain vector and matrix outputs in the code were re-defined, along with changes in formulations for the air chamber volume and mass as shown in equations 4.9 - 4.12 above.

To perform a simulation three key ingredients are required for input which are the geometry of the structure as defined in figure 4.1, power take off information such as the turbine coefficient, operating rpm, inertia, and efficiency curves, this is then followed by incident wave field data. The incident wave field is characterized by the significant wave height and peak time period which is used to create realizations of a power density (wave pressure) spectrum based on the super position of harmonics with random phase angles. After spectrum creation a Fast Fourier Transform (FFT) is used to convert the incident wave pressures to time domain which serves as the driving force for the U-OWC. Next, the equation of motion (EOM) of the U-OWC (shown in simple independent form in equation 4.6) is solved using one of two techniques, namely, Monte Carlo (MC) and statistical linearization (SL). The SL technique draws its roots from the work of Robert et al [52] and yields the quickest results albeit an approximation. It works by replacing the non linear terms in the EOM with optimal linear ones which makes the system significantly easier to solve and minimize computational time. The procedure for calculating the appropriate linear terms is described in reference [51]. On the other hand, the MC technique relies on the numerical integration of the EOM using a Runge Kutta numerical solver where array effects are captured by the hydrodynamic parameter matrices [51]. Afterwards, the flow rate and air density across the turbine are calculated in both techniques for each time step and the solution is marched forward. As an output, the codes provide the incident, absorbed and converter wave power based on the input parameters.

[1] complete form of U-OWC eqautions accounting for array effects can be found at reference [51]

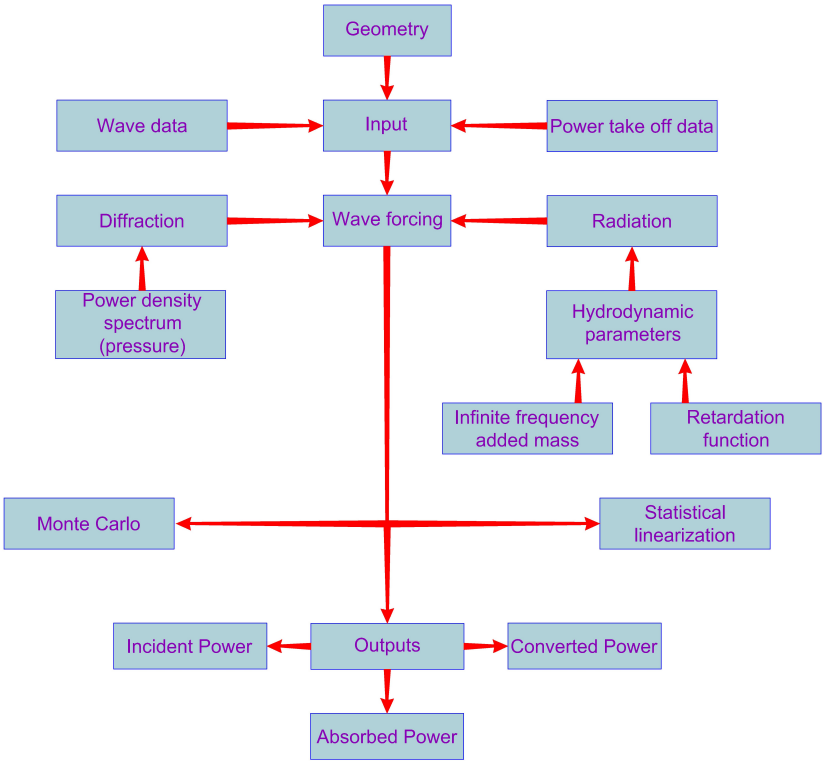

Figure 4.2: Basic flow chart of code algorithm

5

Site Description

The aim of this thesis is to maximize the power conversion by a U-OWC device in the low incident wave energy climate of Gwadar, Pakistan and assess its financial feasibility. At present, under the CPEC agreement a large armour unit breakwater backed by Chinese investment is proposed to facilitate in the creation of an assistance vessel basin. This situation presents the unique opportunity of possibly re-designing the traditional breakwater to comprise of vertical caissons embedded with U-OWC's generating renewable energy. Discussed in this section are the proposed breakwater options presented by the lead consultants and the met-ocean data available for the site which will facilitate in the design of the U-OWC integrated vertical breakwater option.

5.1. Gwadar Breakwater

As mentioned earlier in section 1.1, the Chinese under the one belt one road initiative are investing heavily in the expansion of Gwadar port to revive the maritime silk route and facilitate trade in the region [7]. In this regard, the lead consultants have outlined a master plan for Gwadar port as can be seen in figure 5.1a.

The substantial future expansion plans of the port have resulted in the need of a separate basin for the berthing of assistance and security vessels to cater for the anticipated container vessel traffic. As marked in figure 5.1b, this basin will be located at the southeastern tip of the Gwadar hammerhead and requires a breakwater for protection against waves coming from approximately $170°N$. In this regard the lead consultants have proposed three breakwater alignments termed **option-1**, **option-2**, and **option-3** with approximate lengths of **1.7**, **1.6**, and **2.1** kilometers. The respective options along with relevant bathymetric information for the vessel basin are depicted in figure 5.2 [1] below. As can be seen, the main trunk sections for the three options span across depths ranging from 10-15 m. It is anticipated that option-3 will experience normally incident waves due to refraction from the headland, whereas the other two options will have incidence angles of a slightly oblique nature.

The horizontal alignments of each breakwater option have been determined by the lead consultants and their viability along with further refinement is not within the scope of this report. Each option offers certain benefits and drawbacks in terms of cost and possible shelter area. At present the proposed breakwater(s) have cross sections of the rubble mound type armoured with Chinese pod units. A cross section for the breakwater trunk has been re-created using information taken from local consultants, shown in figure 5.3.

In line with the objectives of this report, breakwater **option-3** has been selected for a potential re-design utilizing vertical caissons embedded with U-OWC chambers extracting wave energy. This option has been chosen due to the following reasons:

- It offers the longest length, hence largest capture width for wave energy extraction. This is an important aspect considering the low incident wave energy native to the site.
- It is expected that the incoming wave ray will be more or less normally incident to this breakwater alignment. This is favoured for U-OWC type WEC's for maximum power conversion.

[1] All information required to create this figure has been provided by the local consultants

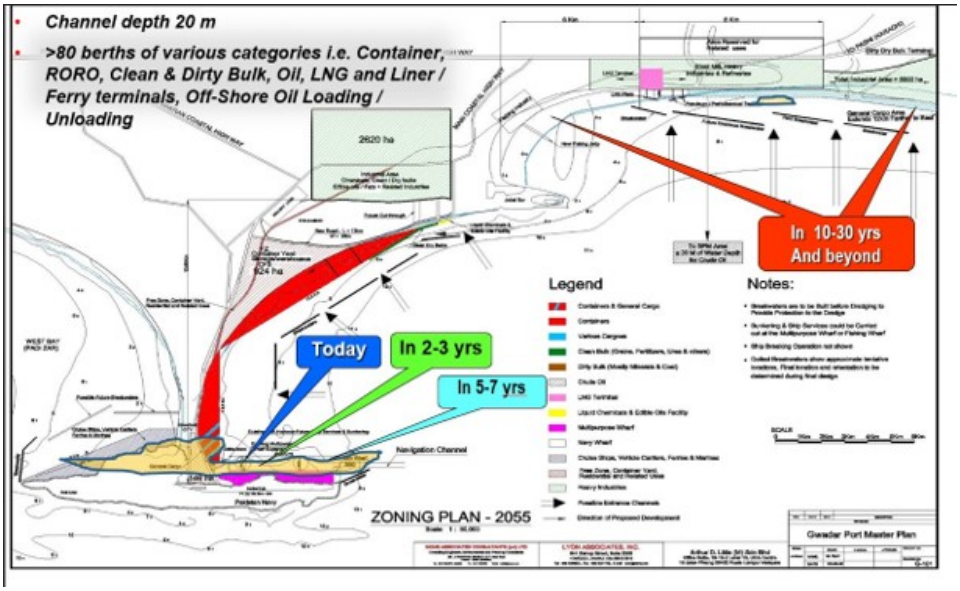

(a) Future master plan of Gwadar port, as taken from [53] (publicly available)

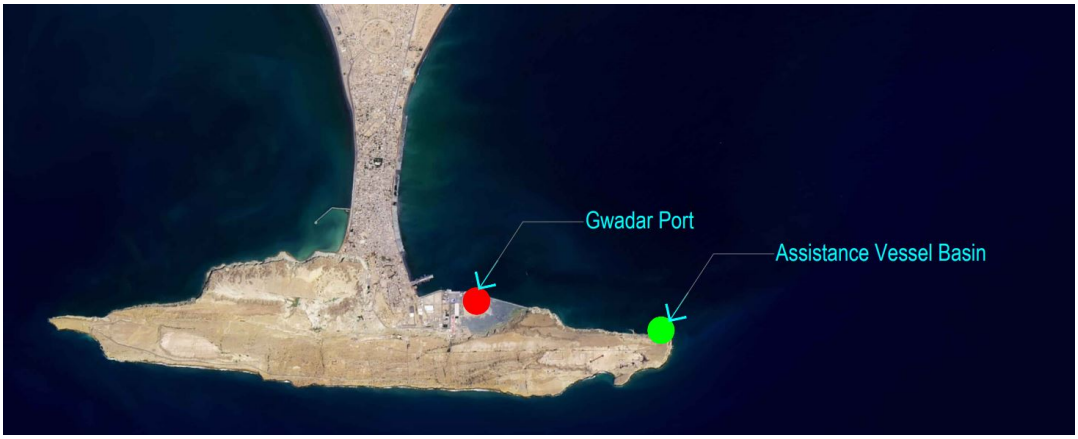

(b) Location of Gwadar Port and assistance vessel basin, image taken from NASA Earth Observatory

Figure 5.1: Gwadar site overview

- Has the greatest potential for relative cost saving as its alignment crosses the deepest regions. Rubble mound breakwaters prove to be expensive when the depth increases due to material requirements and footprint at the seabed (approximately 90 m based on cross section drawing).
- Offers the largest shelter area in its lee for the assistance vessel basin and can easily accommodate future expansion plans

Considering the fact that a substantial investment will be made in the construction of a breakwater, it is worth investigating if re-designing option-3 with vertical caissons integrated with U-OWC chambers generating renewable energy proves to be a superior alternative. Typically, WEC's deployments are not considered appropriate for low wave energy environments because the required capital cost cannot be balanced by the minimal energy generation offered by the device. However, this is not a problem in Gwadar as a breakwater will be built in any case.

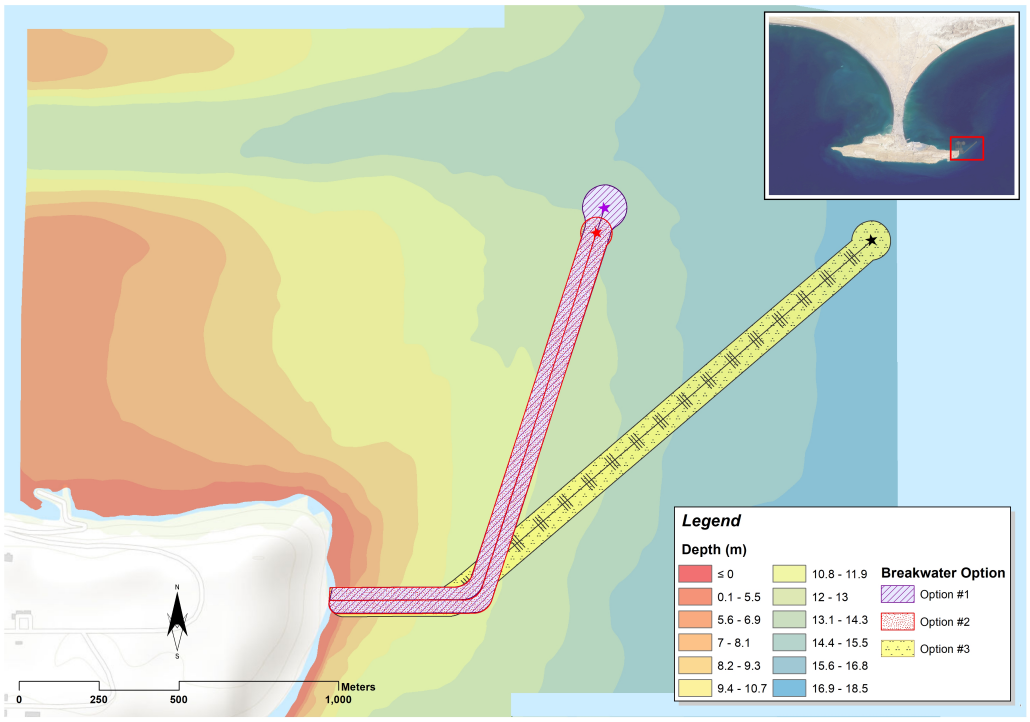

Figure 5.2: Breakwater options and assistance vessel basin layout, depths taken from GEBCO

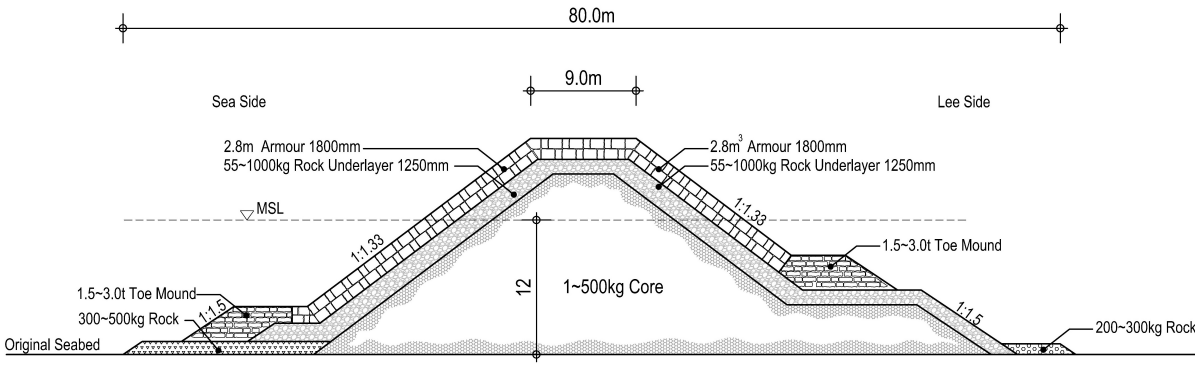

Figure 5.3: Cross section of rubble mound breakwater, re-created based on information provided by local consultants

5.2. Met-Ocean Investigation

In order to maximize the energy generating potential of the U-OWC device, it must be tuned according to the local sea states to encourage the phenomenon of resonance to occur leading to maximum excitation of the inner chamber water surface. To accomplish this task certain critical pieces of information are required that are native to the site of proposed deployment. In this regard, local consultants working under lead consultants are responsible for the met-ocean investigation campaign. They have agreed to provide the following information to further this report in an education capacity.

- Acoustic Doppler Current Profiler (ADCP) data at the 10m and 20m depth contour. Only time-series information provided - not raw data files
- A partly developed but **not calibrated/validated** SWAN wave model. The model included bathymetry data taken from GEBCO along with necessary computational grids.
- Local tidal measurements from the period 07-Aug-2018 to 27-May-2019. Only timeseries information provided - not raw data files

Figure 5.4 below highlights the deployment location of the ADCP's and tide gauge which are underlaid by the local bathymetry. The role of the provided data is as follows, the ADCP data will be used to calibrate the SWAN model (procedure outlined in section 6), which will then be used to perform a long term wave hindcast to determine the classify the sea states incident at the site with a sufficient level of statistical certainty. The tidal data will be used in conjunction with SWAN wave data to optimize the submergence of the 'U-duct' to minimize downtime and determine the design water level under extreme conditions, described in greater detail in section 8 and 9.

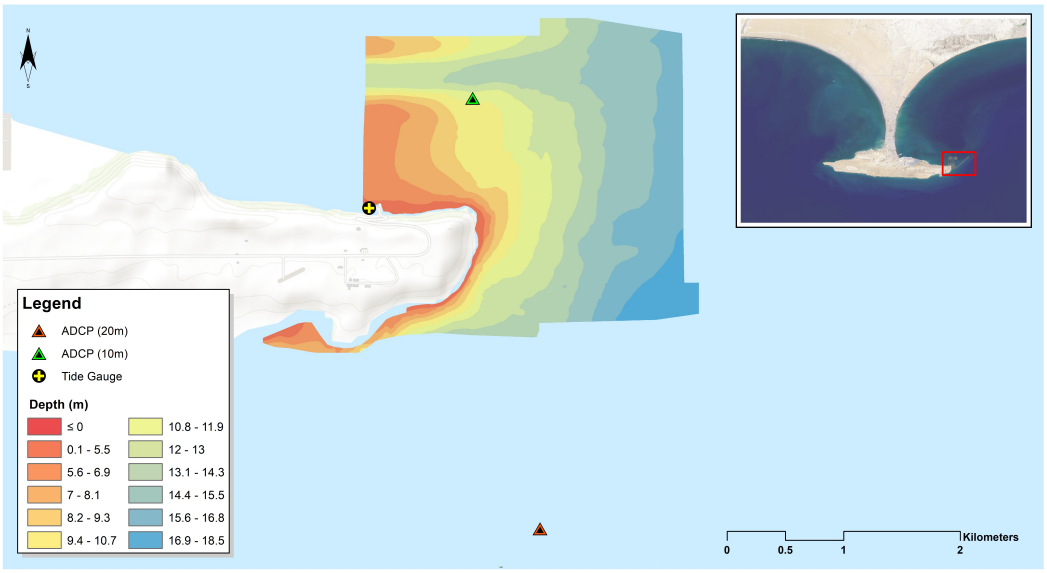

Figure 5.4: Met-ocean investigation campaign, instrument deployment locations

5.3. Data Available

Before using any data for hydraulic design it needs to be pre-processed to check its quality to avoid problems later on. The provided ADCP data (hourly interval) for the two locations in Gwadar have been plotted against corresponding data provided by the European Centre for Medium Range Weather Forecasts (ECMWF-ERA5) for the closest near-shore location. Figure 5.5 and 5.6 show this data, where the top and bottom rows display plots of the significant wave height (Hs) and mean time period (Tm) for the ADCP's at 10m and 20m depth contour. From the plots it can be seen that a significant amount of noise is present in the ADCP data sets, both for Hs and Tm. The source of the noise is uncertain and cannot be investigated further because only an Excel time series of Hs and Tm has been provided, not raw ADCP files. If one would guess, the noise may be attributed to the fact that that wave heights are very low in the October to December period and the instrument might have faced difficulty resolving the sea surface fluctuations based on its deployment settings. The presence of this noise will prove troublesome when trying to use this data for calibrating a SWAN model (section 6), and for any reasonable correlation to be achieved this data has been filtered as shown by the red line. The filtering has been done using a moving average technique based on visual inspection. Due to the doubt in the ADCP data, the SWAN model calibration will also be verified by the ECMWF data. From this point onwards all references made to the ADCP data will refer to the smoothed data time series.

Moving on, the tide gauge data that has been collected over a period of 10 months (293 days) has been plotted in figure 5.7. It can be seen that the deployment location experiences well defined spring and neap cycles and the data exhibits a neutral tidal plane indicating that the instrument did not shift or settle during its deployment. Upon close inspection of the time series data, the region experiences a mixed semi-diurnal tide with two high and low waters every day. This data will be used to perform a 20 year tidal prediction the details of which are outlined in section 8.

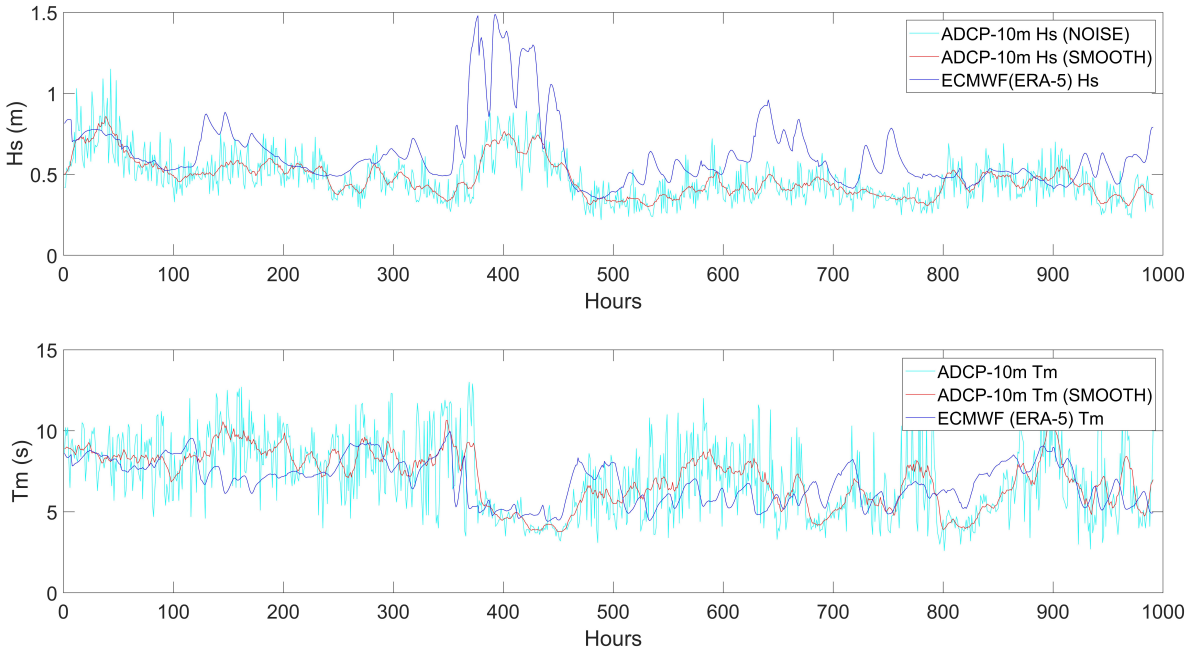

Figure 5.5: ADCP-10m location, plot of Hs and Tm against ECMWF (ERA-5)

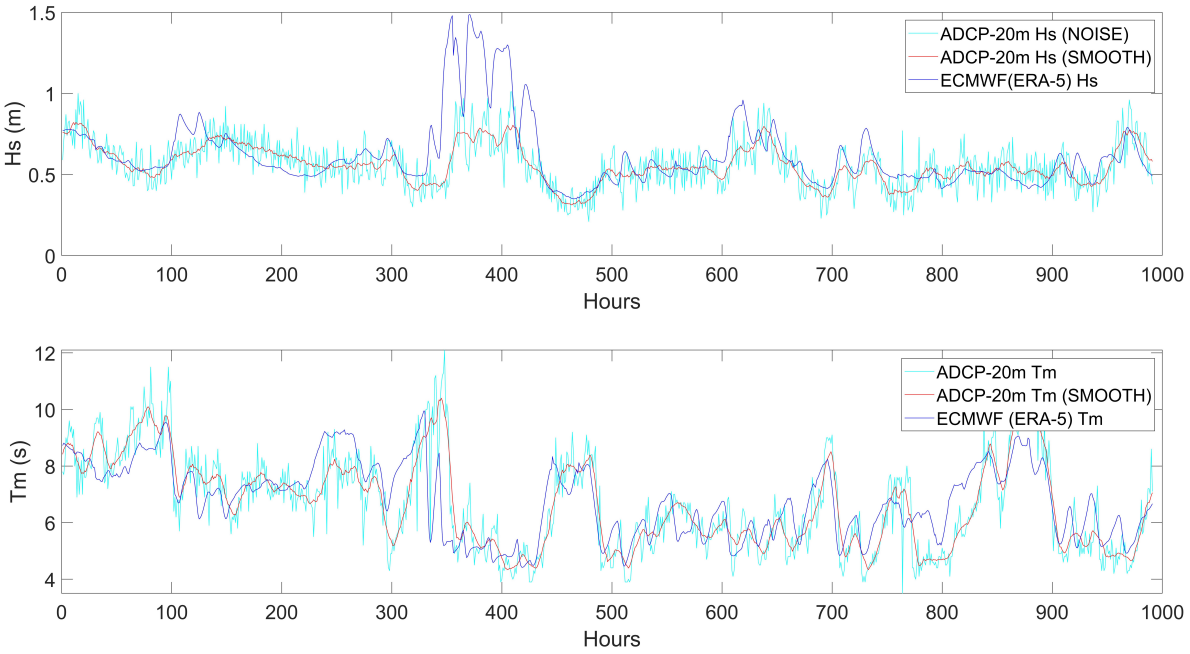

Figure 5.6: ADCP-20m location, plot of Hs and Tm against ECMWF (ERA-5)

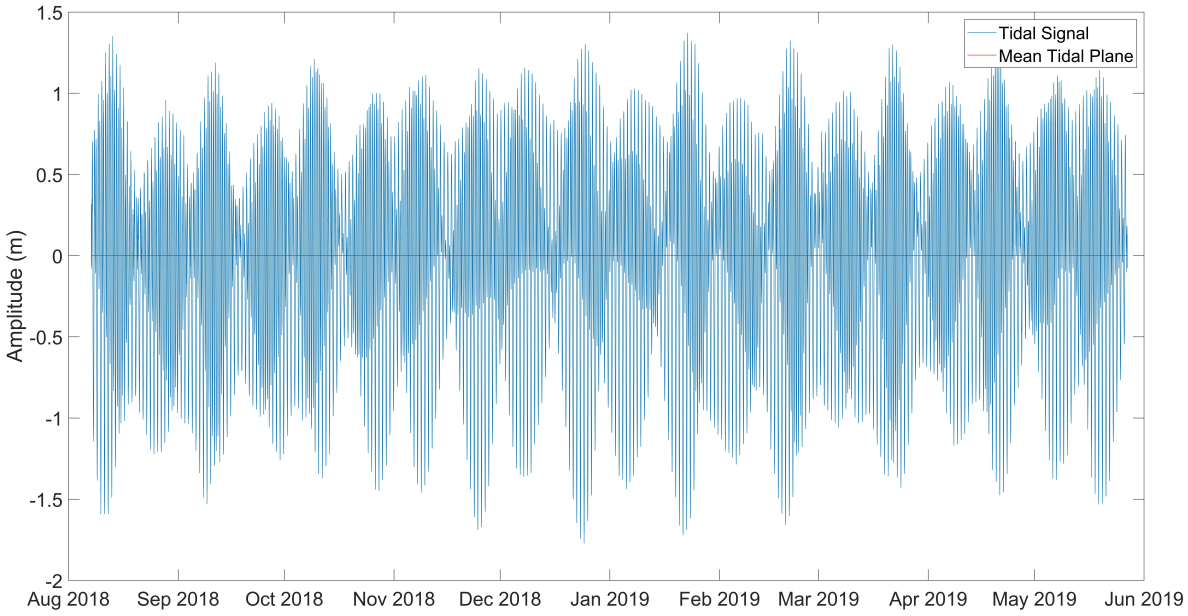

Figure 5.7: Plot of tide gauge data for 1 year

6

SWAN Model

Described in this section is the calibration and validation procedure undertaken for the SWAN wave model, along with the results of a 10 year hindcast for Gwadar. This data set will provide valuable insights, with a certain degree of statistical certainty, about the local wave climate and serve as the foundation for the design of the vertical breakwater integrated U-OWC chambers harnessing wave energy.

6.1. Model Introduction

Based on well established linear wave theory, it is a known fact that the sea surface over a given period of time can be described by its variance density spectrum which when multiplied by ρ and g becomes the energy density. In this regard, numerical wave models attempt to replicate the evolution of the wave spectrum (energy) over time and space subject to certain boundary conditions. In the presence of no currents, SWAN models the energy balance of the spectrum as defined by equation 6.1 where, E is the energy density spectrum, ω the angular frequency, C_g the group celerity, θ the direction, and S represents the source terms [25]. In this equation x and y represent a Cartesian plane, however, the equation can also be used with spherical coordinates (latitude and longitude), as done in this report.

$$\frac{dE(\omega,\theta,x,y,t)}{dt}+\frac{dC_{g,x}E(\omega,\theta,x,y,t)}{dx}+\frac{dC_{g,y}E(\omega,\theta,x,y,t)}{dy}+\frac{dC_{\theta}E(\omega,\theta,x,y,t)}{d\theta}=S(\omega,\theta,x,y,t) \quad (6.1)$$

SWAN falls under the category of phase-averaging models that have the benefit of not being constrained to using small time and space steps with reference to the wave length or period [25]. This allows the model to calculate the statistics of an irregular wave field over a large computational domain in a relatively short amount of time, the same cannot be said for phase resolving models.

6.2. Model Setup

The received model comprised of three computational grids of varying resolutions defined in spherical coordinates along with the necessary bathymetry. Table 6.1 and figure 6.1 below lists the details of the computational grids, where it should be mentioned that the middle and inner grid are of the nested type. The aspect of nesting is done to save on computational time as it allows the area of interest to be modelled with much finer resolution that does not necessarily have to extend to the other regions of the model. The forcing conditions which are used to drive the model are propagated inwards in a stage wise manner on each grid of subsequently higher resolution.

The aim of the report is to produce a comprehensive resource assessment based on SWAN and not only on propagated resources. Therefore, the approach used minimises large over-estimations, and takes full advantage of the shallow water mechanics in SWAN. Furthermore, ERA-5 and satellite data represent far offshore conditions which should always be re-estimated, the nesting adaptation allows a smoother transition to shallower water, and high fidelity spatial domains.

Grid	Area (Km^2)	Resolution
Outer	90250	$0.05° \approx 5Km$
Middle	4678	$0.01° \approx 1Km$
Inner	316	$0.002° \approx 200m$

Table 6.1: Description of SWAN computational grids

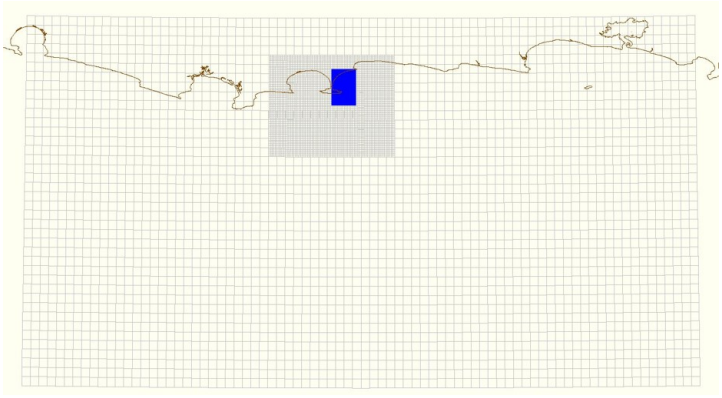

Figure 6.1: Plot of outer, middle, and inner SWAN computational grids

The bathymetry used for each grid of the model can be seen in figures 6.2a, 6.2b, and 6.2c [1] below. The location of the breakwater (option-3) has been marked along with the deployment locations of the ADCP's at the 10 and 20m depth contour. The outer grid bathymetry extends to sufficiently deep depths of approximately 3000m which then reduce towards land, approaching the area of interest. The changes in bathymetry transform the wave field which directly impact the results of the model, especially in the near shore where waves start to feel the bottom. The bathymetry used in this model consists of data taken from GEBCO for the outer regions, and depths provided by local consultants in the vicinity of the breakwater.

It has been decided that SWAN will be used to simulate 10 years of waves in non-stationary mode from 2011 to 2020. This time frame has been selected to strike balance between statistical certainty and computational time. Before the long term hindcast can be conducted, 3 tasks need to be completed which are as follows.

The **first task** involves collecting the forcing data for wind and waves that will drive the model. This will be done using the ERA-5 data-set created by ECMWF available through Climate Copernicus. From here, parameters such as the significant wave height (Hs), peak period (T_p), mean wave direction (D_m), wave spectral width, wind (U10), and wind (V10) along with geographic coordinates and an hourly time stamp will be downloaded for the simulation period. In its native form the data is of the NETCDF file format that will be repackaged to create two ascii files, namely, the .TPAR and .DAT file [2] using scripts written in MATLAB. The .TPAR imposes time varying wave forcing at each of the wet boundaries of the SWAN computational grid, whereas the .DAT file contains gridded time varying wind information used to generate waves within the computational domain. Figure 6.3 shows visually the imposed forcing conditions where the red triangles at the wet boundaries, east, west, and south depict the wave forcing at increments of $0.5°$ and the green dots mark the wind forcing at increments of $0.25°$. The light blue grid represents the SWAN computational grid with resolution $0.05°$ on which the results will be computed along with a NEST file that will translate the boundary conditions to the next subsequent SWAN grid.

The **second task** involves the selection of appropriate empirical relationships for the source terms available in SWAN to accurately capture the evolution of the spectrum from the off-shore to near shore region. These terms are responsible for the increase and decrease of energy in the spectrum along with its transfer to other frequencies. Additionally, the numerical criteria for the model needs to be defined which includes the discretization scheme, and convergence criteria comprising of a tolerance value and iteration limit.

[1] The breakwater position has been marked in this figure. It has not been included as an obstacle in SWAN

[2] Information on how to create these files and their format is available in the SWAN manual/forum

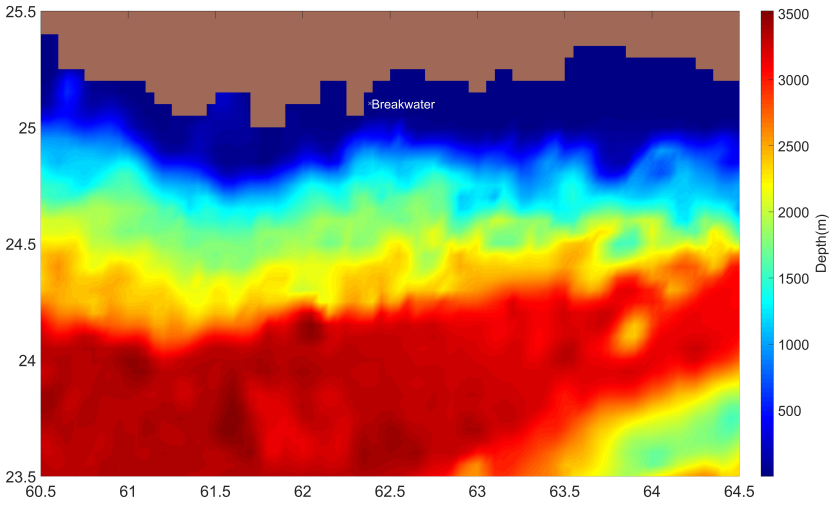

(a) Outer grid bathymetry, latitude on y-axis and longitude on x-axis

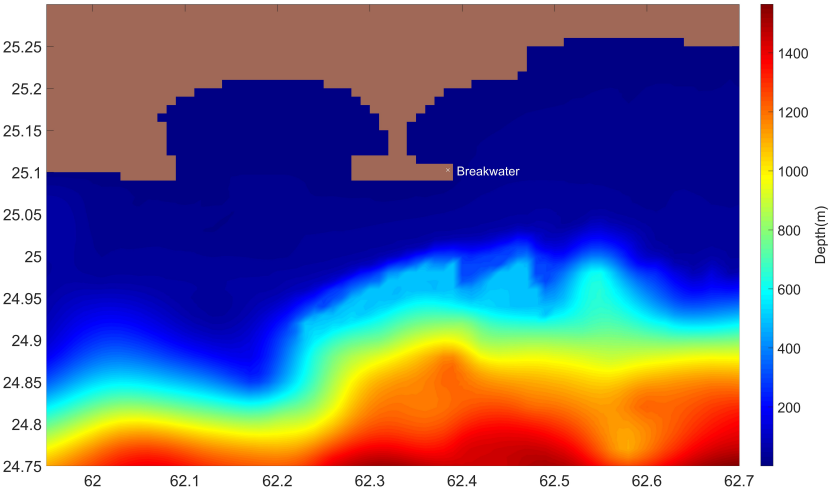

(b) Middle grid bathymetry, latitude on y-axis and longitude on x-axis

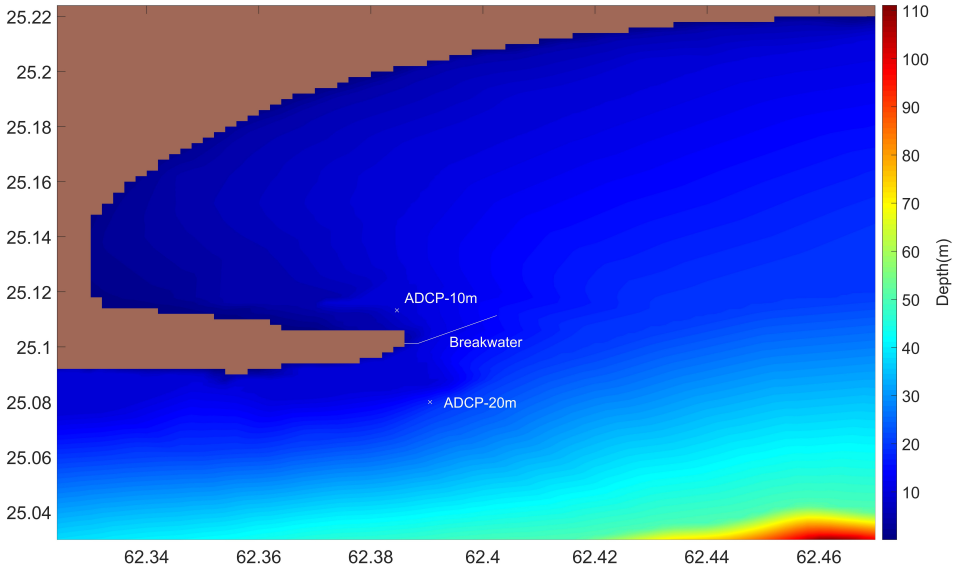

(c) Inner grid bathymetry, latitude on y-axis and longitude on x-axis

Figure 6.2: SWAN model bathymetry

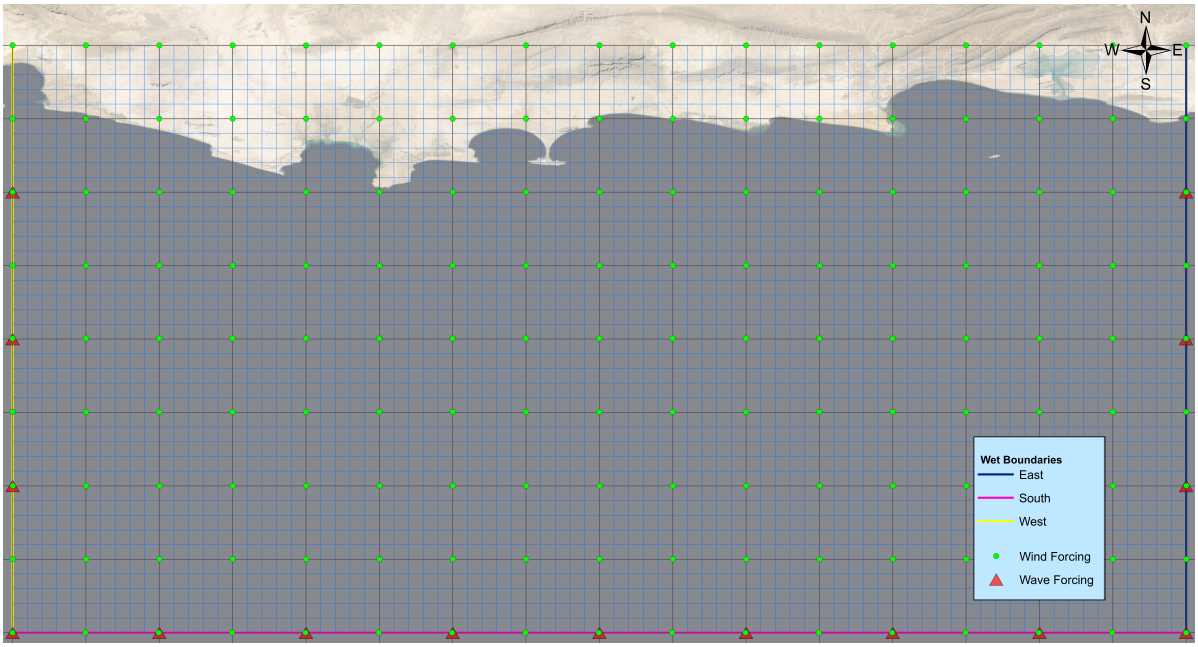

Figure 6.3: SWAN boundary conditions for wave and wind forcing, outer grid

The **third task** involves the validation of the model results against field measurements. In this regard, output points have been defined in SWAN that correspond to the ADCP deployment locations. The model will be run for a window that matches the ADCP measurement time series, accounting for two days of spin up time, after which the results will be compared to assess the model validity. Tasks two and three will be repeated as necessary until an adequate model calibration is achieved, after which the 10 year simulation will be performed.

6.3. Validation

In order to assess the model calibration against the ADCP field measurement and quantify improvement/degeneration, industry standard metrics such as the Pearson regression coefficient (R), model bias (BIAS), and scatter index (SI) will be used. The equations for these parameters can be found at reference [54], and in the interest of brevity have not been mentioned here. The source terms in SWAN that make up the right hand side of equation 6.1 are, S_{in} controlling energy input from the wind, S_{wc} for energy dissipation from whitecapping, S_{nl3} for triad interactions, S_{nl4} for quadruplet interactions, S_b for energy loss from bottom friction, and S_{br} controlling depth induced wave breaking. SWAN incorporates various empirical formulations for each of these source terms along with tunable coefficients, the combinations of which will be used to assess and improve the model.

6.3.1. Base Case Simulation

To ascertain the current state of the SWAN model a **base case simulation** has been performed using largely default parameters making use of a JONSWAP spectrum in GEN3 mode with the KOMEN engine for S_{in} and S_{wc}, whereas MADSEN has been used for S_b. The backward in space backward in time (BSBT) numerical discretization scheme has been used with a accuracy criteria of 0.01 in 98% of the wet grid points with an iteration limit of 80. Based on ADCP and ERA-5 data for the closest nearshore location, the spectral frequency limits for the model have been set from 0.03 - 1.5 Hz. Additionally, the nautical convention is being used with a directional resolution of $10°$. The simulation has been preformed with a timestep of 1 hour for the period 15-Oct-2018 - 18-Dec-2018 to match the ADCP time series. It is important to note that the simulation start time is 2 days prior to the ADCP deployment to account for model spin up time.

Figure 6.4 shows the time series plot of the SWAN results compared to the ADCP measurements and ERA-5. Based on visual inspection, the Hs of SWAN matches relatively well only for the 10m ADCP, whereas ERA-5 tends to over-estimate the values. For the TM01, a clear difference can be

spotted as SWAN is considerably under-estimating the values compared to both ADCP and ERA-5 data. Figure 6.5 highlights that only a reasonable correlation for Hs at the 10m location is present as visible by the number of points on the 1-1 line. The mean Hs calculated from SWAN and measured by the ADCP's is relatively close. However, the same cannot be said for the TM01, where a difference of approximately 50% is present at both locations along with very poor correlations. Table 6.2 and 6.3 list the calibration coefficients for modelled Hs and TM01 against the ADCP's and ERA-5. These tables indicate that SWAN does not compare well with the ADCP's or ERA-5 and significantly under-estimates the TM01 as made evident by the BIAS and RMSE values. On average the SI values are lower for the Hs comparisons versus the TM01 values.

A further investigation was performed by comparing the ADCP measurements with ERA-5, as shown in table 6.4 and 6.5 for the Hs and TM01. The results are surprising because a relatively reasonable correlation of 0.50 or greater is achieved, despite the fact that the ADCP data was very noisy and subjected to a smoothing operation. This indicates that the problem resides in the SWAN model and its calibration must be improved before a long term hindcast can be performed.

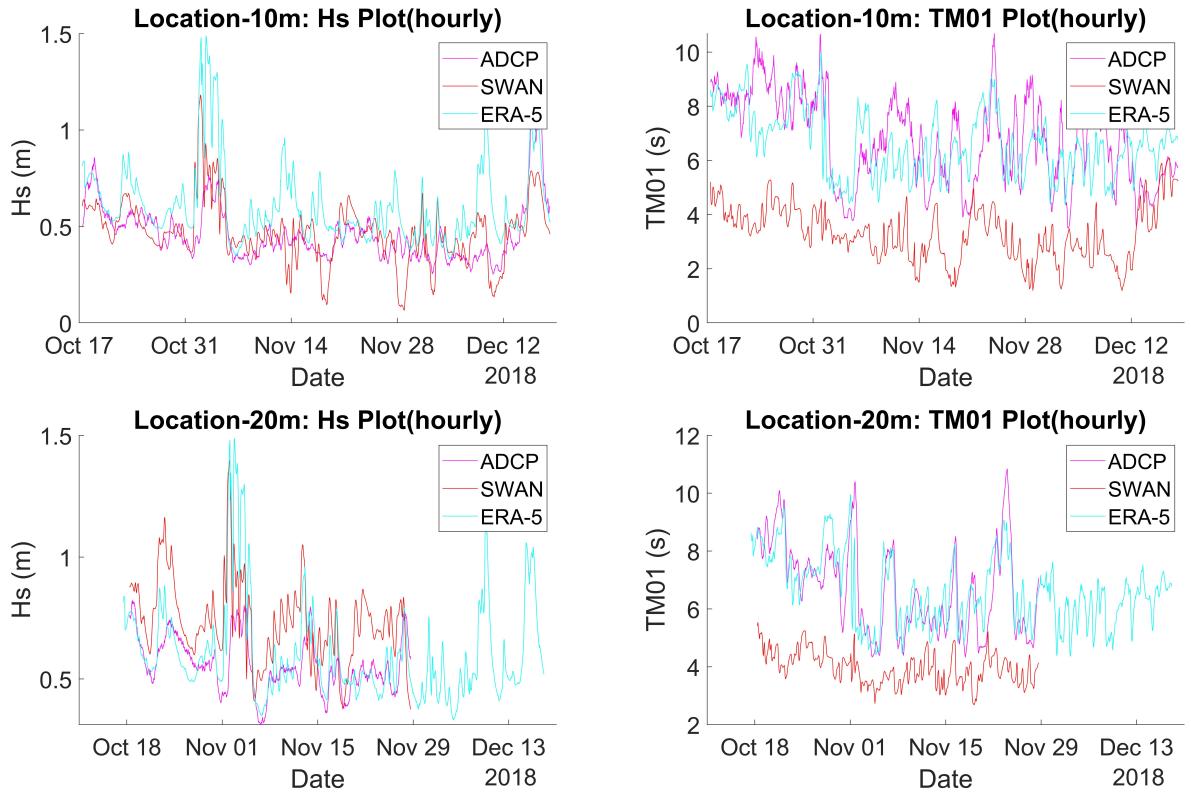

Figure 6.4: Base case simulation result plots of SWAN, ADCP, and ECMWF data

SWAN Hs	ADCP-10m	ADCP-20m	ERA5-10m	ERA5-20m
RMSE(m)	0.14	0.23	0.21	0.22
R	0.6	0.46	0.65	0.18
SI	0.30	0.41	0.34	0.52
BIAS(m)	0.01	0.17	-0.14	0.07

Table 6.2: Base case simulation calibration coefficients for Hs(m)

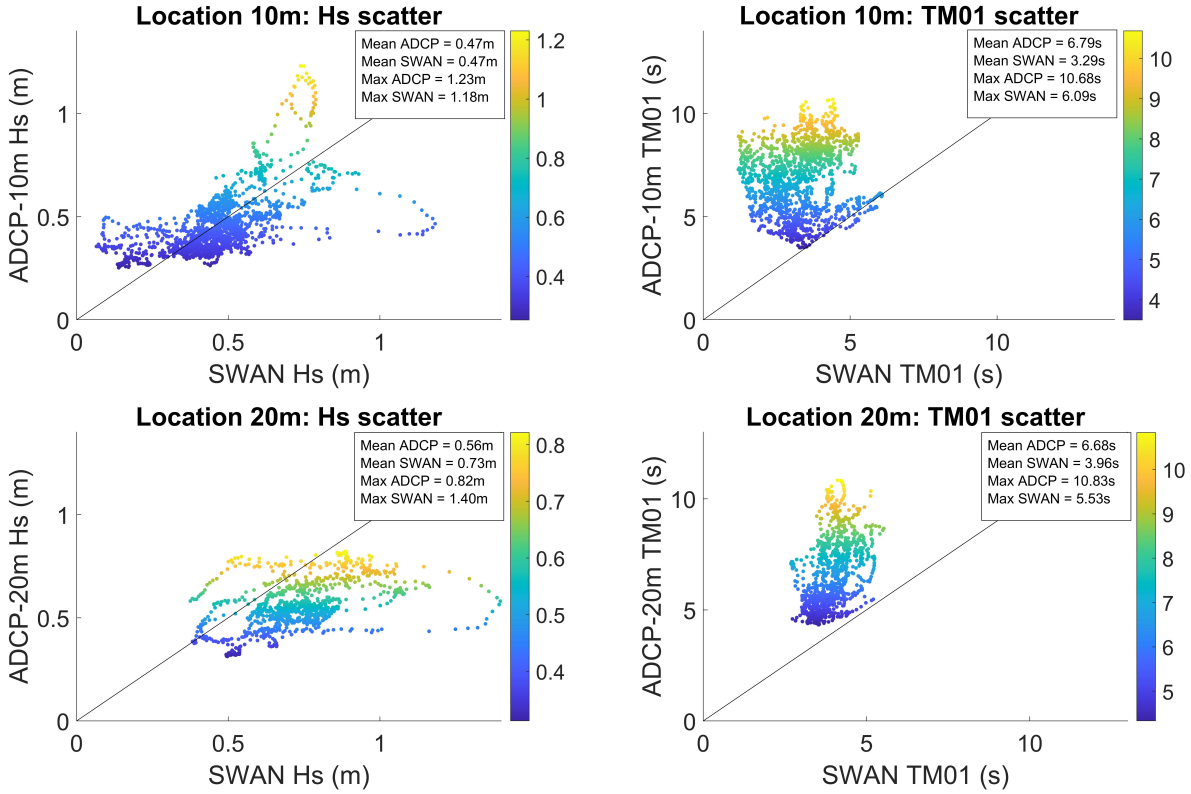

Figure 6.5: Base case simulation scatter plot for 10 and 20m locations, SWAN versus ADCP

SWAN TM01	ADCP-10m	ADCP-20m	ERA5-10m	ERA5-20m
RMSE(s)	3.94	3.06	3.48	2.6
R	0.13	0.47	0.57	0.36
SI	0.58	0.46	0.53	0.56
BIAS(s)	-3.5	-2.73	-3.32	-1.93

Table 6.3: Base case simulation calibration coefficients for TM01(s)

ERA5 Hs	ADCP-10m	ADCP-20m
RMSE(m)	0.22	0.15
R	0.56	0.51
SI	0.48	0.41
BIAS(m)	0.14	0.04

Table 6.4: ERA5 versus ADCP calibration coefficients for Hs(m)

ERA5 TM01	ADCP-10m	ADCP-20m
RMSE(s)	1.47	1.0
R	0.5	0.65
SI	0.22	0.22
BIAS(s)	-0.18	0.1

Table 6.5: ERA5 versus ADCP calibration coefficients for TM01(s)

6.3.2. SWAN Calibration Runs

The calibration of the model is greatly impacted by the formulations used to calculate the various source terms in the energy balance equation along with their tunable coefficients. Ideally, the energy density spectrum for each ADCP measurement ensamble should be compared to that of SWAN to better understand which source terms are responsible for creating differences between modelled and measured

results. However, this data was not available for the ADCP measurements and it was important to determine which source terms to focus on. In this regard, a time series plot (not shown) was made for SWAN and ERA-5 data at a location of reasonable depth, about 600m, where the Hs and TM01 were compared. Based on the plots it was observed that the Hs matched to a reasonable level but the TM01 was being significantly under-estimated by SWAN. Given that this problem was observed in relatively deep water, in addition to the 10 and 20m ADCP deployment locations, it was concluded that the bottom friction (S_b) and wave breaking (S_{br}) source term did not play any significant role, and hence could be eliminated from further investigation. Based on the work of Beyramzade et al [55] the white capping sink term (S_{wc}) in conjunction with a wind source term (S_{in}) impact the model results at deep water, the result of which then propagate to the near-shore region. Hence the focus will be on these terms for model calibration.

SWAN includes a variety of wind packages for (S_{in}) and (S_{wc}) which are functions of the wave steepness, wave number, tunable coefficients and variance density which itself is a function of frequency and direction. Due to the multiple inter-relations between the terms it is not immediately obvious, especially for less experienced modellers (the author), which combination of wind package and white capping term to use to achieve the best calibration and often multiple model runs are required. The findings of Beyramzade et al suggest that the KOMEN and JANSSEN wind packages yield the best results for a SWAN model forced by ERA-5 wind. The results of the base case simulation (section 6.3.1) making use of the KOMEN package for wind and white capping disagree with Beyramzade et al for default settings. The KOMEN wind package is a function of the phase and friction velocity [55], greater details of which can be found in Holthuijsen [25]. In the KOMEN package the c_{ds2} parameter acts as a tunable coefficient[3] that has been incrementally varied as shown in table 6.6 for the 10 and 20m ADCP locations. Based on this table it can be seen that increasing the c_{ds2} parameter mainly reduces the Hs as indicated by the negative tendency of the BIAS values, and less so the TM01. Only a reasonable correlation for Hs at the 10m location has been obtained as seen by R values around the 0.6 range. The remaining correlations are far from adequate and the model continues to under predict the TM01. Looking at the RMSE values, the 20m location shows greater inaccuracies for the Hs whereas the 10m location is more inaccurate for the TM01. The RMSE error for the TM01 is rather large considering that the ADCP measured mean TM01 is around 7 seconds. The runs for the c_{ds2} variations were all carried out with a time step of 1 hour, however, to rule out any numerical problems that might be responsible for the poor performance of the model, a run was performed with a time step of 10 minutes which resulted in negligible differences.

	Hs 10m location				TM01 10m location			
c_{ds2}	R	SI	BIAS(m)	RMSE(m)	R	SI	BIAS(s)	RMSE(s)
0.00001	0.66	0.49	0.19	0.23	0.24	0.64	-4.02	4.32
0.0000236	0.6	0.3	0.01	0.14	0.13	0.58	-3.5	3.94
0.00003	0.64	0.28	-0.01	0.13	0.16	0.57	-3.44	3.87
	Hs 20m location				TM01 20m location			
c_{ds2}	R	SI	BIAS(m)	RMSE(m)	R	SI	BIAS(s)	RMSE(s)
0.00001	0.49	0.8	0.42	0.45	0.62	0.56	-3.49	3.74
0.0000236	0.46	0.41	0.17	0.23	0.47	0.46	-2.73	3.06
0.00003	0.48	0.36	0.14	0.2	0.45	0.46	-2.71	3.04

Table 6.6: SWAN model calibration performance for various KOMEN c_{ds2} values at the 10m and 20m ADCP location. Value of $c_{ds2} = 0.0000236$ is default

Evidence exists that suggests the KOMEN package pumps too much energy into the high frequency part of the wave spectrum [55] that may be responsible for under-estimations in TM01 that the model is generating. The JANSSEN scheme on the other hand has a much stronger dissipation term for the wind input which might rectify the TM01 under-estimation issue and improve the Hs correlations as well [55]. This package incorporates a 2 way interaction between the wind and waves that must be resolved iteratively [55] making it more computationally expensive. As defined in the SWAN manual, the JANSSEN package has two tunable coefficients, δ and c_{cds1}, which based on the work of Beyramzade et al effect the TM01 and Hs respectively. The range of δ varies from 0.5-1 where 1 increases the model

[3] The default value of c_{ds2} has been used for the base case simulation presented in section 6.3.1

TM01, whereas the c_{cds1} typically varies between 1.5-5.5 with higher values lowering the average model Hs. It is important to mention that running SWAN with JANSSEN proved to be very challenging as the model would fail to converge. This issue was resolved by reducing the time step to 10 minutes, relaxing the numerical accuracy criteria and increasing the iteration limit. Due to the difficulties encountered, only a JANSSEN run with $\delta = 1$ was performed as this run was expected to increase the model TM01 by the greatest margin. Table 6.7 shows the results which do not look satisfactory as the correlation coefficient are still low. Using JANSSEN with $\delta = 1$ did improve the TM01 negative BIAS compared to KOMEN, but not by enough to rectify the problem as the RMSE values are still relatively high.

		Hs 10m location				TM01 10m location			
δ	c_{ds1}	R	SI	BIAS(m)	RMSE(m)	R	SI	BIAS(s)	RMSE(s)
1	5	0.6	0.33	-0.02	0.15	0.28	0.48	-2.7	3.26
		Hs 20m location				TM01 20m location			
δ	c_{ds1}	R	SI	BIAS(m)	RMSE(m)	R	SI	BIAS(s)	RMSE(s)
1	5	0.48	0.4	0.15	0.15	0.5	0.42	-2.48	2.82

Table 6.7: SWAN model calibration performance for JANSSEN at the 10m and 20m ADCP location. Values of $\delta = 0.5$ and $c_{ds1} = 4.5$ are default

Due to the lack of success with the KOMEN and JANSSEN packages, the wind formulation of Yan coupled with the Alves and Banner dissipation expression was tested. As mentioned in the SWAN modifications for version 40.51 on source forge, the Alves and Banner white capping formulation depends on quantities local to the frequency spectrum instead of being distributed as in the case for KOMEN. It also mentions that using this package helps rectify the under-estimation of the TM01 in young seas by SWAN. The combination of Yan for wind coupled with Alves and Banner for white capping is achieved by the GEN3 WESTH command in SWAN. The results of the WESTH simulations, where c_{ds2} and br act as tunable coefficients, can be seen in table 6.8 below. As indicated by the table, the use of this package helps lower the TM01 BIAS and increases the correlation significantly compared to previous runs with KOMEN and JANSSEN. The simulation with $c_{ds2} = 0.00005$ and $br = 0.001$ yields the best overall results (made bold in the table) across both locations for the Hs and TM01 and will from this point onwards be refer to as the final calibration run. It is also worth mentioning that in this run the SI values are on average 10% lower compared to previous simulations with the other wind packages and the RMSE values are lower as well.

		Hs 10m location				TM01 10m location			
c_{ds2}	br	R	SI	BIAS(m)	RMSE(m)	R	SI	BIAS(s)	RMSE(s)
0.00005	0.00175	0.73	0.28	-0.07	0.13	0.46	0.41	-2.23	2.82
0.00007	0.00175	0.75	0.28	-0.08	0.13	0.49	0.39	-2.01	2.64
0.00005	0.003	0.66	0.29	-0.03	0.13	0.43	0.5	-3.2	3.41
0.00008	0.003	0.76	0.29	-0.08	0.13	0.49	0.38	-1.94	2.58
0.00005	**0.001**	**0.76**	**0.31**	**-0.1**	**0.14**	**0.52**	**0.33**	**-1.42**	**2.26**
0.00005	0.0005	0.71	0.37	-0.13	0.17	0.56	0.27	-0.62	1.83
0.00008	0.0005	0.67	0.39	-0.14	0.18	0.57	0.25	-0.32	1.72
0.00003	0.0005	0.74	0.34	-0.12	0.16	0.53	0.3	-1.01	2.03
		Hs 20m location				TM01 20m location			
c_{ds2}	br	R	SI	BIAS(m)	RMSE(m)	R	SI	BIAS(s)	RMSE(s)
0.00005	0.00175	0.58	0.23	0.05	0.13	0.72	0.32	-1.86	2.15
0.00007	0.00175	0.57	0.2	0.03	0.11	0.73	0.3	-1.69	2.01
0.00005	0.003	0.53	0.33	0.11	0.19	0.75	0.4	-2.49	2.7
0.00008	0.003	0.57	0.19	0.02	0.11	0.73	0.29	-1.63	1.95
0.00005	**0.001**	**0.54**	**0.19**	**-0.01**	**0.11**	**0.7**	**0.26**	**-1.24**	**1.71**
0.00005	0.0005	0.33	0.24	-0.06	0.14	0.68	0.21	-0.54	1.41
0.00008	0.0005	0.23	0.27	-0.07	0.15	0.67	0.2	-0.28	1.36
0.00003	0.0005	0.45	0.21	-0.04	0.12	0.68	0.23	-0.86	1.54

Table 6.8: SWAN model calibration performance for WESTH (Yan, Alves and Banner) at the 10m and 20m ADCP location. The parameters $c_{ds2} = 0.00005$ and $br = 0.00175$ are default values

Figure 6.6 shows the time series plot of the final calibration run where it can be seen that a much better match is obtained between SWAN and the ADCP's. Additionally, the scatter plots in figure 6.7 highlight that a much greater number of points now lie on the 1-1 line, indicating that a relatively better correlation has been achieved.

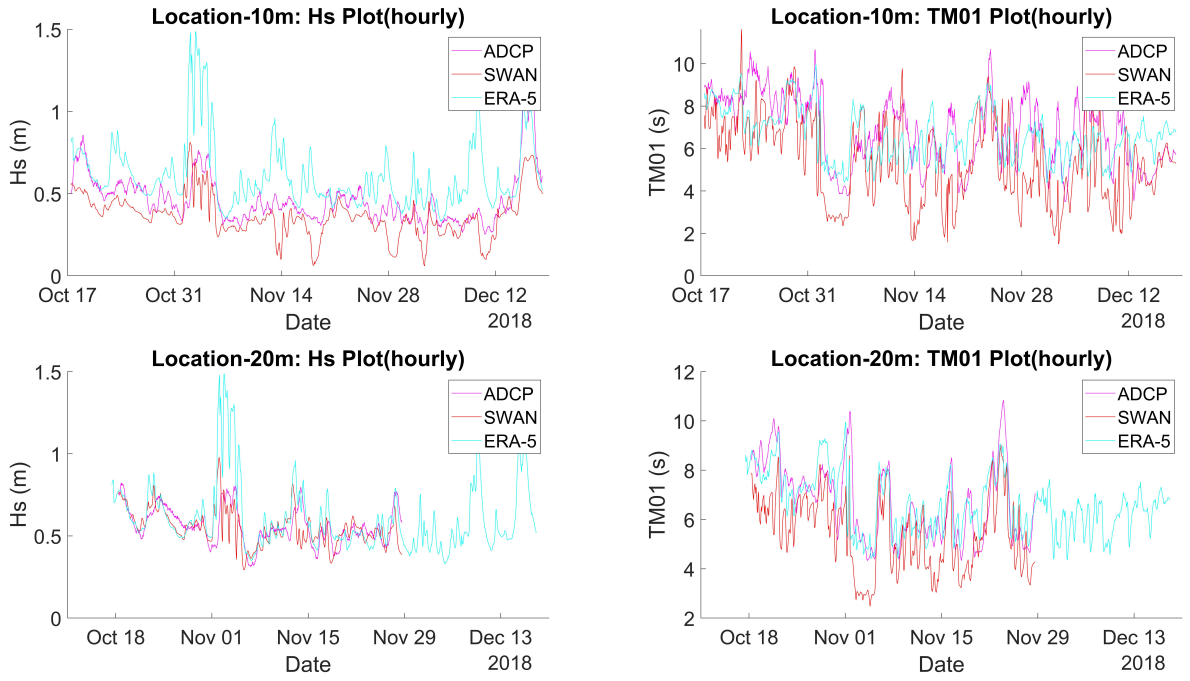

Figure 6.6: Final calibration time series plot for SWAN, ADCP and ERA-5 data

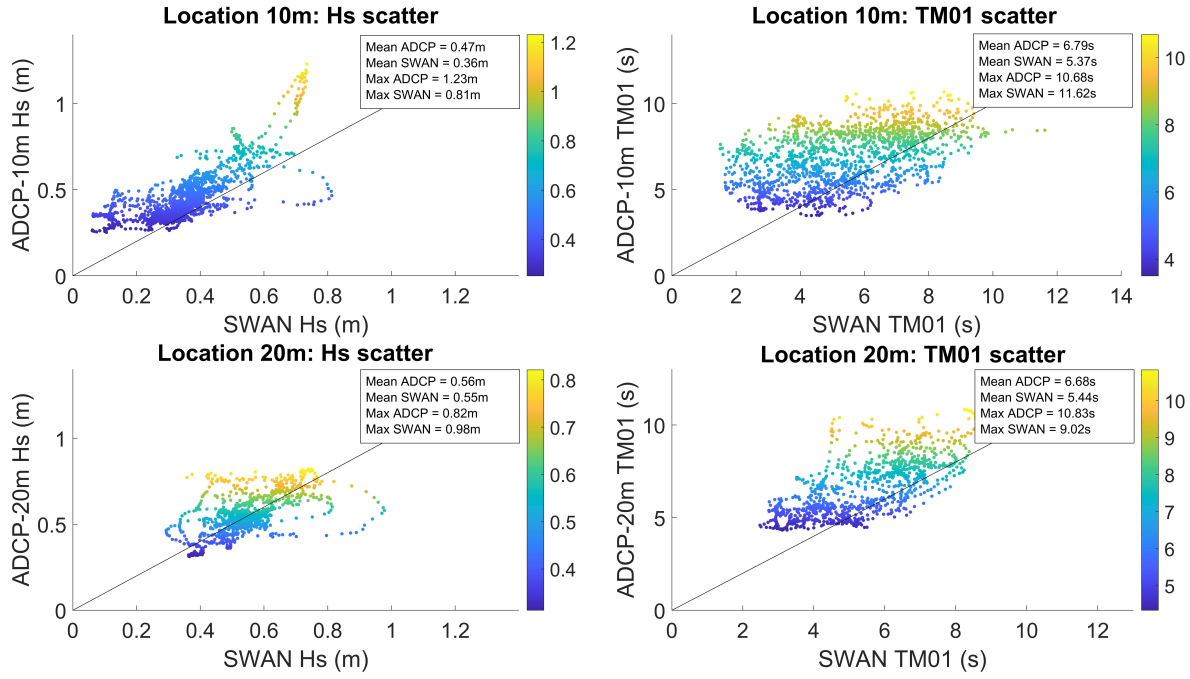

Figure 6.7: Final calibration scatter plot for SWAN and ADCP data

The extent of improvement made in the final run compared to the base case can be seen in tables 6.9 and 6.10. These tables make clear that using WESTH gave an improved calibration compared to KOMEN in terms of the R and RMSE values at both locations. The reason for this is due to the

KOMEN package assigning too much energy at the higher frequencies of the wave spectrum. This fact was confirmed by creating a subtraction surface of the spectral density outputs using both packages where the KOMEN spectrum was subtracted from that of WESTH resulting in a negative variance density peak at high frequency, as can be seen in figure 6.8.

For the purposes of this report, the results of the final simulation have been deemed adequate to proceed with the 10 year hindcast the results of which are presented in the section below.

R improvement 10m location (ADCP vs SWAN)			
Parameter	Base case	Final run	%improvement
Hs	0.6	0.76	**27**
TM01	0.13	0.52	**300**
RMSE improvement 10m location (ADCP vs SWAN)			
Parameter	Base case	Final run	%improvement
Hs(m)	0.14	0.14	**0**
TM01(s)	3.94	2.26	**43**

Table 6.9: Correlation (R) and root mean square error (RMSE) improvement, base case versus final simulation at 10m ADCP location

R improvement 20m location (ADCP vs SWAN)			
Parameter	Base case	Final run	%improvement
Hs	0.46	0.54	**17**
TM01	0.47	0.70	**49**
RMSE improvement 20m location (ADCP vs SWAN)			
Parameter	Base case	Final run	%improvement
Hs(m)	0.23	0.11	**52**
TM01(s)	3.06	1.71	**44**

Table 6.10: Correlation (R) and root mean square error (RMSE) improvement, base case versus final simulation at 20m ADCP location

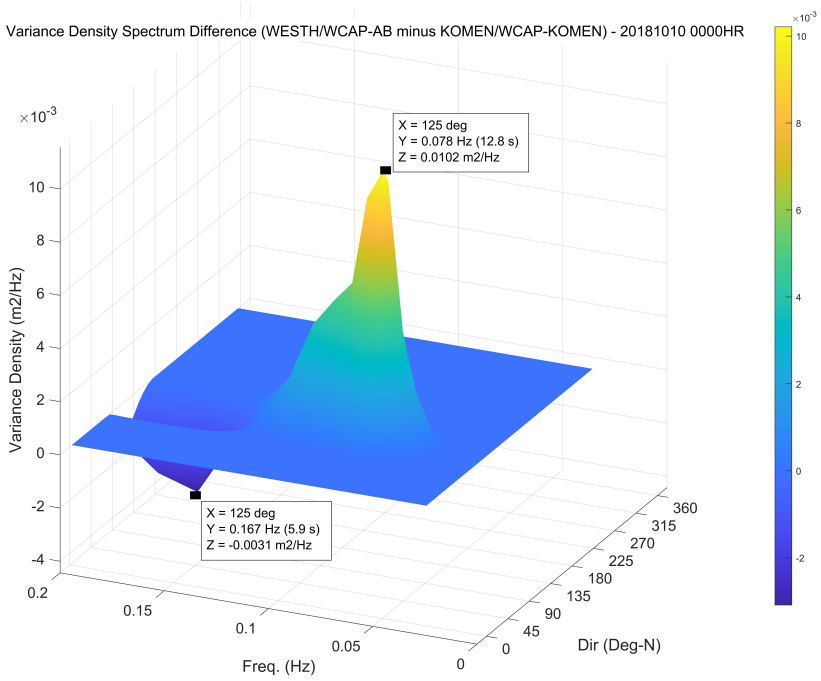

Figure 6.8: Variance density spectrum of WESTH minus KOMEN for timestep 2018-10-10 0000HR

6.4. Results

Based on the calibration procedure outlined in the section above, the SWAN model was used to perform a 10 year hindcast. This was done in a year wise manner, where each year required 3 runs to be performed for the computational grids (outer, middle and inner), thus the total number of simulations for 10 years came out to be 30. These runs were divided amongst 5 residential desktop computers, which after completion were aggregated and post-processed using MATLAB. This data will serve as the foundation for the design of the breakwater integrated U-OWC, additionally it will also provide much needed detail on the wave climate native to Gwadar. A 10 year hindcast is considered sufficient in terms of statistical certainty and will be used to derive 'n' number of design sea states for which the U-OWC device geometry will be tuned to maximize power conversion.

Keeping in line with the motives of this report, the SWAN model results are presented in this section. Figure 6.9 shows that 7 output points have been defined along the breakwater alignment with an additional point offshore at approximately 1000m depth.

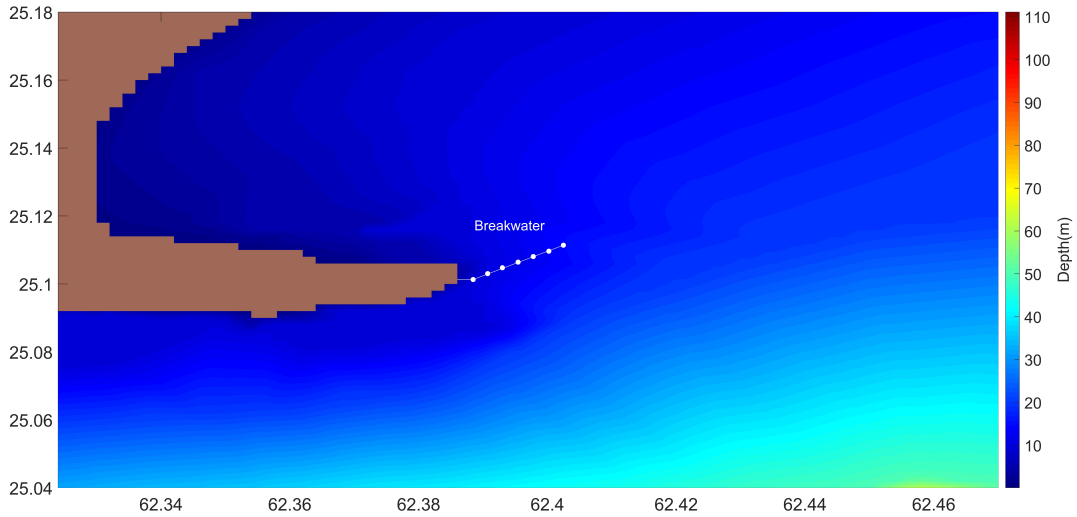

(a) SWAN output points for breakwater option-3, depicted as white dots. Latitude on y-axis and longitude on x-axis

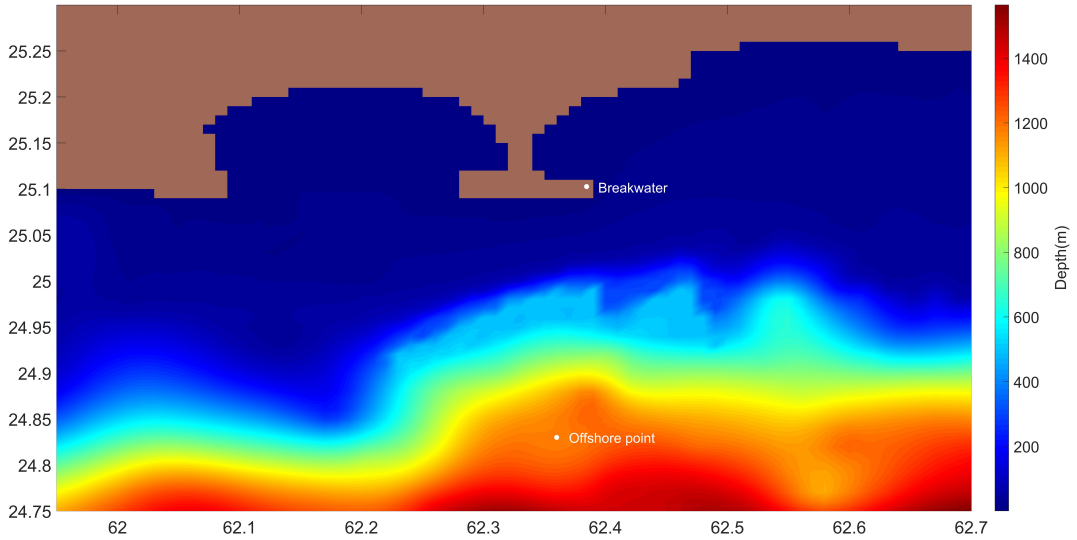

(b) SWAN offshore output point, depicted as white dot. Latitude on y-axis and longitude on x-axis

Figure 6.9: SWAN output point(s) location displayed on model bathymetry

For the output points at the offshore location and tip of the breakwater, figures 6.10a and 6.10b show the wave roses created using 10 years of hindcast data. Looking at the offshore wave rose it can be seen that Hs ranging between 1-2.5 m make up the largest share of conditions and that the dominant direction is from the south with a very minor westward tendency giving a bearing of approximately 182° from north. The Hs in the 0.5-1m band shows a much greater directional variability and ranges from the south-south-east to the south-south-west. This wave rose is made for a location where the depth is around 1000m and the waves do not feel the bottom. For the wave rose created at the breakwater tip (nearshore) it can be seen that the wave ray has an eastward bias due to refraction from the Gwadar headland which causes it to turn. The phenomenon of refraction causes a focusing of the wave directions resulting in less directional variability which serves as an advantage for a wave energy converter. The nearshore rose highlights that the most frequently occurring condition is for Hs values ranging between 0.5-1.5m, whereas relatively large waves range between an Hs of 2-2.5m but occur for a negligible percentage of time. The mean direction of the wave ray based on the nearshore rose is approximately 160° from north.

To gain a visual insight of the refraction taking place at the Gwadar headland, figure 6.11 has been made where the wave ray directions have been plotted as black arrows along with color coded pixels representing Hs values. This figure has been made using data from the timestep: 2018-07-16 2200

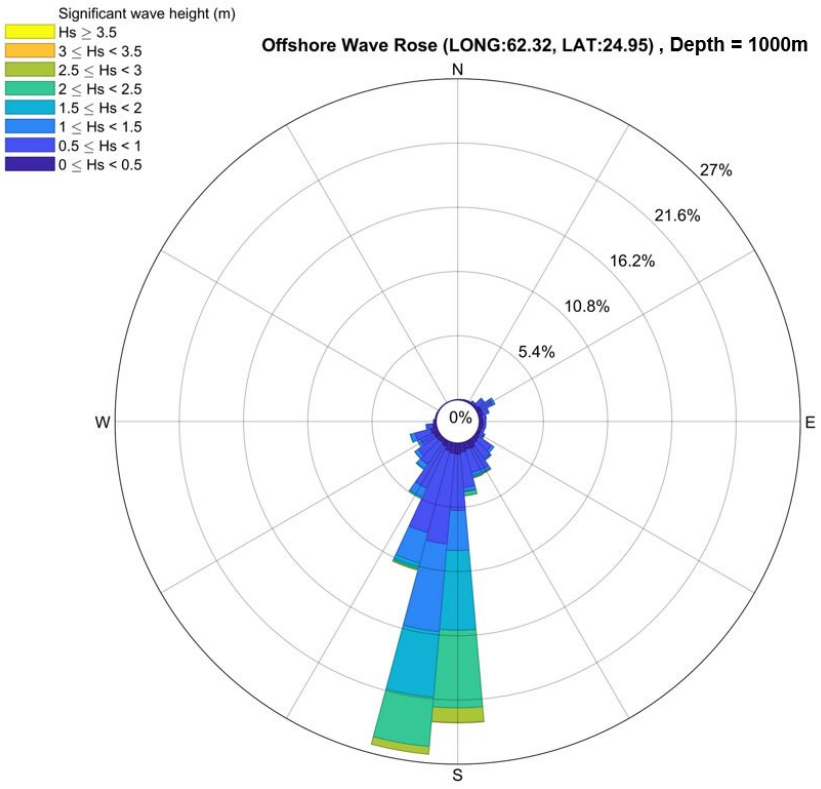

(a) Wave rose for offshore output point.

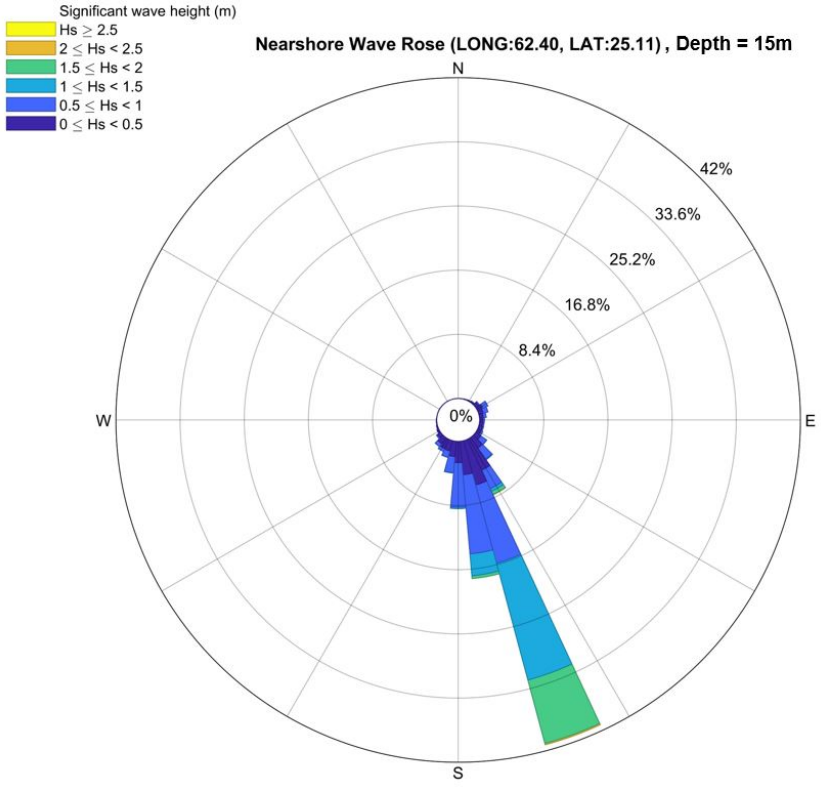

(b) Wave rose for nearshore point, tip of the breakwater.

Figure 6.10: Wave roses for offshore and nearshore locations, direction coming from.

hours and the breakwater alignment[4] is marked using a white line. It can be seen that the impact of refraction extends along the entire breakwater length and aids in minimizing the obliquity of the wave ray incident on the breakwater.

For the 7 output points along the breakwater alignment, spaced at approximately 300m, the 10 year average values at each position have been computed for Hs, Tp, Dm, and P. The values of these parameters along with the depth variation can be seen in figure 6.12. Based on the results, the values do not vary to a large extent so as to prompt the design of U-OWC chambers of varying geometry along the breakwater. It is worth mentioning that only the long straight section of the breakwater oriented in a north-eastern direction is being investigated as a design with integrated U-OWC's, and not the root section of the breakwater due to shallow depth and unfavourable orientation with respect to the wave ray. Given this fact, it can be seen that the depth ranges between 10-15m along the long straight section of the breakwater. The Hs values only differ by approximately 0.1m between nearshore to offshore with negligible changes in Tp. The Dm varies within approximately 8° with a greater eastward tendency at the nearshore. The incident wave power which is a function of Hs and Tp experiences minor variation along the breakwater and is on average approximately 3 KW/m. In figure 6.12 the power values have been approximated using equation 2.2 and show a slight increase at the 10m depth due to the greater Hs value found by the model. At depths lower than 10m the wave power decreases due to bottom friction effects and wave breaking - not shown here.

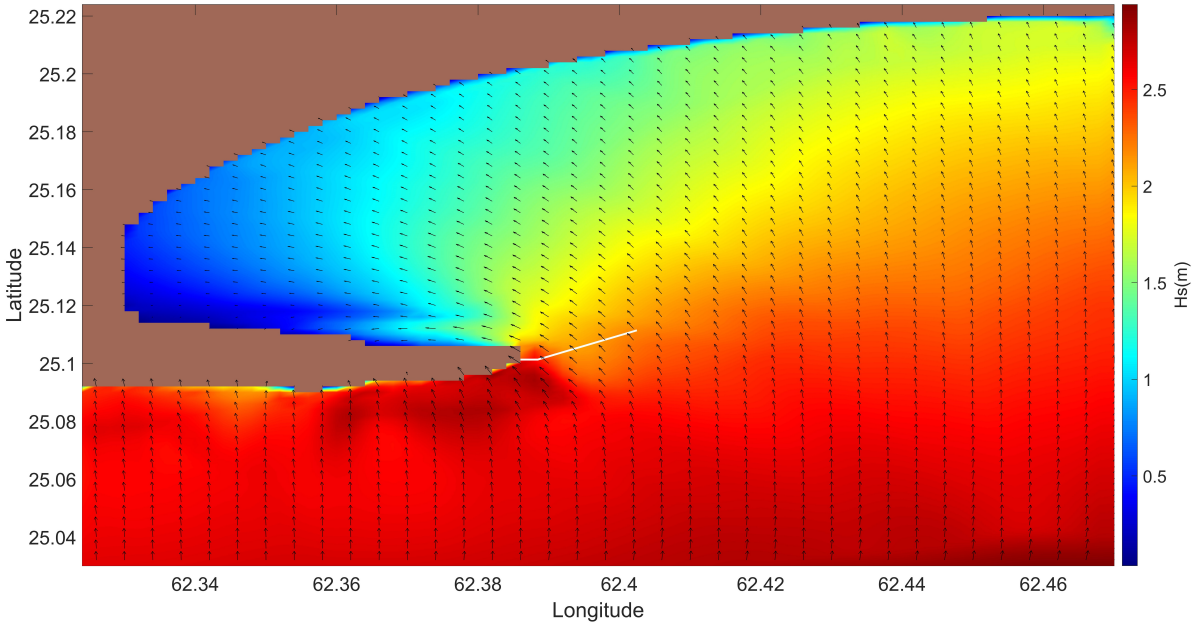

Figure 6.11: Hs plot with direction for time step 2018-07-16 2200 hours

Given the findings mentioned above, the middle output point along the breakwater alignment has been selected for further analysis. The 10 year time series has been parsed month wise to identify the dominant season(s) in Gwadar based on wave parameters such as the Hs, TM01, and Dm. The results of this can be seen in figures 6.13, 6.14, and 6.15 where the value of each bar represents the 10 year average for that month, additionally year wise average values are also depicted by color coded circles, each corresponding to a particular year. Immediately the summer monsoon season can be identified from June-August where the relative Hs values are the highest compared to other months. The wave heights are largest in July with an average value of 1.6m for Hs, and over the last decade the highest average Hs value was experienced in the July of 2018 of 1.8m. From August onwards, the Hs values taper down to about 0.4m and remain this way from March through February, after which they rise towards the summer months. Looking at the TM01, the values are on the order of 8s during the summer monsoon after which they mostly range between 5-6s. In terms of direction, the summer monsoon shows a slight eastward tendency from the months June to August, whereas the winter months display a greater southward bias.

[4]Breakwater alignment only drawn for a visual purpose, it has not been included as an obstacle in SWAN

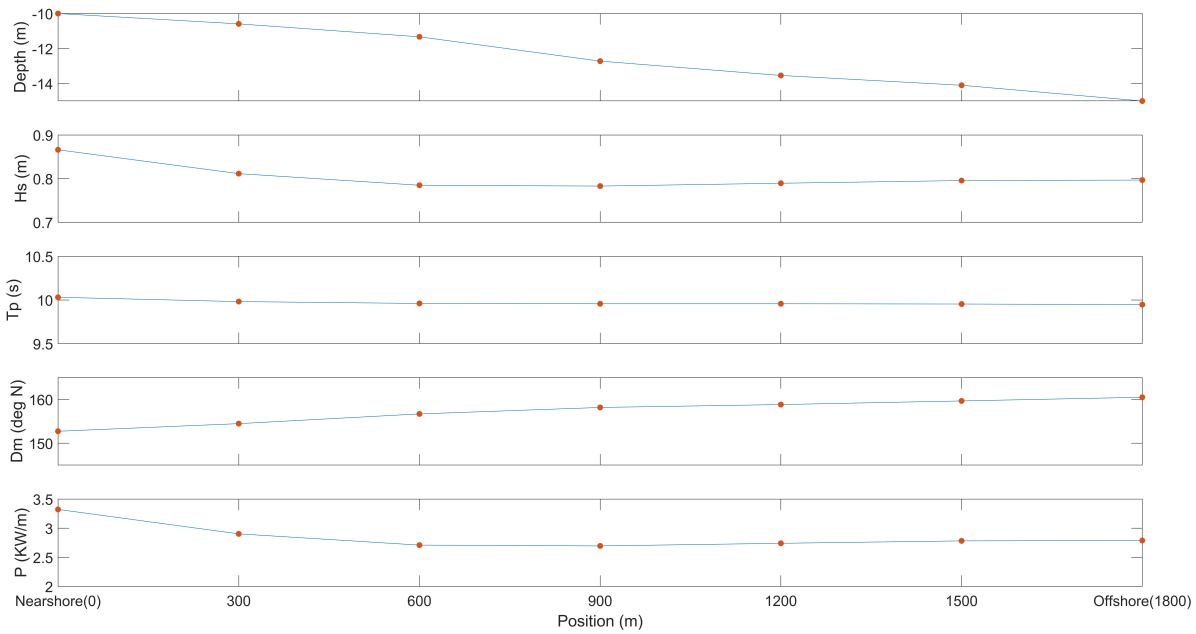

Figure 6.12: Variation of wave parameters along breakwater alignment

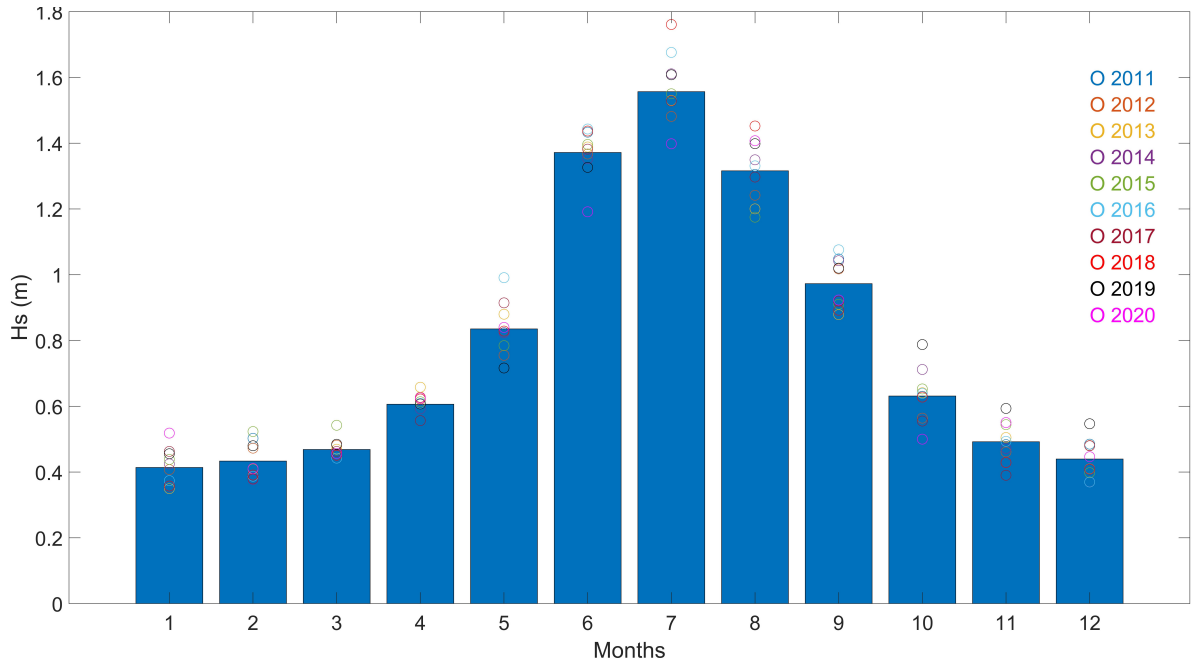

Figure 6.13: Monthly average distribution of Hs over 10 years (2011-2020) at mid-breakwater location

Apart from a monthly analysis it is also important to determine the annual incident wave energy at the location of interest. By doing so a rough estimate can be obtained about the power conversion potential of a WEC, in this case a U-OWC integrated breakwater, based on the local wave climate. Figure 6.16 shows the total annual incident wave power available for each year from 2011 through 2020. The average power across the decade is approximately 3.9KW/m with a standard deviation of 0.4KW/m, and the highest calculated total power is 4.5Kw/m in the year 2018. Based on these statistics it can be said that Gwadar is subjected to a relatively low wave energy climate.

In order for the 10 years of hindcast data generated by SWAN to be utilized in the design and optimization of the U-OWC chambers, it needs to be synthesized into a more usable form. To assist with this objective, the wave climate is broken down into a number of bins, which from this point onwards

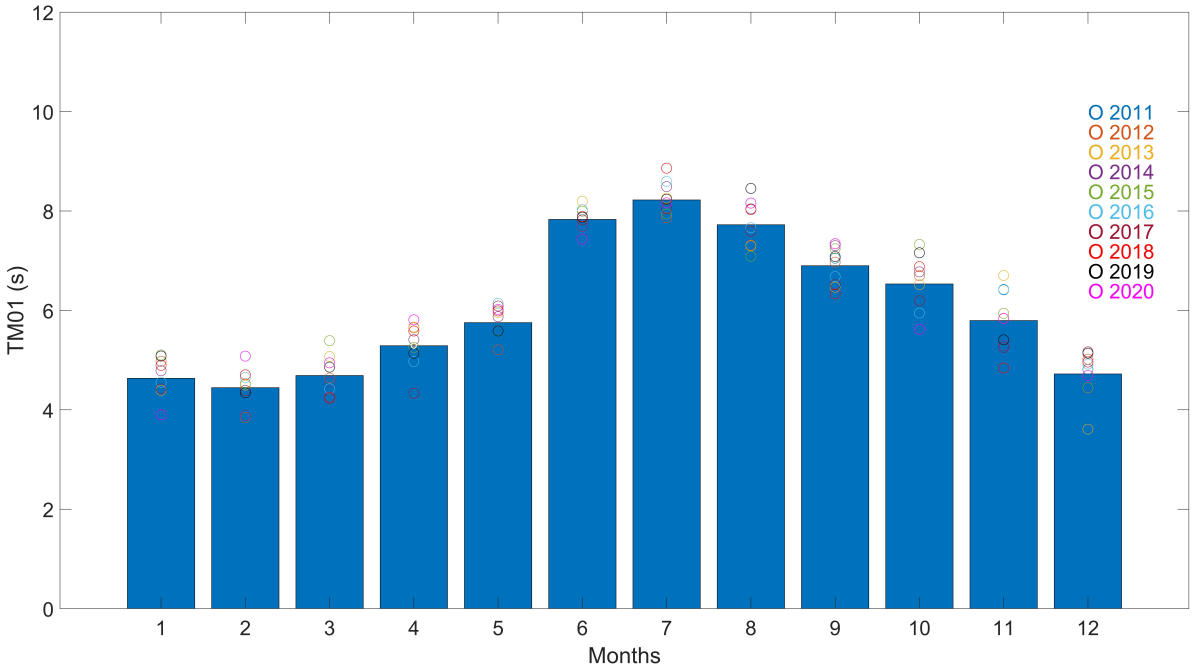

Figure 6.14: Monthly average distribution of TM01 over 10 years (2011-2020) at mid-breakwater location

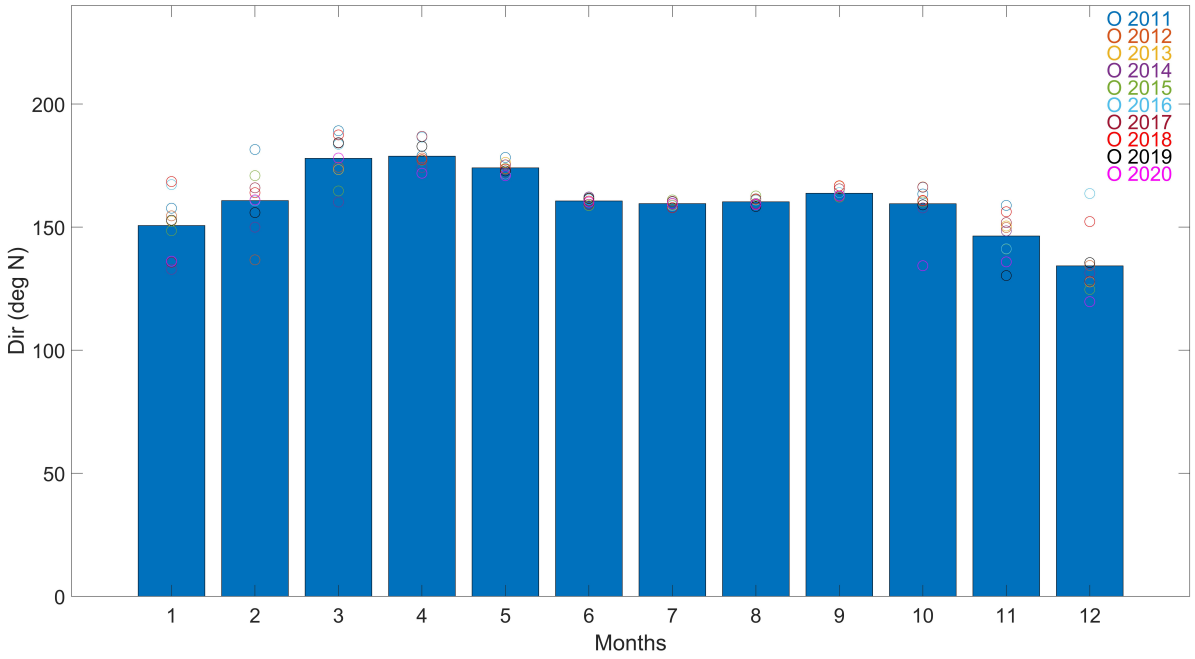

Figure 6.15: Monthly average distribution of D_m over 10 years (2011-2020) at mid-breakwater location

will be referred to as sea-states. Each sea-state is characterized by a unique value of Hs and Tp for which the joint probability (or percentage) of occurrence is found by means of creating a bi-variate histogram. This can be seen in figure 6.17 where the sea-states have been color coded based on the magnitude of their occurrence percentage. Additionally, contour lines for incident wave power in units of KW/m have been drawn to ascertain the power available in a sea-state. Based on this figure it can be seen that no particular sea-state dominates in Gwadar, rather a summation of multiple sea-states, each with minor occurrence percentages, make up the Gwadar wave climate. Therefore, is does not make sense to tune the U-OWC chambers for a single sea-state corresponding to the greatest incident wave power as it corresponds to a low occurrence percentage in a given year. Instead, it has been

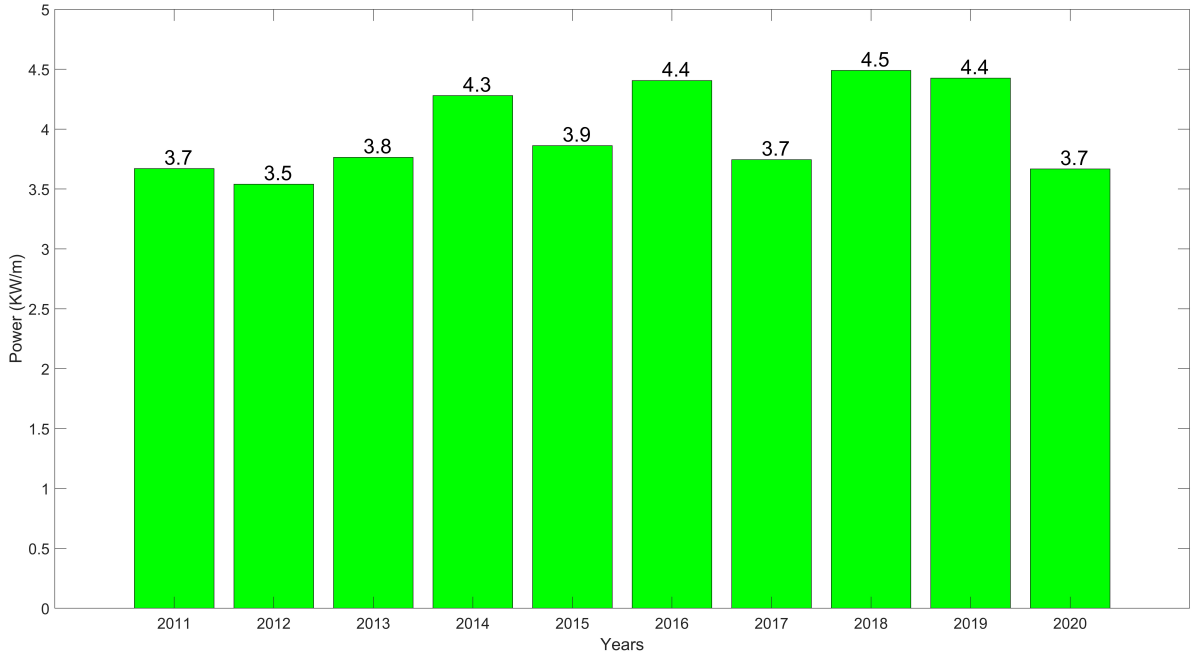

Figure 6.16: Year wise total incident wave power (KW/m) at mid-location of breakwater alignment from 2011-2020

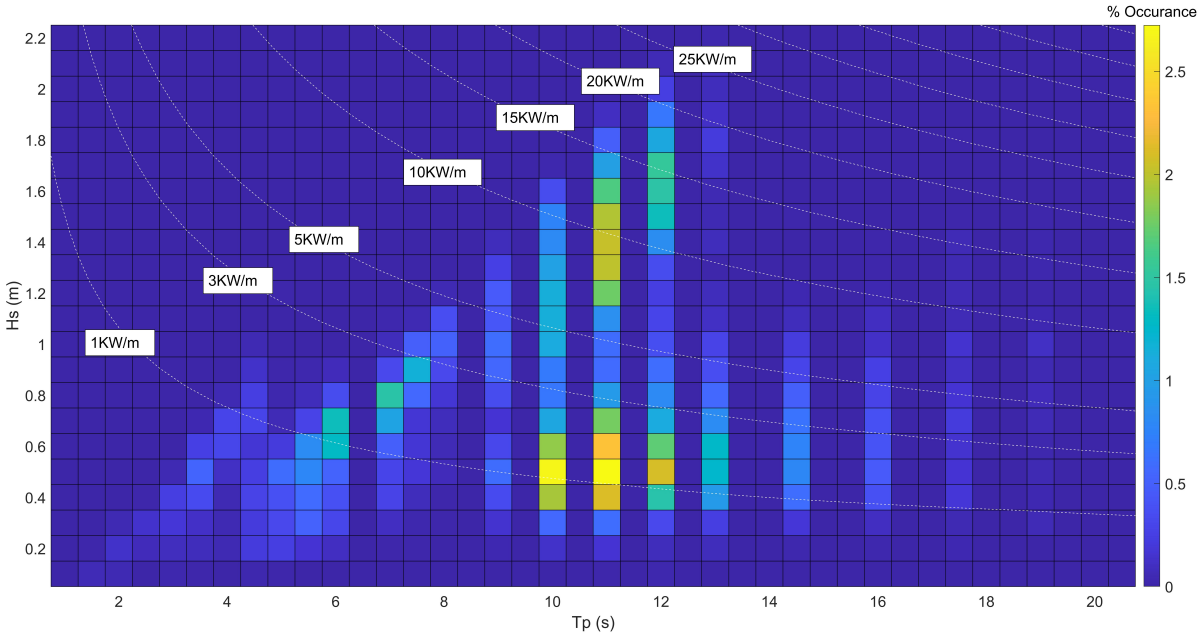

Figure 6.17: Gwadar wave climate occurrence matrix (2011-2020)

decided to tune the U-OWC chamber such that they maximize power conversion over 'n' number of sea-states, the selection criteria for which is a minimum threshold occurrence value taken as 0.5% in a year. Based on this, 60 design sea-states have been determined, the summation of which accounts for 71% of the time in a year during which the U-OWC device will operate - remainder is downtime. The sea-states that fall below the occurrence threshold are considered as statistically not relevant for the U-OWC design and have been ignored in the interest of minimizing computational time.

Figure 6.18 is a bubble plot of the 60 design sea-states that will be used to optimize the U-OWC chambers so as to maximize wave power extraction. As made evident by the bubble diameters, the left panel shows the occurrence percentage of each sea-state, the middle panel depicts the power for each sea-state, and the right panel depicts the product of the occurrence percentage times the power. More

details regarding the use of the sea-states in the design and optimization of the U-OWC chambers is discussed is section 9.

The results from the SWAN model help answer the first research question of this report which pertains to long term wave statistics of Gwadar. Based on the results the average incident wave power has been determined along with the identification of the dominant season, namely the summer monsoon. Lastly the wave climate has been condensed into 60 representative sea-states that will be used in the U-OWC device design.

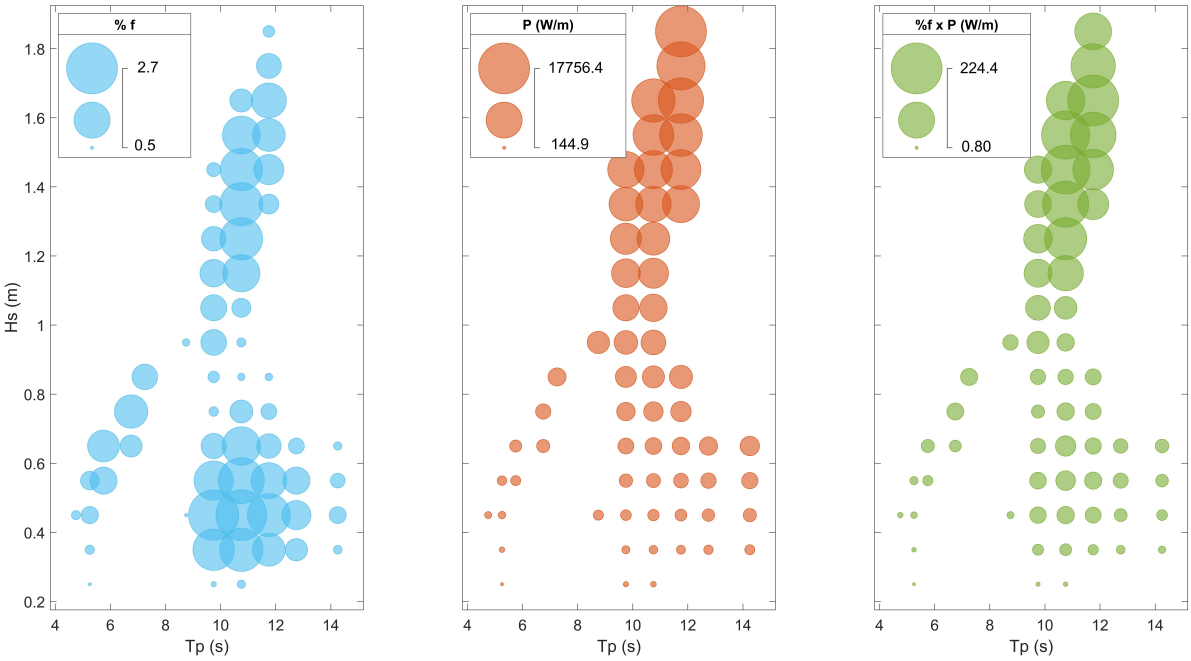

Figure 6.18: Design sea-states bubble chart plot.

7

Extreme Value Analysis

Discussed in this section is the extreme value analysis pertinent for the design of the breakwater integrated U-OWC device in Gwadar. Primarily, a WEC is designed to maximize on the amount of power that can be extracted from the local wave climate, however, its design should also be able to withstand extreme events. Therefore, mentioned in this section is the procedure to obtain the Hs value corresponding to the design return period.

7.1. Introduction and Methodology

For the case of Gwadar, the assistance vessel basin breakwater is assumed to have a deign life of $T_L = 50$ years. This assumption is based on the scale of investment taking place in Gwadar and the envisaged expansion of the port as detailed in its master plan - figure 5.1a. Additionally, based on the guidelines presented in PIANC Report n° 196-2016, a failure probability over the structure design life is taken as $p_{f,TL} = 0.15$ assuming a low risk to human life and medium economic repercussions in the event of failure. Given this information, the corresponding return period R_p for design can be calculated using equation 7.1 [56] and is equal to 310 years.

$$R_p = \frac{T_L}{-ln(1 - p_{f,TL})} \tag{7.1}$$

Now the task remains to find an Hs value corresponding to the design return period. This will be done by utilizing the peak over thresholds extreme value analysis technique in conjunction with the Generalized Pareto (GP) distribution. Equation 7.2 shows the cummulative exceedance function for the GP distribution which is characterized by a scale parameter σ_u, a shape parameter ξ, and a threshold value u [57]. Once these parameters are known, equation 7.3 [57] is used to translate the selected return period into a design value for Hs. In this equation, ζ_u is the probability associated with exceeding a particular threshold, and x_m is the value associated with a return period m [57].

$$H(x) = 1 - \left[1 + \xi \left(\frac{x - u}{\sigma_u}\right)\right]^{\frac{-1}{\xi}} \tag{7.2}$$

$$\begin{aligned} x_m &= u + \frac{\sigma_u}{\xi}\left[(m\zeta_u)^\xi - 1\right] , \quad if\ \xi \neq 0 \\ &= u + \sigma_u ln(m\zeta_u) , \qquad if\ \xi = 0 \end{aligned} \tag{7.3}$$

Now the main challenge is to filter the SWAN dataset to aggregate the extreme events that are independent in nature after which the GP distribution will be fit using carefully selected values for the free parameters, σ_u and ξ. To derive the extreme value dataset, a threshold value coupled with a de-cluster time will be imposed on the original SWAN Hs timeseries, where values $x > u$ was collected provided that they are at least the de-clustering time apart. The de-clustering time separation ensures that the collected exceedances are independent and homogeneous, complying with a fundamental assumption of extreme value theory. To assist in the selection of the threshold and de-clustering time,

the extremal index (EI) will be used. The EI value draws its roots from the fact that extreme event tend to occur in clusters and is defined as the inverse of the mean cluster size with a value ranging between 0-1, where values close to 1 signify a greater level of independence between extreme events [58].

To determine the free parameters σ_u and ξ that will characterize the GP distribution fit to the extreme value dataset, the maximum likelihood curve fitting technique will be used where the objective will be to minimize the negative log likelihood value (NLL). An NLL value closer to zero indicates that the choice of free parameters for the distribution capture the data well. Additionally, the goodness of the GP distribution fit will be assessed by the Akaike information criterion (AIC) and Bayesian information criterion (BIC). These parameters measure the quality of the statistical model by rewarding goodness of fit and penalizing unnecessary complexity, here values close to 0 are desired [59].

To perform the procedure outlined above and calculate the various parameters, the extRemes package in R developed by Eric Gilleland and Richard W. Katz will be used. For more information regarding the capabilities embodied in this package along with details for the equations and parameters mentioned above, the reader is pointed towards references [57] and [59].

7.2. Results

First the data from the near-shore SWAN output point is analysed. A quick check of the timeseries data reveals that a max Hs value of 2.55m is present, hence the threshold value must be less than this. Selecting a higher threshold value provides a greater degree of independence but comes with a greater risk of uncertainty as less data points are available to fit the distribution. Therefore, using the functionality of the extRemes package, a range of threshold values from 1.5-2.2m is tested. Figure 7.1 shows the confidence interval associated with a threshold value for the σ_u and ξ parameters. Based on this plot a threshold values of $u = 1.9m$ has been selected to strike balance between degree of independence and uncertainty. It can be seen that threshold values greater than 1.9m experience a much greater rise in uncertainty for both σ_u and ξ.

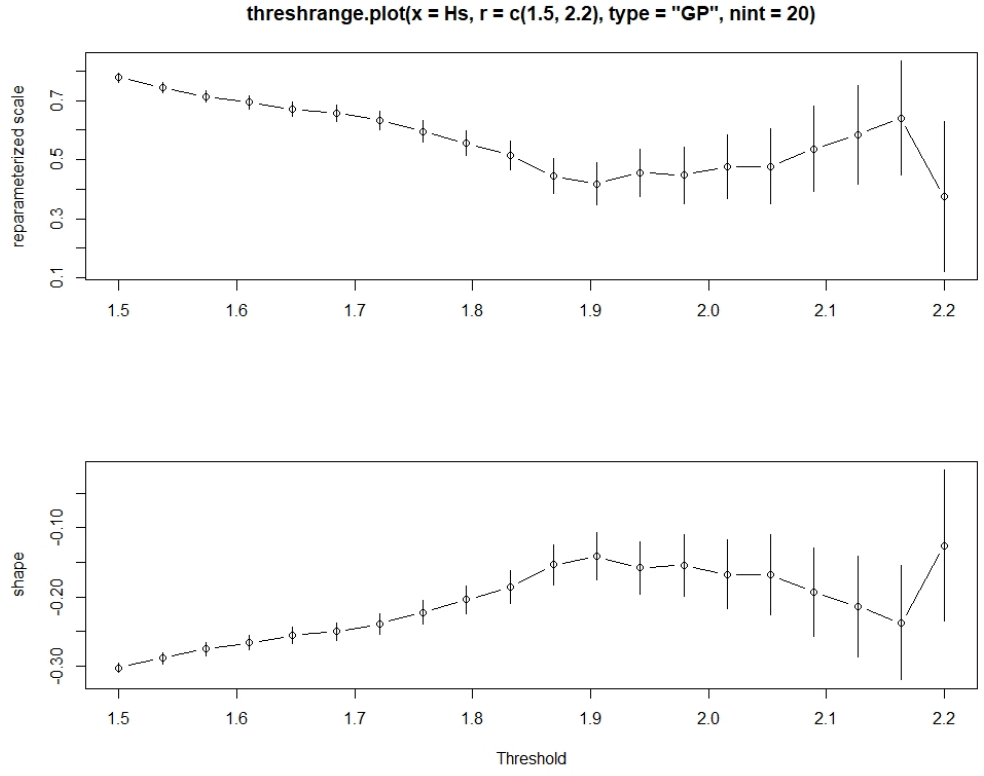

Figure 7.1: Threshold sensitivity analysis for the near-shore, confidence intervals depicted as lines.

Next, an appropriate de-clustering time needs to be determined for the selected threshold. This is

done by taking a de-cluster length of 0 hours as a base case, after which the de-clustering length is incrementally increased and the model performance is gauged by the EI, NLL, AIC and BIC values. Additionally, the error associated with the σ_u and ξ parameters is also monitored along with the number of samples obtained which tends to decrease with increasing de-cluster time. The results from this procedure are presented in table 7.1, where it can be seen that a de-cluster length of 72 hours yields the best results. This is indicated by an increase in the EI, followed by a reduction in the NLL, AIC and BIC values.

de-cluster(hrs)	no. samples	EI	NLL	σ_u error	ξ error	AIC	BIC
0	2937	0.008	-3040.68	0.003	0.017	-6077.37	-6065.4
10	89	0.29	-83	0.0247	0.117	-162.3	-157.3
24	60	0.43	-45.7	0.038	0.132	-87.47	-83.29
48	50	0.52	-35.36	0.04	0.13	-66.73	-62.9
72	43	0.6	-28.6	0.05	0.128	-53.2	-49.76

Table 7.1: Statistical model performance for a threshold $u = 1.9m$ at the near-shore

Based on the 72 hour de-clustered dataset with $u = 1.9m$, figure 7.2 highlights the selected extrema from the original dataset. Utilizing these extreme events, the GP distribution is fit with $\sigma = 0.261$ and $\xi = -0.322$. Figure 7.3 shows the visual result of the fitting compared to the empirical data. As can be seen, the GP distribution does a relatively reasonable job of capturing the empirical data.

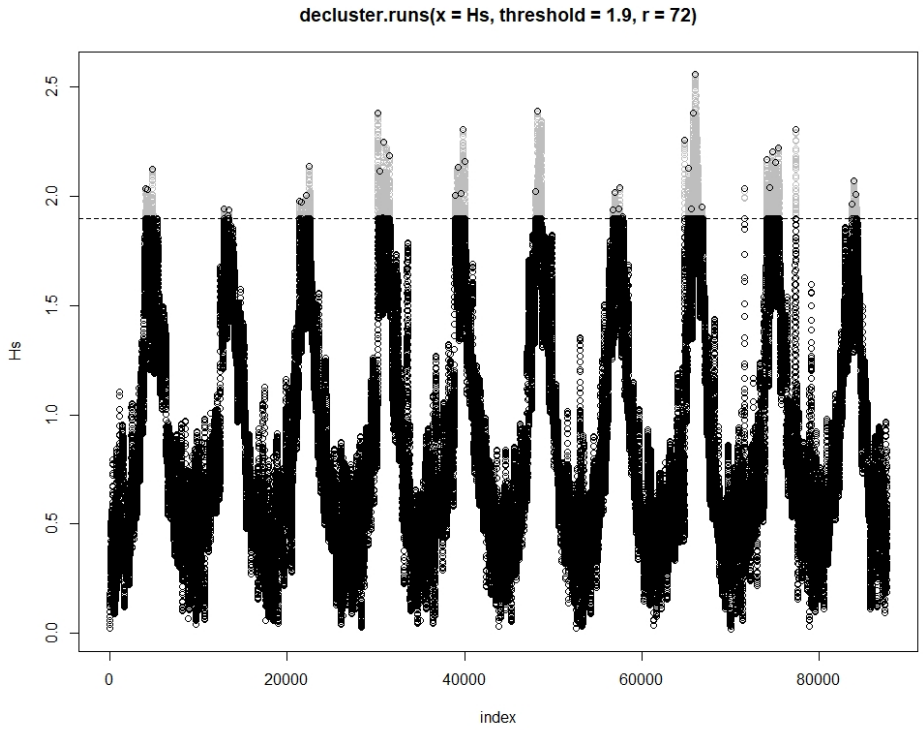

Figure 7.2: Scatter plot of selected extrema based for the near-shore

Now, given that the GP distributing fit has been finalized, a plot of return period and corresponding Hs value is created and presented in figure 7.4. Here the red lines depict the 95% confidence interval associated with a return period values. The procedure for calculating the confidence bounds is done via a bootstrapping technique available in the extRemes package. The bootstrapping procedure is sensitive to the number of runs simulated, and in this case an upper limit of 1000 was selected beyond which the program would crash. It was noted that the confidence intervals did not change going from 500 to 1000 runs, indicating that the solution had converged.

For better interpretation of the results, table 7.2 has been created where Hs values corresponding

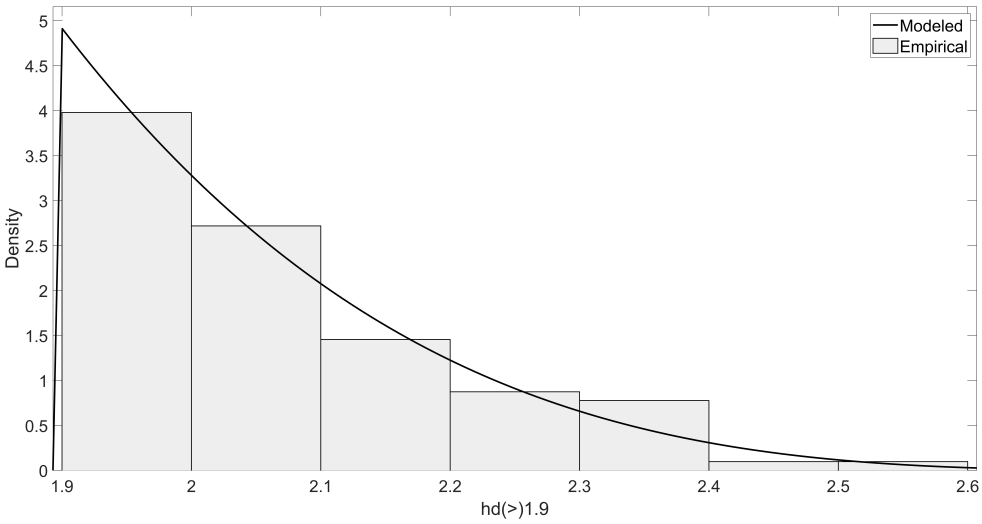

(a) Generalized Pareto distribution fit for Hs

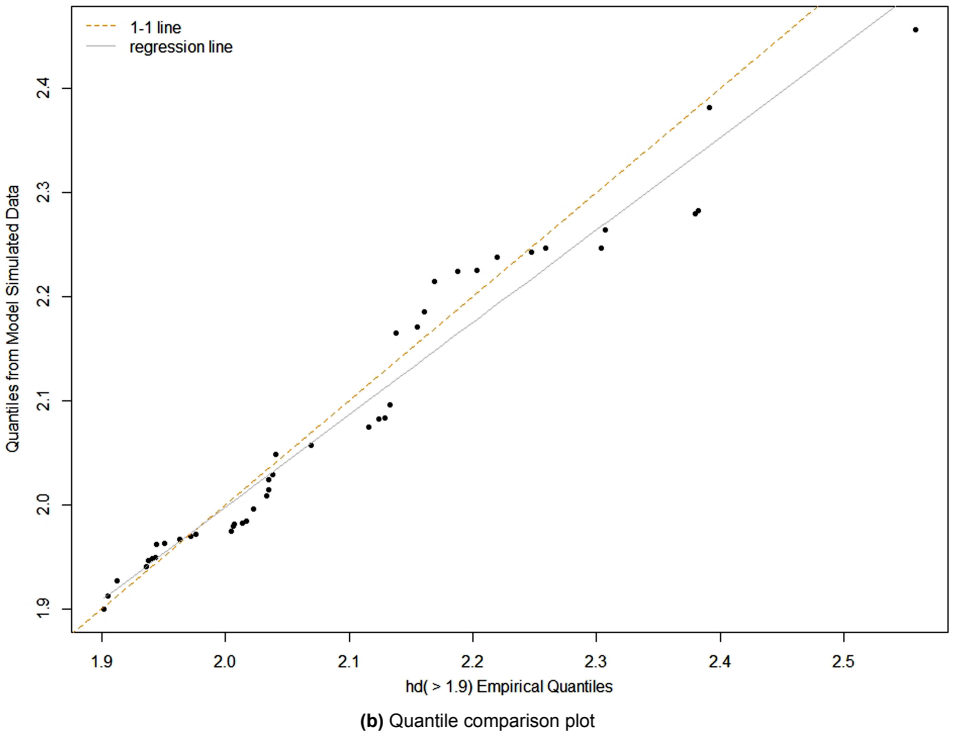

(b) Quantile comparison plot

Figure 7.3: Fit of the Generalized Pareto distribution at the near-shore, Hs $>$ 1.9m

to return periods ranging from 10 - 310 years have been shown. Additionally, the confidence interval associated with each return period are also indicated. The delta difference between the upper and lower confidence bound tends to increase with the return period which is as expected due to greater uncertainty surrounding these values.

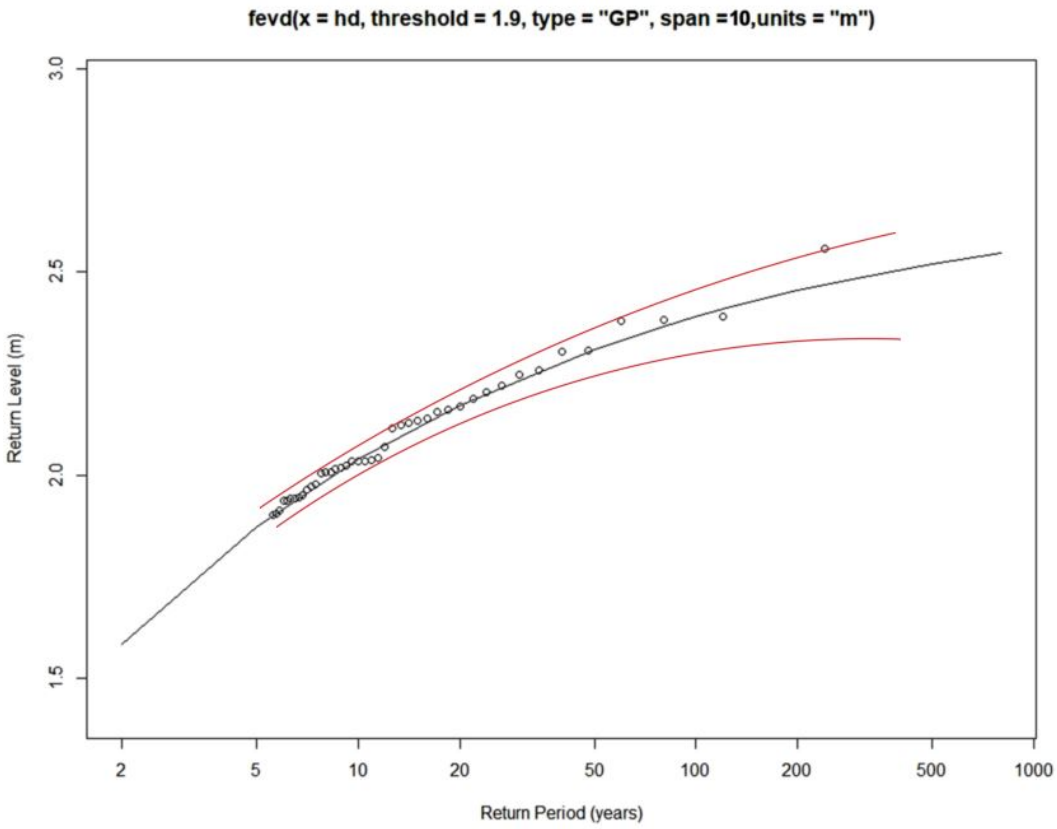

Figure 7.4: Return period and corresponding Hs value for the near-shore.

Return period (years)	lower bound (m)	value (m)	upper bound (m)	delta (m)
10	2.01	2.03	2.07	0.06
50	2.24	2.3	2.36	0.12
100	2.28	2.38	2.44	0.16
310	2.32	2.5	2.57	0.25

Table 7.2: Return period and corresponding Hs value at the near-shore

Following the exact same procedure as outlined above, an extreme value analysis has been performed for the off-shore SWAN output point to provide the reader with a comparison. The offshore results are presented directly in table 7.3 and as expected are relatively higher compared to the near-shore with the 310 year return period corresponding to a design Hs of 3.2m. For more details and plots for the offshore location the reader is pointed towards appendix A.

Return period (years)	lower bound (m)	value (m)	upper bound (m)	delta (m)
10	2.73	2.79	2.87	0.14
50	2.98	3.07	3.17	0.19
100	3.05	3.14	3.26	0.21
310	3.07	3.2	3.32	0.25

Table 7.3: Return period and corresponding Hs value at the off-shore

8

Tide

Discussed in this section is the tidal analysis at the proposed breakwater location in Gwadar. The analysis in its entirety has been performed using the T-TIDE package in MATALB developed by Rich Pawlowicz for which more information can be found at reference [60]. It is important to mention that a detailed tidal analysis is not within the scope of this report and has been performed only to the extent necessary. The findings of the analysis along with its use in the design and optimization of the U-OWC integrated vertical breakwater have been mentioned below, furthermore, these results will be utilized in section 9.

8.1. Tidal Results

The tidal analysis has been performed primarily for two reasons, which are mentioned as follows. The first reason pertains to the optimization of U-duct submergence, a parameter denoted by h as shown in figure 4.1. The submergence of the U-duct affects the power production of the U-OWC device as there will exist combinations of the tide jointly with waves that will leave the U-duct uncovered, halting power generation. Hence, the occurrence of these combinations need to be quantified for a particular value of the submergence. The seconds reason related more to traditional engineering, where the tidal analysis results will be used to calculate the design water level for the vertical breakwater based on the highest astronomical tide.

The tidal data measured by local consultants at the site has been provided to T-TIDE. The input data comprised of a 293 day tidal timeseries with a resolution of 10 minutes from which T-TIDE has calculated the necessary harmonic constituents, 59 in total. Table 8.1 highlights the 10 main constituents along with their amplitude and phase based on a 95% confidence interval. The full list of constituents is available in appendix B. Additionally, the signal to noise ratio (SNR) has also been mentioned which is defined as the squared ratio of the amplitude divided by the amplitude error which is readily calculated by T-TIDE [60] (see appendix B). It can be seen that the primary constituents exhibit a large SNR value as expected and comprise of both diurnal and semi-diurnal types. The character of the tide is further assessed by means of the form factor F, a ratio of the constituent amplitudes as given by equation 8.1 [61]. With an F value of 0.69 the tide in Gwadar is classified as the mixed semi-diurnal on the basis of table 8.2 below [61]. Also, it can be noted that the frequency of the M2 and S2 constituent are very similar. For this reason they interact resulting in the phenomenon of beats which gives rise to a spring-neap variability in the tide. Making use of equation 8.2 [61] where $\omega = 2\pi f$ is the angular frequency, the time between successive spring (or neap) tidal periods can be calculated as 14.8 days.

$$F = \frac{O1 + K1}{M2 + S2} = 0.69 \tag{8.1}$$

$$T = \frac{2\pi}{\omega_{S2} - \omega_{M2}} = 14.8\ days \tag{8.2}$$

The tidal timeseries supplied as input to T-TIDE is sufficiently long, thereby allowing for the constituents to be determined with a good level of accuracy. This is made evident by the low level of

Constituent	frequency (cycles/hr)	amplitude (m)	phase(°)	SNR
M2	0.08051	0.6434	300.15	31000
K1	0.04178	0.4074	52.81	11000
S2	0.08333	0.2516	333.64	5200
O1	0.03873	0.2078	49.84	3100
N2	0.079	0.1593	279.89	2100
P1	0.04155	0.1306	47.9	1300
K2	0.08356	0.0703	329.31	250
SSA	0.00023	0.0537	129.48	7.20
Q1	0.03722	0.0422	43.61	130
NU2	0.0792	0.0316	286.88	80

Table 8.1: Tidal harmonic analysis results for 10 primary constituents

Type	form factor (F)
semi-diurnal	0-0.25
mixed semi-diurnal	0.25-1.5
mixed diurnal	1.5-3
diurnal	> 3

Table 8.2: Tidal character classification based on form factor F [61]

amplitude and phase error which is listed in appendix B. Utilizing these constituents a preliminary tidal prediction is made to match the timestamps of the measured data by the tide gauge. Then a residual signal plot has been created as visible in figure 8.1 by subtraction the tide gauge measured values from the T-TIDE predicted signal. The residuals in the tide are mainly attributed to shallow water effects and the presence of land that give rise to multiple minor constituents the behaviour of which is difficult to predict. Based on the plot, the residuals are not large which is a positive finding and the data has an RMSE of 0.05m, an acceptable value.

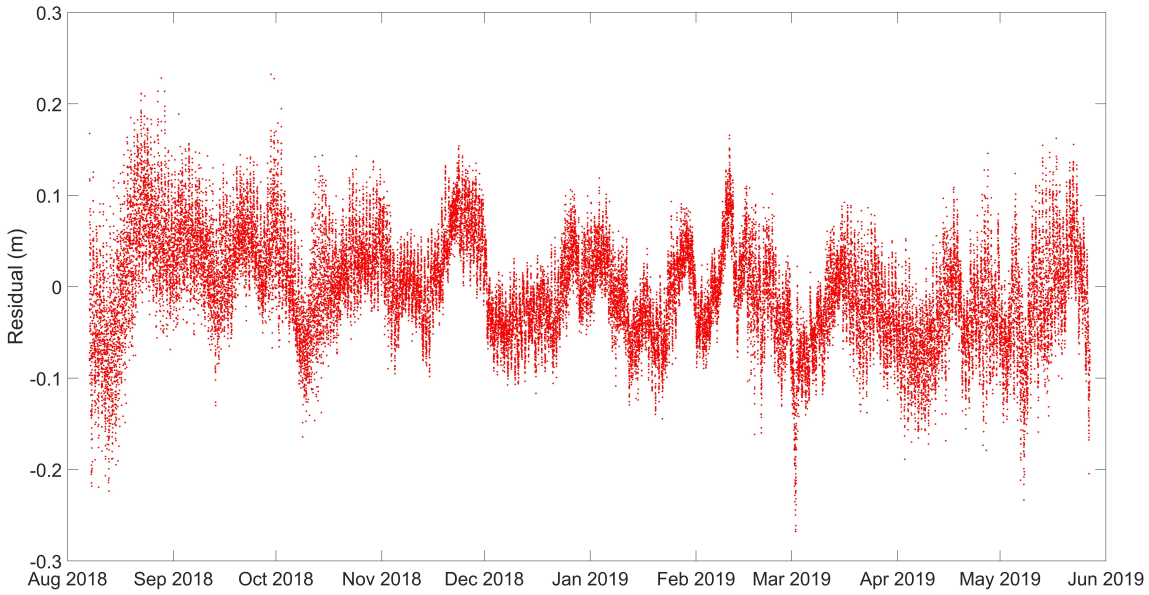

Figure 8.1: Plot of the tidal residual, observations subtracted from predicted data.

Given the validity of the tidal prediction results, the calculated constituents were used to perform a 20 year hindcast encompassing the time window of the SWAN model results. Based on the tidal hindcast the highest astronomical tide (HAT) equalled 1.33m, and the lowest astronomical tide (LAT) had a

value of -1.75m with reference to the mean sea level. Next, a subset timeseries of tidal amplitudes was isolated to match the SWAN simulation window between 2011-01-01 00:00hr to 2020-12-31 00:00hr. For this time frame the tidal amplitudes and corresponding Hs values were used to create a bi-variate histogram to analyse the joint occurrence probability of particular values occurring simultaneously. The results of this are presented in figure 8.2 below which highlights the chance (probability) of a particular combination of tidal amplitude and Hs occurring together. This results of this diagram will be utilized in section 9 together with a Boolean matrix corresponding to U-duct uncovering combinations to optimize the submergence value based on device downtime and annual energy generation.

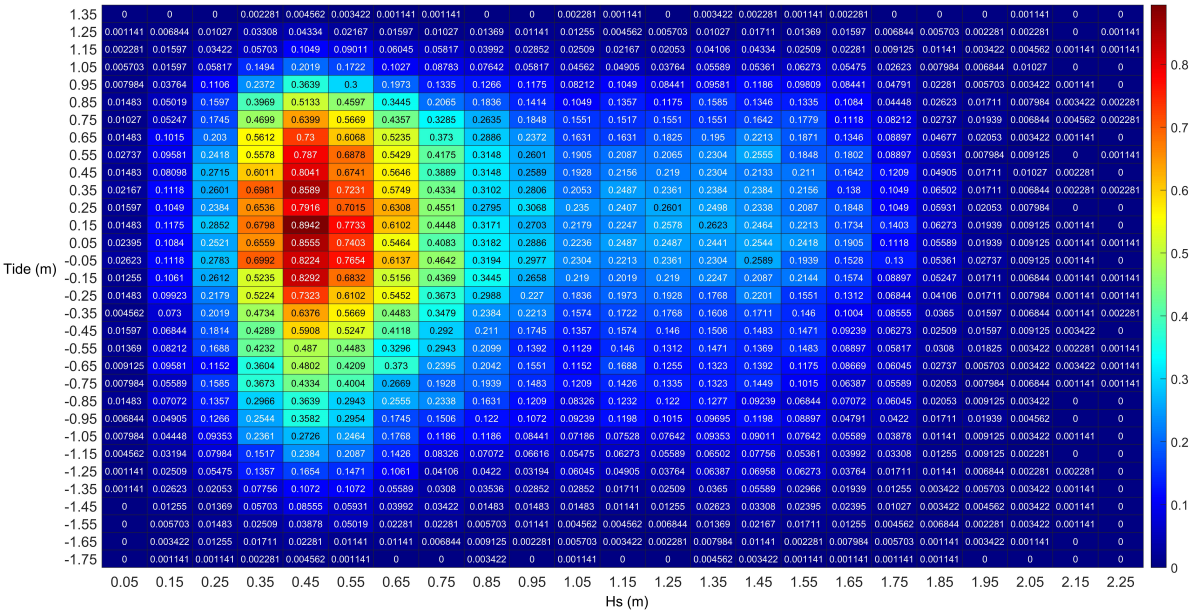

Figure 8.2: Joint occurrence probability diagram of tidal amplitude and Hs from 10 year dataset. Here the magnitude is expressed as a probability, all bins add up to 1

9

Design of the U-Oscillating Water Column

Discussed in this section is the design procedure for the vertical breakwater integrated U-OWC device as an alternative to the rubble mound breakwater suggested by the lead consultants. The results from the preceding section will be used to determine a feasible chamber geometry and turbine operating configuration. The primary objective will be to maximize the power conversion potential of the device, given that it will be situated in the low wave energy climate of Gwadar. Additionally, the integration of the device in a vertical caisson type breakwater will also be discussed.

9.1. Methodology

As a recap for the reader, breakwater option-3 as described in section 5.1, has been selected for a possible re-design utilizing vertical concrete caissons embedded with a U-OWC device. The alignment for this option is presented in figure 9.1, where it should be mentioned that only the north-eastern segment is of interest for U-OWC device integration due to the following reasons. This sections offers a superior orientation with respect to the incident waves that is favourable for the deployment of a U-OWC device in a terminator configuration. Evidence of this is found in the SWAN results of section 6.4, where the average angular obliquity between the wave ray and breakwater normal is within 12°. The north-eastern segment has a length of about 1.8km and thereby offers the largest capture width potential to harness wave energy, an important aspect considering the low levels of incident energy for the region. Additionally, the depth along this segment varies between 10-15m which offers a vertical caisson type breakwater the best chance of becoming financially competitive when compared against a rubble mound structure, the material quantities for which increase greatly with depth. Similar advantages for the short eastern segment located in shallow water cannot be found, hence it has been excluded from analysis and possibility of re-design.

Based on the results of the SWAN model, the project site experiences on average 3.9 KW/m of incident wave energy. This energy is the collective sum of 312 sea-states (number of bins in figure 6.17), each of which is characterized by a unique value of Hs, Tp, and occurrence probability. From further inspection it was found that the bulk of these sea-states correspond to very low occurrence percentages and Hs values that are too small for energy extraction by a U-OWC device. Therefore, the sea-states were filtered based on a minimum occurrence percentage criteria of 0.5%. As depicted in figure 6.18 of section 6.4, 60 representative design sea-states have been obtained that account for 3 KW/m of usable incident wave energy and make up 71% of the time in a given year, the reminder of which will be device downtime. Now the primary objective is the selection and optimization of the U-OWC chamber geometry along with a turbine configuration that will bring the power conversion of the device as close to the 3 KW/m benchmark as possible. The details for doing so have been mentioned below where all power estimations for the device will be calculated numerically via the codes described in section 4.2.

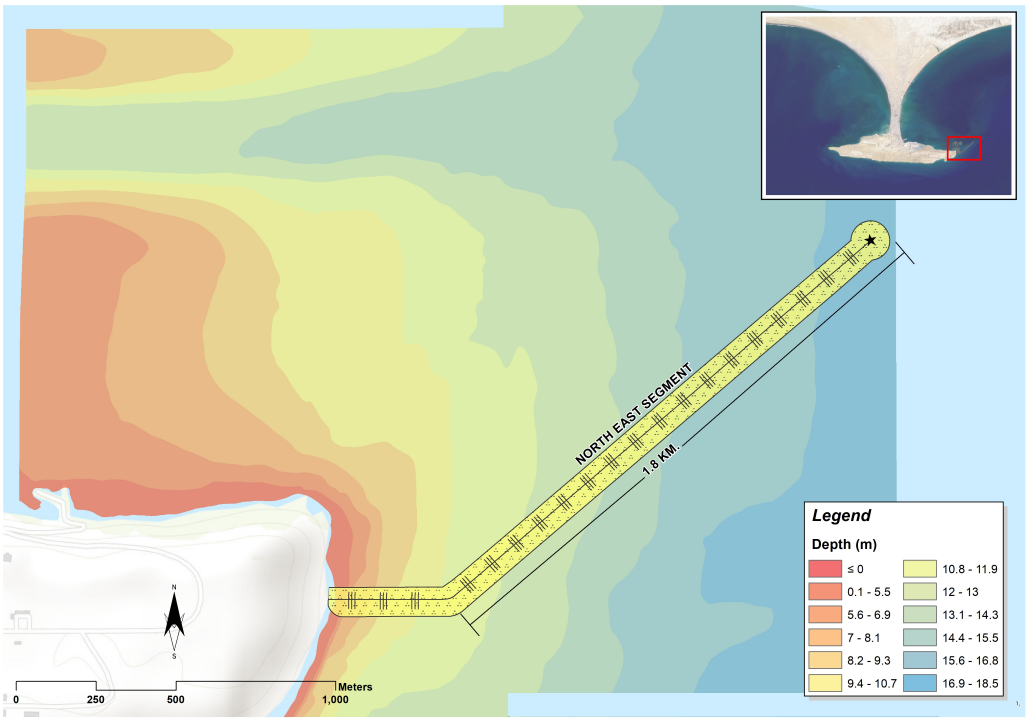

Figure 9.1: Breakwater option-3 alignment

9.2. Geometric Optimization

The selection for the U-OWC chamber geometry will be done so that it maximizes the power conversion summed across all 60 design sea-states, as opposed to encouraging resonance with a particular sea-state. This method has been adopted because the Gwadar wave climate is not dominated by a single sea-state of very high energy or occurrence. The parameters that need to be determined have been presented in figure 9.2, where the transverse width $b3$ has been fixed at 4m, similar to that of the Civitavecchia U-OWC, to avoid structural problems involving the use of a wide span subjected to wave force [35]. Constraints have also been placed on the outer and inner chamber width, namely b1 and b2, by keeping the values small (less than 2%) compared to the incident wave length to comply with an underlying assumption of fundamental U-OWC theory [62]. Also based on previous OWC type designs, as a general rule of thumb the ratio of $\frac{b2}{b1}$ should be approximately equal or close to 2 [62]. Lastly, for obvious reasons the air chamber height h_c should be large enough to prevent turbine submergence by inner chamber water level fluctuations during extreme conditions.

The mathematical determination of the various parameters to maximize converted power across 60 design sea-states is far from a trivial task. This is due to the fact that the U-OWC dynamics as mentioned briefly in section 4, are governed by equations that are a function of multiple inter-related quantities some of which are non-linear in nature. Hence, the separation of variable to find an optimal geometric configuration does not render itself to an analytical solution. Given that this is a complex problem involving multi-variable optimization simultaneously, a random sampling technique will be used followed by 'n' number of simulations. This technique will start off by defining an appropriate range of values for each geometric parameter to be optimized based on a step size, keeping in mind the constraints mentioned above and achievable construction tolerances. Once the range of values for each geometric parameter of interest have been defined, they will be stored in their respective column vectors from which 'n' number of samples will be drawn randomly from each, with replacement. This will be done with the help of the random.choice function available in the NumPy library of Python. The range of values defined for each of the parameters is shown in table 9.1. Each instance of sampled values across all of the necessary geometric parameters will be called a combination, and $n = 100$ such combinations will be simulated. Figure 9.3 depicts visually the random sampling technique procedure.

Each of the 100 combinations of geometric parameters will be tested against all 60 design sea-

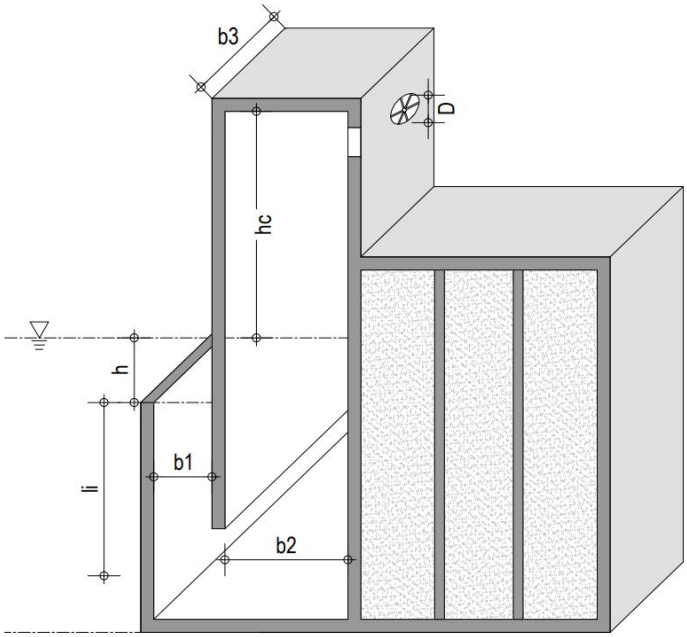

Figure 9.2: Geometric parameters for U-OWC device

Parameter	lower limit (m)	step size (m)	upper limit (m)
outer chamber width (b1)	1	0.2	2
inner chamber width (b2)	2	0.2	4
submergence of U-duct (h)	1.5	0.2	3.5
duct length (l_i)	2	0.2	8
air chamber height (h_c)	3	0.2	8

Table 9.1: Range of values for various geometric parameters to be stored in column vectors

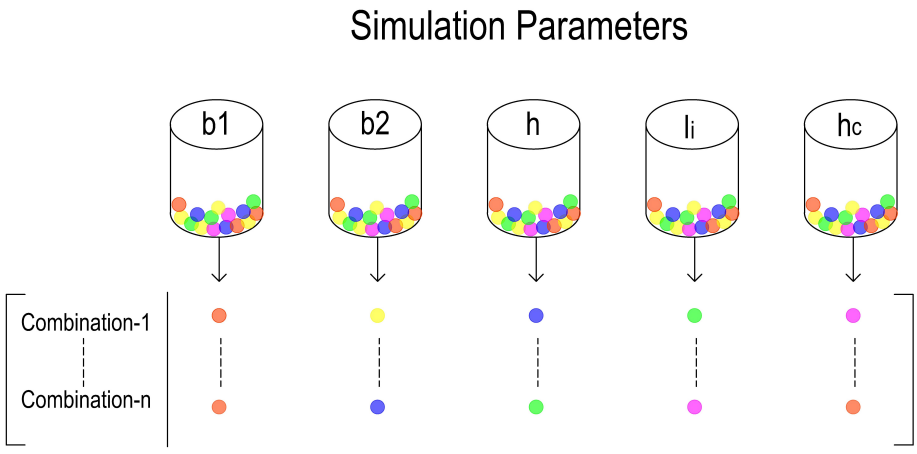

Figure 9.3: Visual depiction of random sampling technique

states. These sea-states will be provided as a matrix with dimensions 60x3 containing information on the Hs, Tp, and occurrence probability, as input to the numerical codes. The power converted by the U-OWC device for each sea-state simulated over a duration t = 30 minutes, will be determined,

multiplied by its occurrence probability, and then cumulatively summed. The combination that will yield the highest converted power as a sum across all 60 design sea-states will be selected for the design of the U-OWC chamber - subject to further optimization.

The results of the above mentioned procedure can be seen in figure 9.4, where the total absorbed and converted power across all 60 design sea-states has been plotted for n=100 combinations. It can be seen that combination 55 is most efficient as it results in the largest value of converted power, $Pc = 1.175KW/m$, the geometry for which is given below. A full list of the combinations along with power outputs is given in appendix C.

Combination 55	b_1 = 1.8m	b_2 = 3.8m	h = 1.7m	l_i = 6.2m	h_c = 7m

Coincidentally, it can be seen that the geometry of combination 55, is similar to that of the Rocella Jonica U-OWC (details provided in section 3.4), a device also designed for deployment in a low wave energy climate. Hence, this inspires confidence in the design procedure being used here.

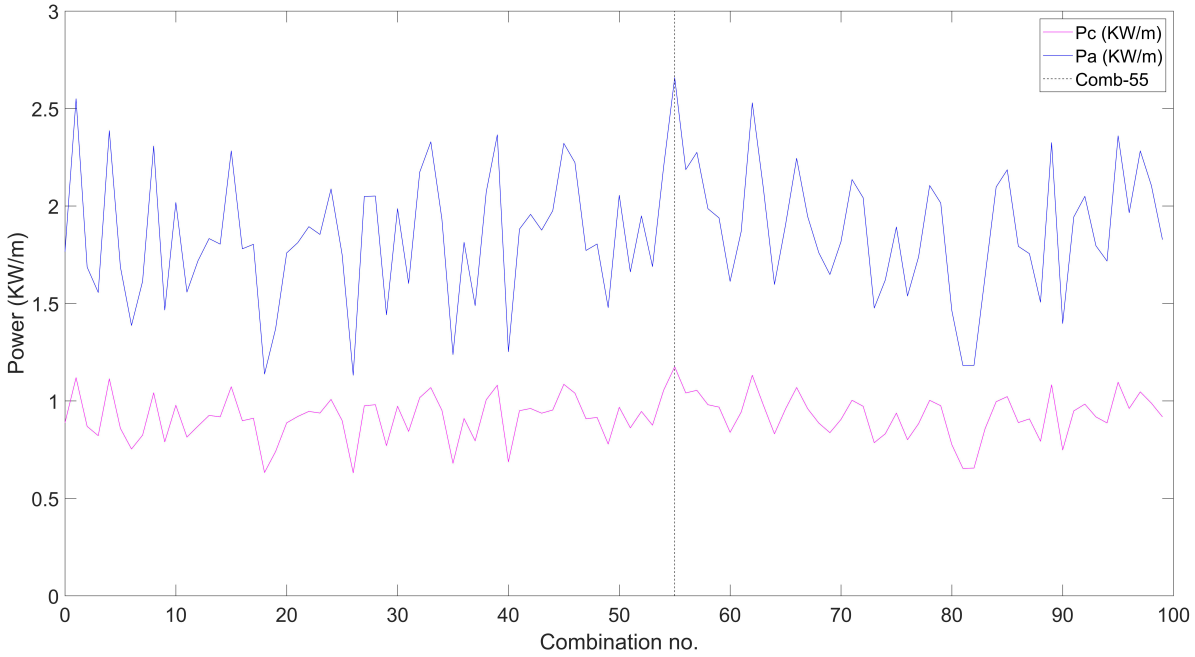

Figure 9.4: Power output (absorbed and converted) for simulated combinations

Based on the results of figure 9.4 and the procedure outlined above it is important to mention the following:

- All power results have been obtained using numerical codes which contain pre-defined values for frequently used constants. Two constants worth mentioning are C_{dg} and C_{in} which control the continuous steady, and unsteady headloss in the U-OWC device. They have been assigned values of 0.71 and 0.13, based on a physical full scale experiments involving a U/OWC type device.
- The depth along the breakwater segment of interest is between 10-15m, therefore an average depth of 13.5m has been simulated. Based on a preliminary check, the power results are not sensitive to depth given the low Hs values in the 60 design sea-states being simulated.
- The presented results are for a single U-OWC chamber, not an array configuration which will be simulated at a later stage.
- The power numbers have been divided by the transverse chamber width b3 = 4m, and therefore are in units of KW/m.
- The absorbed power (Pa) is what the device can capture in its inner chamber. However, for the end user the power that the turbine can successfully convert (Pc) is the quantity of interest. Going from Pa to Pc, an approximate 47% energy loss is experienced based on the data presented in figure 9.4.

- A self-rectifying Wells turbine is being used to go from Pa to Pc. At this stage a typical value of turbine diameter d= 0.9m and constant revolutions per minute of 3000 are being used. These quantities will be optimized in the proceeding section based on the turbine efficiency curve.
- The U-duct submergence denoted by h, will be optimized further in conjunction with the tide and waves to minimize device downtime due to U-duct un-covering in the proceeding section.
- The simulation (along with future runs) have been performed with an average value of wave obliquity equal to 8° at the mid point of the north-eastern breakwater alignment. Changing the obliquity by plus or minus 5° shows negligible changes in the results.

9.3. Chamber Coupling and Turbine Optimization

Moving forward with the geometric parameters determined in combination 55, the aspect of air chamber coupling is investigated. As proven beneficial in the case of the Rocella Jonica U-OWC [34], air chamber coupling can potentially increase converted power and save cost while doing so as less turbines are required. In this regard, the numerical codes were modified to allow for the coupling of 'n' connected air chambers while keeping the oscillations of the water column independent. The results of this are depicted in figure 9.5 for up to 3 connected air chambers simulated for varying turbine diameters with a constant rotational speed of 3000rpm (typical value). Here the capture width ration (CWR) is defined as $\frac{Pc}{Pi}$, where Pc has been determined across all 60 design sea-states. Based on the plot it can be seen that the largest value of capture width ratio of 0.34 is for a single un-coupled air chamber with an optimal turbine diameter of 0.9m. Given the complex dynamics of the system, the results are not always intuitive and for the case of Gwadar, the aspect of chamber coupling does not yield a fruitful outcome. Therefore, it has been decided that U-OWC air chambers will operate independently without coupling for the Gwadar breakwater as this configuration provides a significantly better capture width ratio compared to 2 or 3 coupled chambers. From this point onwards, all runs will be performed with a turbine diameter of 0.9m.

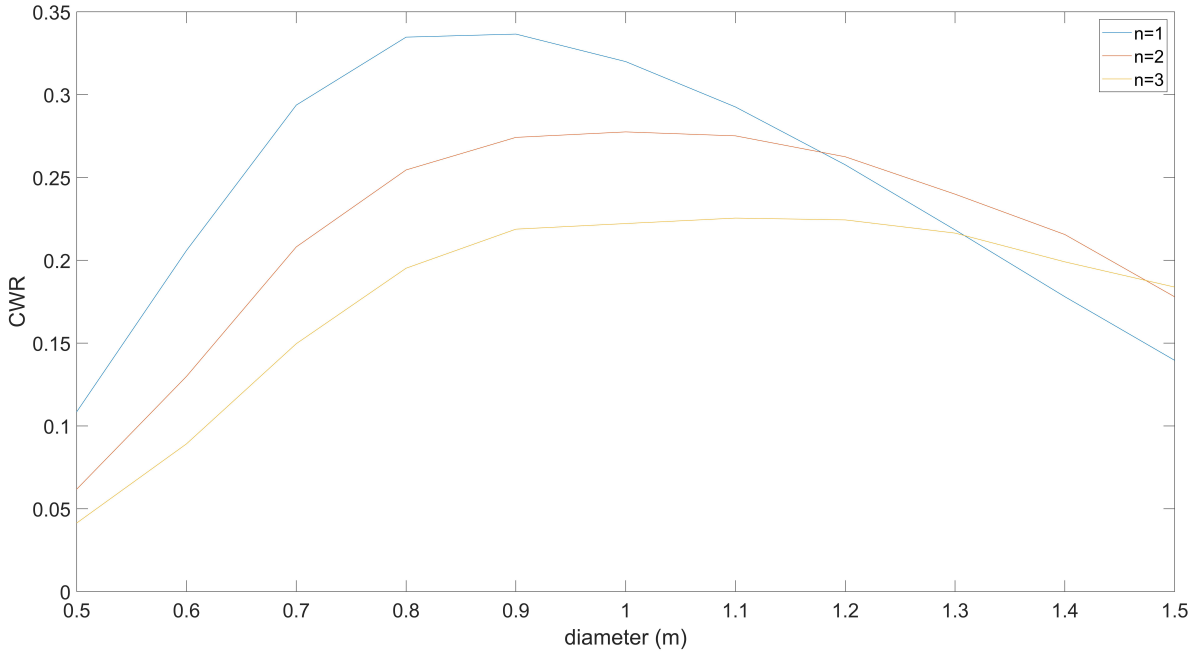

Figure 9.5: Capture width ratio (CWR) for coupled air chambers across varying wells turbine diameters

Now a stage has been reached where it is important to study the wells turbine behaviour, in particular its rotational speed. Up till now, a constant rpm value of 3000 had been assumed for the turbine operation across all 60 design sea-states. However this is not ideal, as the wells turbine offers only a narrow bandwidth of high efficiency when subjected to a range of differential pressure heads, as mentioned earlier in section 3.3. Typically, in the case of a U-OWC device the wells turbine is coupled to a generator via a feedback control system which imparts a necessary torque on the turbine to govern

its rotational speed [29]. In doing so, the turbine can operate at its best point of efficiency for a particular value of differential pressure between inner chamber and atmosphere, thereby maximizing converted power.

As mentioned in the paper of Scialo et al (2021), equation 9.1 can be used for the implementation of turbine control. Here, I is the moment of inertia, N the turbine revolutions in radians per second, P_{ctrl} the magnetic power of the generator, and P_{turb} the turbine power. Further it should be mentioned that P_{turb} is a function of the turbine diameter, revolutions to the cube (N^3), and the dimensionless flow rate Ψ (see equation 4.16, section 4) at the best efficiency point based on turbine model specific curves. More detailed information regarding turbine/generator control can be found at reference [29].

$$\frac{d}{dt}\left(\frac{1}{2}N^2\right) = \frac{1}{I}(P_{turb} - P_{ctrl}) \tag{9.1}$$

A full turbine control algorithm has not been implemented in this report as this is a task of an electro-mechanical nature for which model specific parameters are required. Additionally, it will introduce a layer of complexity not required for a feasibility level design. Nevertheless, a technique has been implemented to mimic the effect of a turbine control system to produce realistic converted power numbers, while avoiding unnecessary complexity, and has been defined below.

Given the fact that the numerical codes already include an efficiency curve for a specific Wells turbine, simulations have been performed for each of the 60 design sea-states subjected to turbine rotational speeds ranging from 50 - 400 radians per second. The rotational speed resulting in the highest conversion efficiency for each sea-state has been stored in a column-vector, which will be provided as input for all subsequent runs. Figure 9.6 highlights the conversion efficiency, color coded by magnitude, across a range of rotational speeds for each sea-state. By specifying optimal turbine rotational speeds for each sea-state, the conversion efficiency of the U-OWC device increases by 3% compared to the prior run utilizing a constant value of N=3000 rpm.

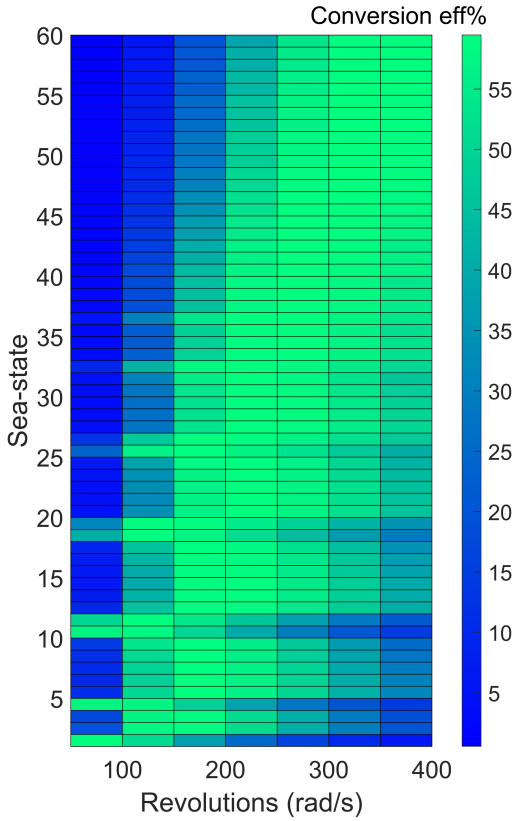

Figure 9.6: Conversion efficiency for varying rotational speeds across design sea-states

9.4. Optimization of Submergence

As a next step to maximize the power generation of the U-OWC device, the submergence of the U-duct denoted by h along with the duct length l_i needs to be optimized. These parameters have been indicated previously in figure 9.2. It is assumed that a change in U-duct submergence will be accompanied by a change in the duct length, and the combination of these two parameters will impact the power conversion of the device along with downtime. The device will cease to produce power if the U-duct is not submerged. The objective is to select a combinations that maximizes the Kilo Watt hours of energy produced in a year, which is a product of the converted power multiplied by the net annual operational hours of the device. The procedure outlined below has been performed to accomplish this task.

- The reader is made to recall the results of figure 8.2 in section 8, where the probability of a particular tidal amplitude and significant wave height occurring together is mentioned - this figure will be called the T-matrix.
- For each possible combination of tide and wave height, the submergence state of the device is determined with a Boolean value of 1 or 0, where 1 implies un-submergence of the U-duct. The state is determined by equation 9.2, where Ta is the tidal amplitude, Hs the significant wave height, Hm the mean wave height [1], and h the U-duct submergence. Figure 9.7 is an example of possible submergence states [0,1] for an h = 1.7m and is called the state-matrix.
- To calculate device downtime, the state-matrix for a particular value of h is element wise multiplied by the T-matrix and all entries are summed. This procedure is repeater for h values ranging from [1-2.5m].
- Given a value of downtime, the net operational hours of the device are calculated and multiplied by their converted power to calculate annual energy production in units of KWh for various configurations

$$\begin{aligned} B &= (T_a + h) - Hm/2 \\ Hm &= 0.588Hs \\ if B < 0, \quad Boolean &= 1(un - submerged \;\; duct) \\ if B > 0, \quad Boolean &= 0(submerged \;\; duct) \end{aligned} \tag{9.2}$$

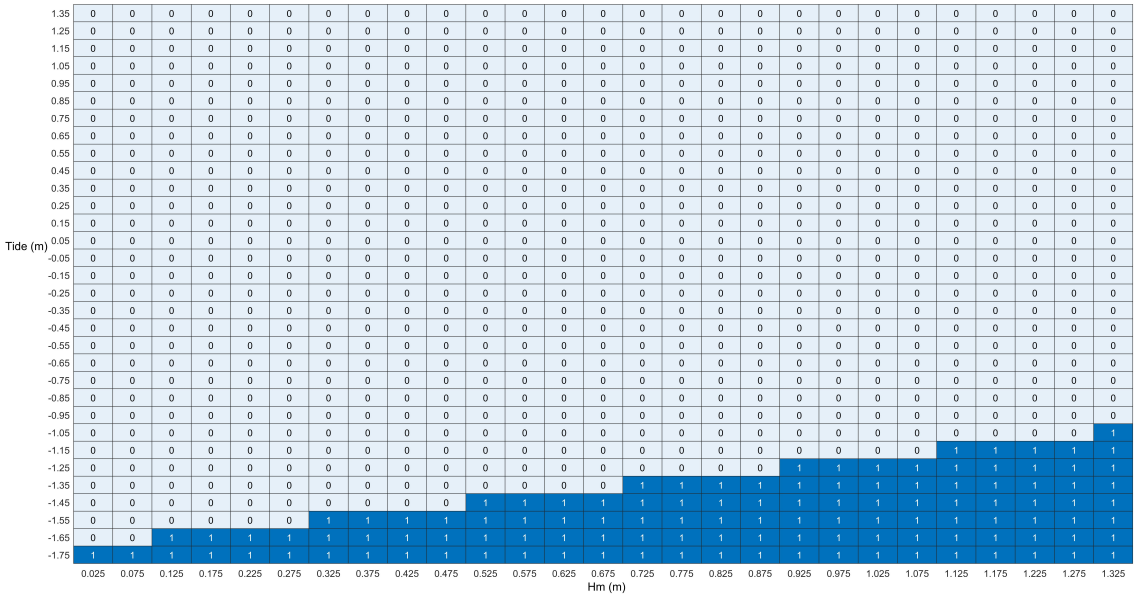

Figure 9.7: Submergence combinations for h= 1.7, un-submerged conditions correspond to a value of 1

[1] Hs is converted to Hm using the relationship presented in reference [56] assuming a JONSWAP spectra and deep water

The results of the method outlined above are presented in table 9.2 below and it can be seen that lower values of submergence lead to a greater magnitude of down time. The net operational hours are calculated by subtracting the down time from the devices intended operational time of 71% in a year. It can be seen that h=2m and $l_i = 5.3m$ maximize the annual energy with a value of 22875.8 KWh, and hence has been selected for the final design. As a note, the presented energy outputs are for a single U-OWC chamber with b3 = 4m.

h (m)	l_i (m)	Pc (KW)	down time (hr)	Net op-time (hr)	energy (KWh/year)
1	6.3	2.95	794.9	5424.7	16003
1.5	5.8	3.47	154.2	6065.4	21034.6
1.7	5.6	3.43	56.6	6163	21139.1
2	5.3	3.68	6.8	6212.8	22875.8
2.5	4.8	3.66	0	6219.6	22763.7

Table 9.2: Annual energy production for various submergence (h) and duct length values (l_i)

9.5. Final Power Output

Up till now all output power numbers have been calculated for a single U-OWC chamber operating in a stand along configuration. However, given that the north-eastern segment of the Gwadar breakwater will be 1.8 km long, it will comprise of multiple U-OWC chambers operating simultaneously in an array configuration. Based on the work of Malara and Arena (2019), for which more information can be found at reference [50], U-OWC's in an array configuration suffer from the park effect. The park effect is defined as a reduction in conversion efficiency of U-OWC's configured in an array, compared to a stand along case because of the interaction effects between diffracted and radiated waves from adjacent chambers [50]. Malara and Arena mention a parameter q to quantify the efficiency reduction of an array with j chambers as given by equation 9.3 below. Their findings suggest that the q value decreases from 1 (single chamber) to approximately 0.8 for arrays with j=10, beyond which it stabilizes - no further reduction in power with increasing array length.

$$q = \frac{1}{jPc_{i=1}} \sum_{i=1}^{j} Pc_i \tag{9.3}$$

Based on the design of the U-OWC chamber at present, the converted power was calculated for varying array lengths with j ranging from 1 - 10. Figure 9.8 shows how the q factor decreases for increasing values of j. As documented in literature, a decrease of about 20% is experienced beyond which the line is expected to stabilize [50]. Given a chamber width b3 = 4m with a typical value or wall thickness of 0.4m, approximately 375 (1800/4.8) U-OWC chambers can be integrated in the north-eastern segment of the Gwadar breakwater. It is simply not possible to model an array of this length as it would require a system with 375x2 = 750 degrees of freedom (1 DOF for each independent water column, and air chamber), the computational time for which would be extraordinary. Hence an array with j=10 chambers will be used to determine the final power numbers for the Gwadar breakwater (north-eastern segment), the results of which will be scaled by an integer N. An array length of 10 chambers is approximately 48m, hence N=37.5 arrays of j=10 chambers will be integrated in the 1.8km long breakwater segment.

Having determined an ideal U-OWC chamber geometry each with its own turbine, the final power and energy conversion results of the device are presented in table 9.3. The reader is pointed to appendix C for power results of each chamber in the array. Based on this data, another research question as outlined in section 1.3 can be answered. For the low incident wave energy climate of Gwadar, the device in its entirety can produce 1.1MW of usable converted power and generate 6.8GWh of energy based on an operational time of 70.5% in a year. Given these numbers, the benefit of a large capture width made available due to the long length of the breakwater (1.8km), are immediately obvious despite the low wave energy native to the region. If constructed, this device would be one of the largest of its kind in terms of power generation in the world (see table 3.2).

The efficiency numbers for the final device design are presented in table 9.4. As stated earlier in this section, the goal was to maximize the value of Pc and bring it as close to Pi as possible. Given a

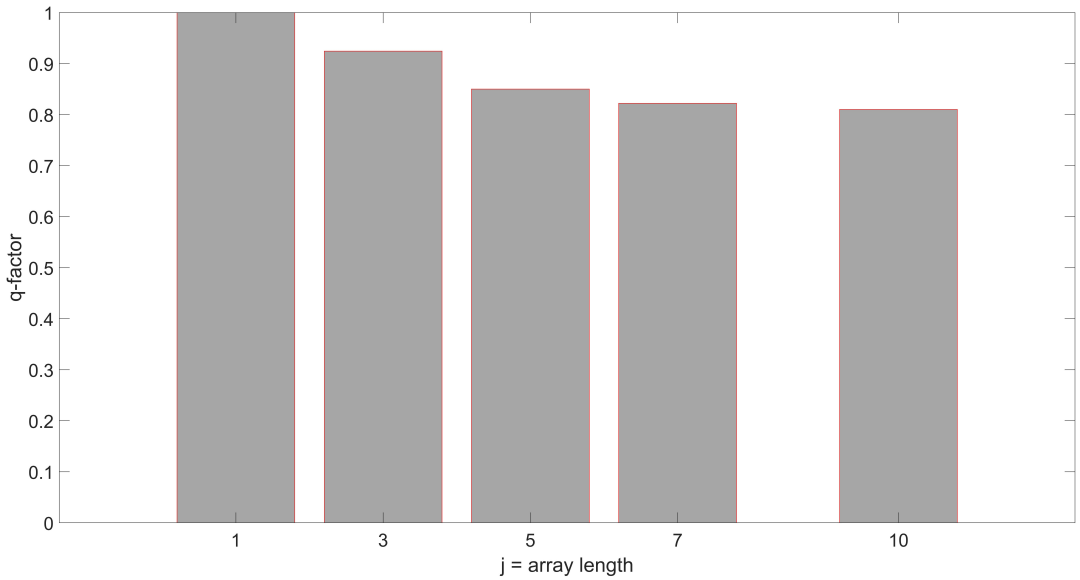

Figure 9.8: Effect of array length j on q factor

$Pc_{j=10}$ (KW)	N	Pc_{total} (MW)	Net Op. (hours)	Energy (MWH/year)
29.8	37.5	1.1	6212.8	6834.1

Table 9.3: Total U-OWC converted power and energy for north-eastern breakwater segment, Gwadar

potentially usable Pi = 3 KW/m, the device in its most realistic configuration is able to convert 25% of this power resulting in a Pc = 0.74 KW/m. This is a reasonable result for a U-OWC type device and future advances in turbine efficiency can help improve this number. Lastly, the performance of the final design can also be seen for each of the 60 design sea-states as shown in figure 9.9. Here the diameters of the bubbles in the left panel show the incident power and the bubbles in the right panel depict the converted power for each sea-state. It can be seen that the final device configuration performs as intended, made evident by a similar trend in bubble diameters between incident and converted power. Hence it can be said that the device has been tuned such that is maximizes power conversion across all the design sea-states.

Pi (KW/m)	Pa (KW/m)	Pc (KW/m)
3.0	1.26 (42%)	0.74 (25%)

Table 9.4: Final U-OWC design, device power and efficiency per meter width

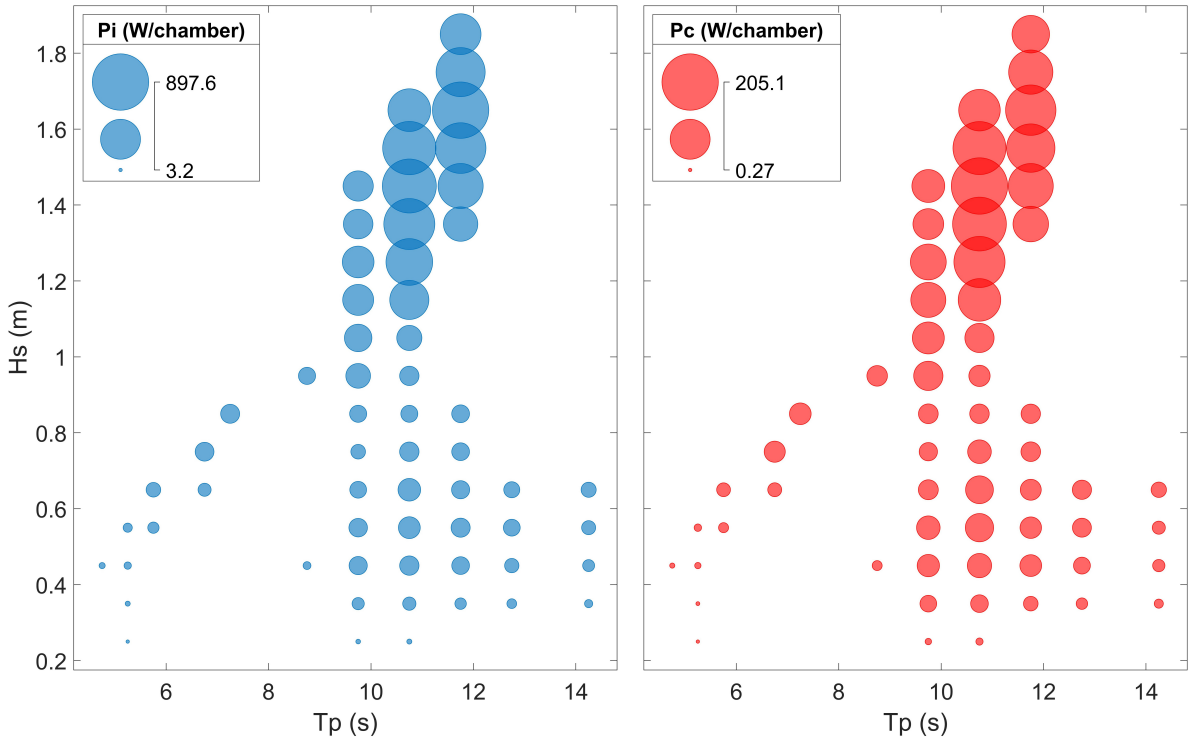

Figure 9.9: Incident and converted power per chamber (b3 = 4m), for final U-OWC design across 60 design sea-states

9.6. Vertical Breakwater Design

At this stage, given that the U-OWC chamber geometry and optimal turbine configuration have been determined, it is necessary to design the vertical caisson breakwater in which the device will be integrated. The vertical breakwater will be designed according to the Goda method, the details of which can be found in Takahashi (1996) [63] and Goda (2000) [64].

As mentioned previously, the north-eastern segment of the Gwadar breakwater experiences a depth variation between 10-15m. It has been decided to embed the U-OWC chambers into vertical reinforced concrete caissons placed on top of a shallow rubble mound foundation. The level of submergence of the U-OWC duct will be fixed at h=2m with reference to the mean sea level (msl), and variations of the local bathymetry along the breakwater alignment will be dealt by altering the rubble mound foundation height.

Geo-technical aspects pertaining to the design of the breakwater both original, and its re-design with vertical caissons embedded with U-OWC's, are not included in this report. This is done because of the limited geotechnical information available and to avoid significant complexities.

The results of the design have been present here directly, as an alternative to the rubble mound structure proposed by the lead consultants for breakwater option-3. A detailed structural design has not been undertaken, rather a typical concrete wall thickness of 0.4m, as used in the Civitavecchia U-OWC [62], has been assumed with a steel reinforcing of 150 kg/m^3. The reader is pointed towards appendix D for relevant design calculations.

Tables 9.5 and 9.6 below list the safety factors for the caisson stability along with primary design parameters. As can be seen, the safety factors for sliding and overturning are above the 1.2 threshold as specified in [63]. The armor layer has been designed according to the procedure outlined in Takahashi (1996) in terms of the stability coefficient N_s, and a foot protection block has been sized for placement directly in front of the structure where a standing wave pattern can develop. Given the structures dimensions, the depth of the toe is out of range for the traditional equation involving the N_{od} parameter as $(h_t/Hs > 2)$, where h_t is the depth above the toe and Hs is the significant wave height. Therefore, the wave induced bed shear stress is used to calculate a stone dn50 value based on the Shields approach. The under layer has been sized according to the guidelines mentioned in Schiereck (2017) [65] for geometrically closed filters subject to wave loading and their corresponding layer thick-

ness has been calculated by the procedure outlined in chapter 3 of the Rock manual (2007) [66]. An overtopping discharge of less that 10 L/s per meter has been set as a limit according to the guidelines specified in the EurOtop manual (2018), and it is assumed that the turbine housing will be water proof against overtopping discharge. The lee side of the caisson will comprise of sand ballast with a free board of $+1mDWL$ and can be used as a walk way.

The various layer gradings and their corresponding thickness are mentioned in table 9.7 below. A drawing is also provided for the deep and shallow water sections which are at a depth of 15 and 10m from MSL in figures 9.12 and 9.13 below. Lastly, a basic 3d model of the U-OWC integrated vertical caisson breakwater is depicted section 9.7 below.

Breakwater type	Vertical caisson
Foundation	Shallow rubble mound
Design life (years)	50
Depth	(10-15) m MSL
HAT	1.33 m MSL
Hs (R=310 years)	3.2m
H_D (R=310 years)	6.34m
T_D	14.7s
L_D	170m
DWL	+1.5 m MSL
Crest height	+7.4 m MSL

Table 9.5: Design parameters for U-OWC vertical caisson breakwater

Failure mode	Limit state	Design value	pf_{TL}	R (years)
Overturning	ULS	SF = 1.81 $>$ 1.2	0.15	310
Sliding	ULS	SF = 1.57 $>$ 1.2	0.15	310
Bearing	ULS	P_B = 484.2 $KN/m^2 < 600KN/m^2$	0.15	310
Overtopping	SLS	q $<$ 10L/s per m	0.15	310

Table 9.6: Goda safety factor for design

Component	Grading/Material	Thickness/Volume
Armour	LMA (40-200kg), Dn50=0.34m	0.60m
Under layer	CP (90/250mm), Dn50 = 0.13m	0.40m
Core	Quarry run, Dn50≈0.06m	(5.5-2m)
Ballast	Sand Fill	$315.4m^3$
Foot Block	Concrete	$7.5m^3$

Table 9.7: Layer breakdown of shallow rubble mound foundation

9.6.1. Inner Chamber Water Level Fluctuation

Given the final design geometry for the U-OWC integrated caisson, it is important to assess the maximum water level fluctuation ζ of the inner chamber. This is necessary to ensure that the turbine is kept high and dry during extreme events and based on figure 9.10 a clearance of 4.1m from DWL is available. To assess the adequacy of this clearance, the extreme event scenario has been simulated a 100 times for a duration of 30 minutes in which the max level of ζ has been stored. The results indicate a mean ζ_{max} of 3.52m with a standard deviation of 0.32m. Additionally, an exceedance probability plot (figure 9.11) has been created assuming an empirical distribution. A Gaussian distribution is also fitted and it can be seen that it matches the empirical distribution well. Based on the empirical distribution the probability of $\zeta_{max} > 4.1m$ is approximately 10% - a reasonable value considering the structure is designed for $pf_{TL} = 15\%$.

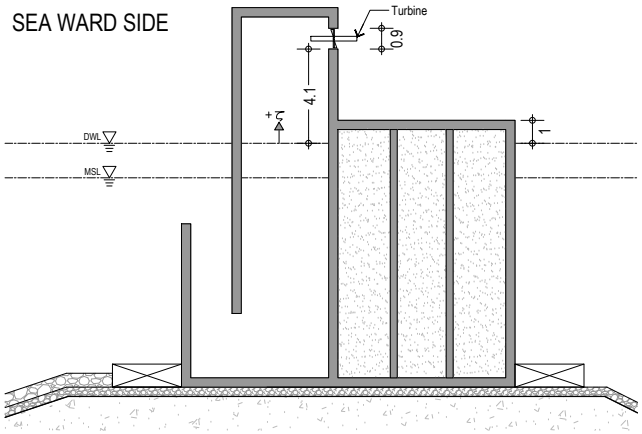

Figure 9.10: Water level fluctuation ζ clearance, dimensions in meters

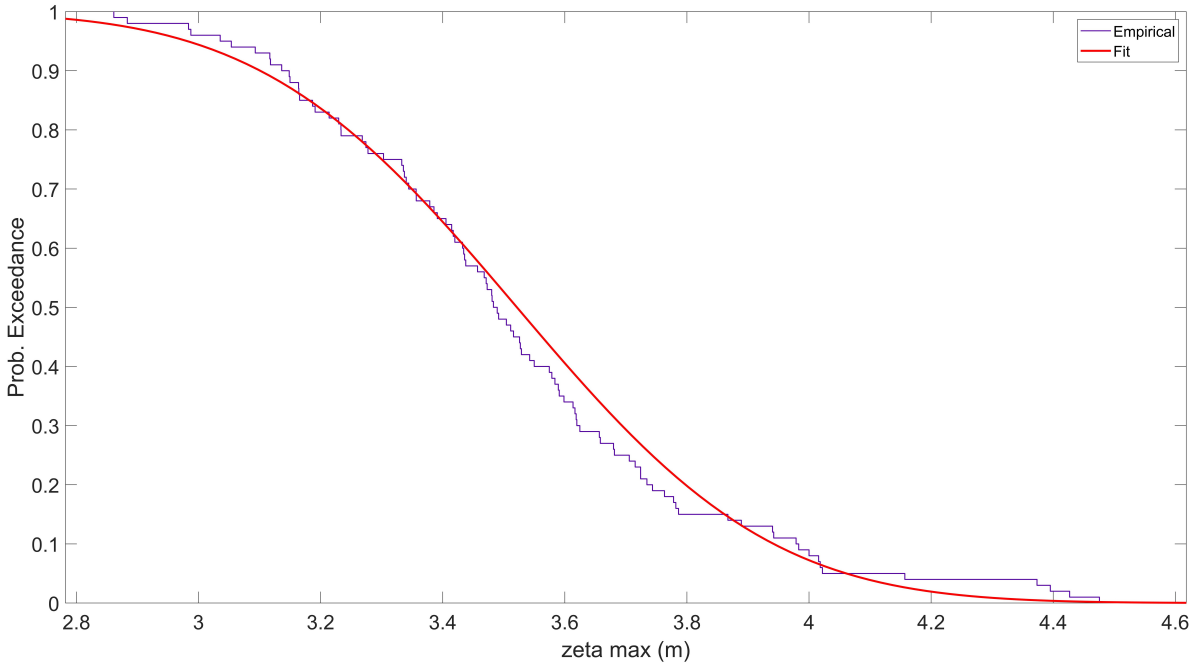

Figure 9.11: Water level fluctuation ζ exceedance probability

9.7. Final Design Layout Drawings

Displayed below are cross section drawing for the 15m and 10m depth locations - see figures 9.12 and 9.13. Additionally, images from a basic 3d model are also shown only for a short segment of the 15m depth cross section - see figures 9.14, 9.15, 9.16, 9.17, 9.18.

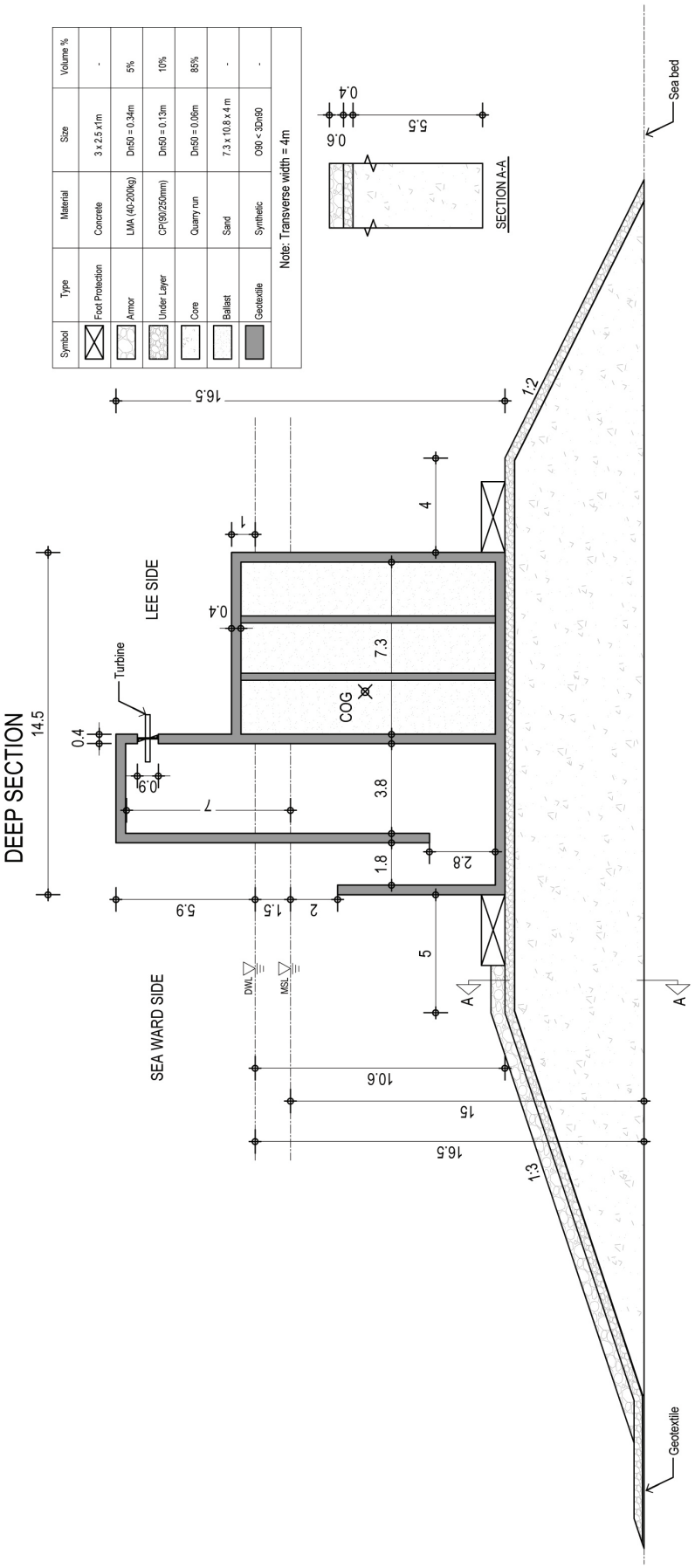

Figure 9.12: Final design cross section at 15m depth, dimensions in meters

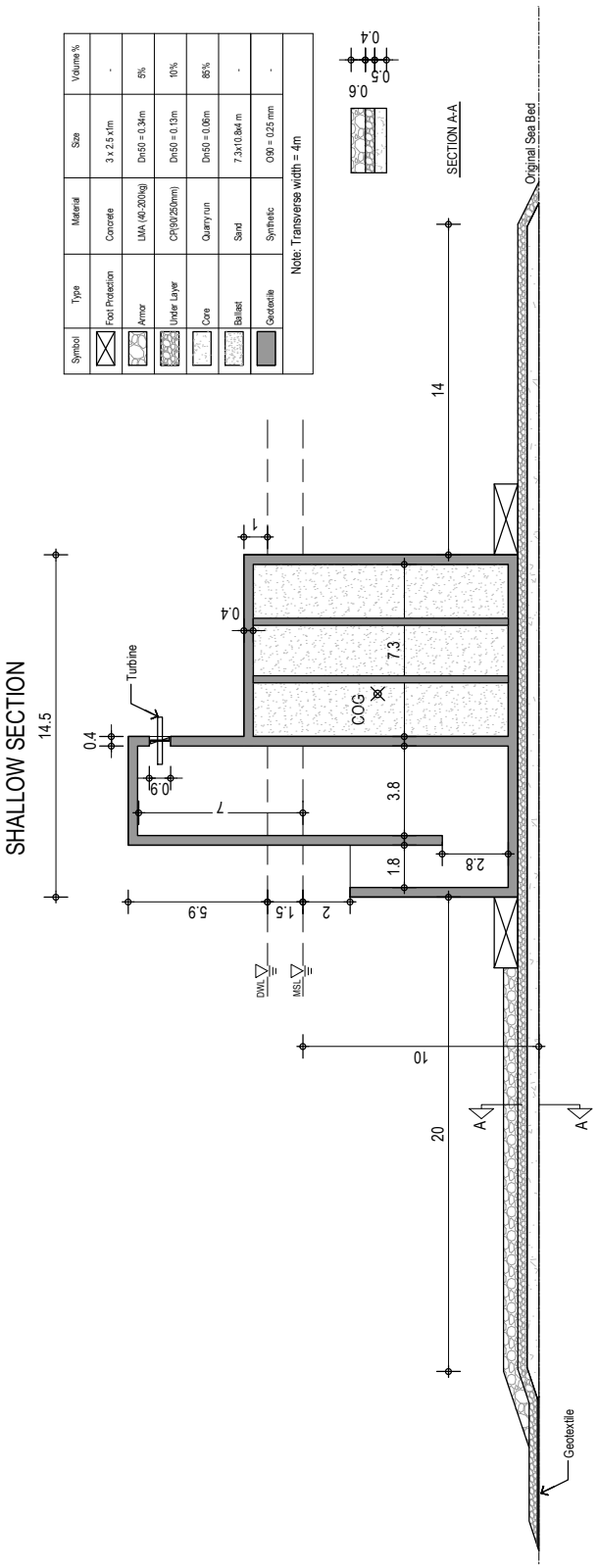

Figure 9.13: Final design cross section at 10m depth, dimensions in meters

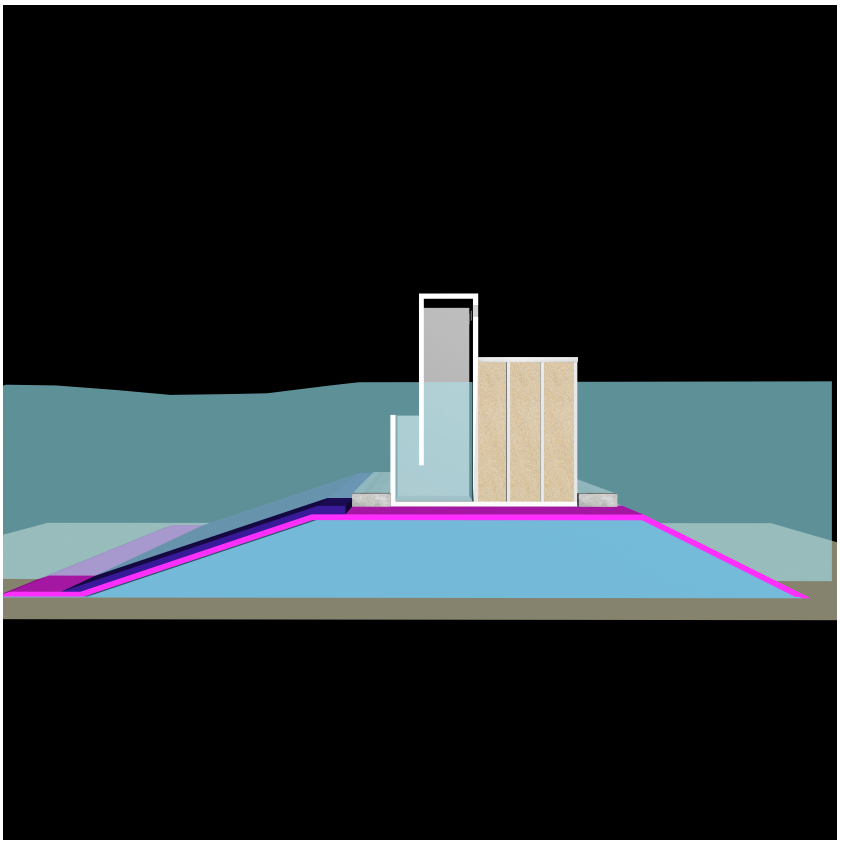

Figure 9.14: 3d model view 1

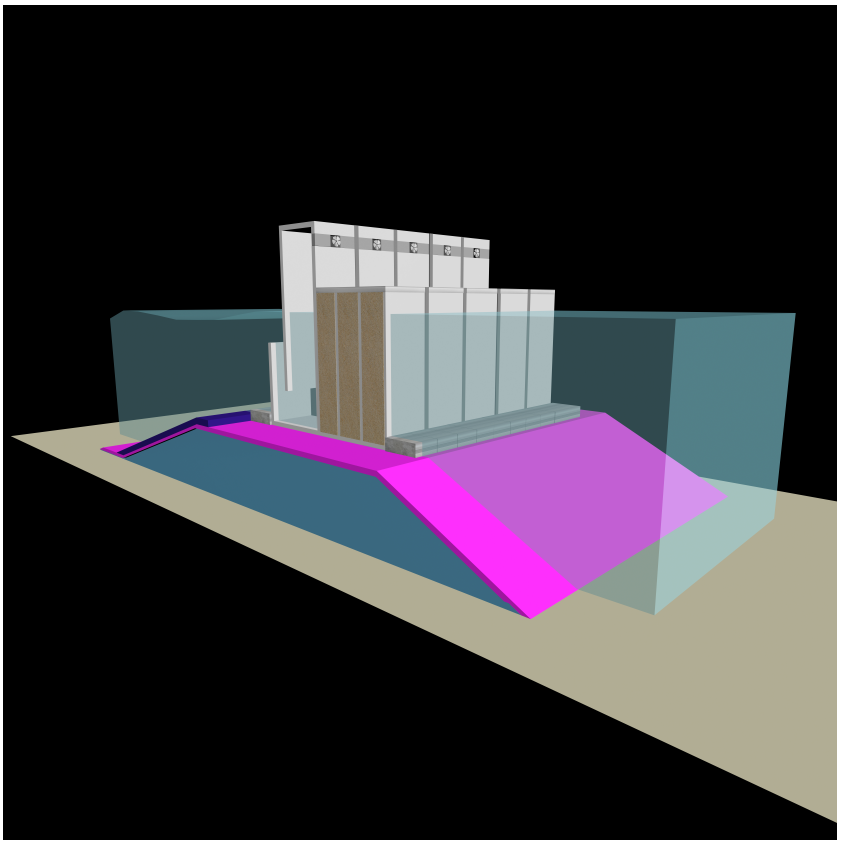

Figure 9.15: 3d model view 2

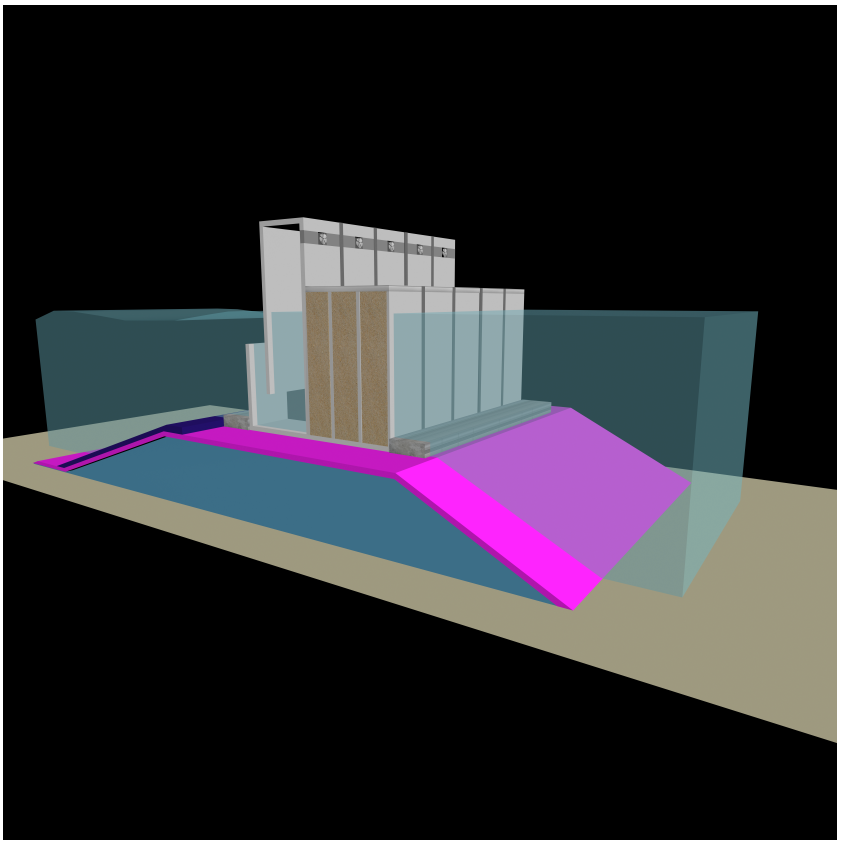

Figure 9.16: 3d model view 3

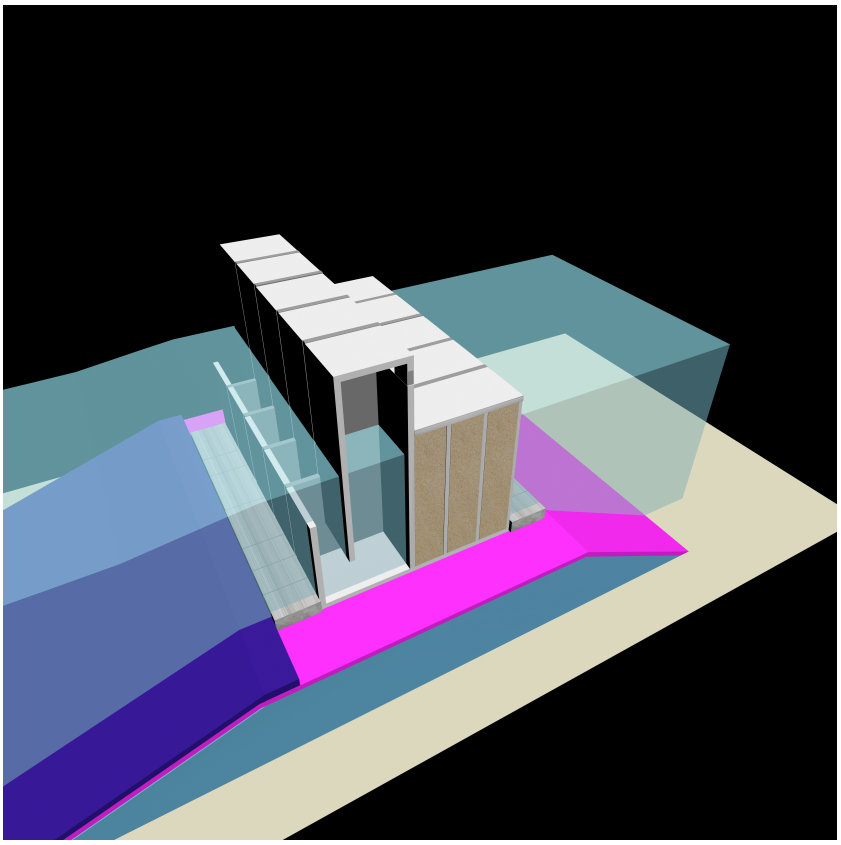

Figure 9.17: 3d model view 4

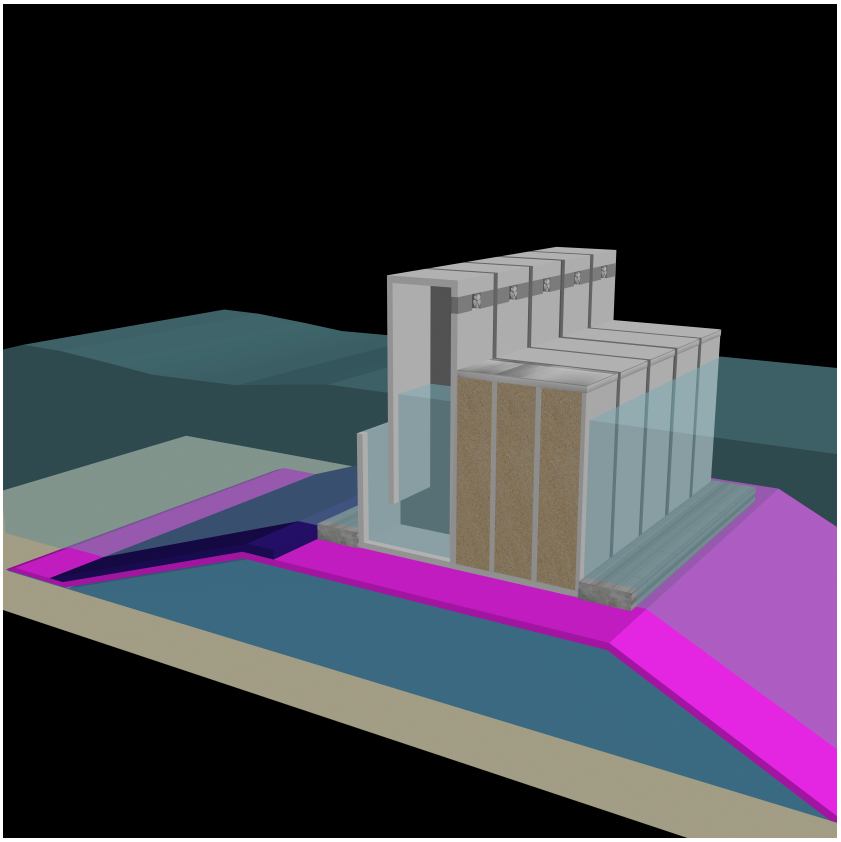

Figure 9.18: 3d model view 5

10

Economics

Discussed in this section is the approximate cost of the U-OWC integrated caisson breakwater suggested as an alternative to the rubble mound design. The costing has been done primarily on a material quantity basis and excludes the cost of engineering design fee, site investigation, and purchase of specialized equipment. To assist with this task, local consultants have agreed to provide local material rates for a previous breakwater project completed in 2011. Once a total cost estimation has been obtained, a sensitivity analysis is performed to account for the variability in caisson construction, ground improvement, and PTO cost. A cost comparison is done for the caisson breakwater versus the rubble mound, and the cross over point where one structure is cheaper than the other after a certain depth is identified. Additionally, since the U-OWC breakwater will harness wave energy, the LCOE of the device is calculated as a range based on a sensitivity analysis. Lastly, the return on investment and net present value of the structure is found. All calculations and material rates are mentioned in appendix E and costing is done for the year of 2018.

10.1. Design Cost Comparison

As mentioned by the lead consultants, the total cost for the rubble mound breakwater is around 199 million USD in the year 2018. The break-up of this cost is not available and it is valid for the entire 2.1 km alignment of breakwater option-3 (see section 5.1). However, only the 1.8km north-eastern segment is considered for re-design as a vertical caisson breakwater embedded with U-OWC chambers. Hence, to allow for an appropriate comparison, the equivalent cost only for the north-eastern segment is calculated for the rubble mound design using the material rates provided by local consultants, the calculation procedure for which is shown in appendix E. This total cost is approximately 174.4 million USD and is relatively close to the figure suggested by the lead consultants (for the entire 2.1km length) which gives confidence in the validity of the material rates used. Table 10.1 below depicts the bill of quantity and material rates for each component of the rubble mound breakwater. Here a simplifying assumption is made, that rubble mound structures are relatively less prone to geo-technical failure given that they are resilient structures and distribute their pressure on the sea bed more uniformly compared to caisson breakwaters, hence no ground improvement cost has been assumed.

Component	Unit	Rate (USD)	Quantity	Total (USD)
Armour unit	no.	1,054	59,718	69,973,579
Under layer	m^3	197	260,514	51,238,670
Core	m^3	50	926,705	45,566,808
Toe	m^3	197	70,038	13,775,283
Geotextile	m^2	50	16,200	796,566
Total Cost (USD) = 174.4 Million				

Table 10.1: Rubble mound breakwater cost for north-eastern segment, bill of quantity and material rates for the year 2018.

Typically, rubble mound breakwater are financially feasible for depths up to 8m [67], beyond which their cost increases significantly due to large material quantities required. This is made evident in table 10.1, especially for the armor units, which are $2.8m^3$ Chinese pods associated with expensive costs[1].

Considering that the depth along the north-eastern alignment varies linearly from 10-15m over a distance of 1.8 km, a vertical caisson breakwater should prove more cost effective versus a rubble mound. The integration of U-OWC chambers as designed in section 9, can allow the structure not only to shelter the vessel basin against waves but produce green energy as well. With this motive, the cost of the caisson breakwater integrated with U-OWC chambers is presented in table 10.2 below. With regard to this cost, it is important to mention the following:

Component	Unit	Rate (USD)	Quantity	Total (USD)
Armour	m^3	236	20,342	4,800,978
Under layer	m^3	236	41,348	9,758,919
Core	m^3	50	281,722	16,622,958
Geotextile	m^2	50	11,700	690,358
Caisson	no.	153,393	375	57,522,395
Foot block	no.	4,247	1,440	6,114,995
Ground improvement	m	25,000	1800	45,000,000
PTO	no.	12,500	375	4,687,500
Total Cost (USD) = 145.2 Million				

Table 10.2: U-OWC caisson breakwater cost for north-eastern segment, bill of quantity and material rates for the year 2018.

- A caisson breakwater has not yet been constructed in Pakistan, hence specialized labour and placement costs are unknown. A work of Tutuarima et al (1998) [67] is used to approximate the all in cost of a 285.8 m^3 caisson with U-OWC chamber as 153,393 USD per unit (see appendix E for details).
- Vertical breakwaters are sensitive to geo-technical issues given that they are rigid structures, and their deployment is preceded by ground improvement measures. The cost of these measures is not directly calculated given the lack of sub-soil information and to avoid significant complexities. A cost of 25,000 USD/m (equivalent to 500 USD/m^2) has been assumed along the entire 1.8km alignment. This cost has been provided based on talks with local consultants and uncertainty involved due to geo-technical aspects which might involve soil replacement and strengthening measures.
- A reference cost cannot be found for the power take off (PTO) system comprising of a wells turbine, generator, and electrical accessories on public information domains. Hence a PTO cost of 12,500 USD is assumed per caisson which might be subject to change in the future.
- The cost derived in table 10.2 is referred to as the '**base case cost**,' and incorporates the assumptions stated above. This cost will be subjected to a sensitivity analysis for the caisson, ground improvement, and PTO cost.

The results of table 10.2 indicate that the total U-OWC caisson breakwater cost is 145.2 million USD, which is cheaper compared to the rubble mound, with a saving of about 29.2 million USD. Additionally, figure 10.1 shows the cost per 4.8m section[2] of the rubble mound and U-OWC caisson breakwater plotted against depth along the north-eastern alignment. The figure shows that the cross over depth is approximately 8.7m beyond which the rubble mound sections are more expensive than the caissons - this finding agrees with general literature. However, the results of figure 10.1 are only valid for the base case cost (presented in table 10.2) of the U-OWC caisson breakwater.

[1] A cross section for the rubble mound breakwater is presented in appendix E

[2] The cost is provided per 4.8m segments because it is the transverse width of a U-OWC caisson with b3 = 4m and a wall thickness of 0.4m on either side

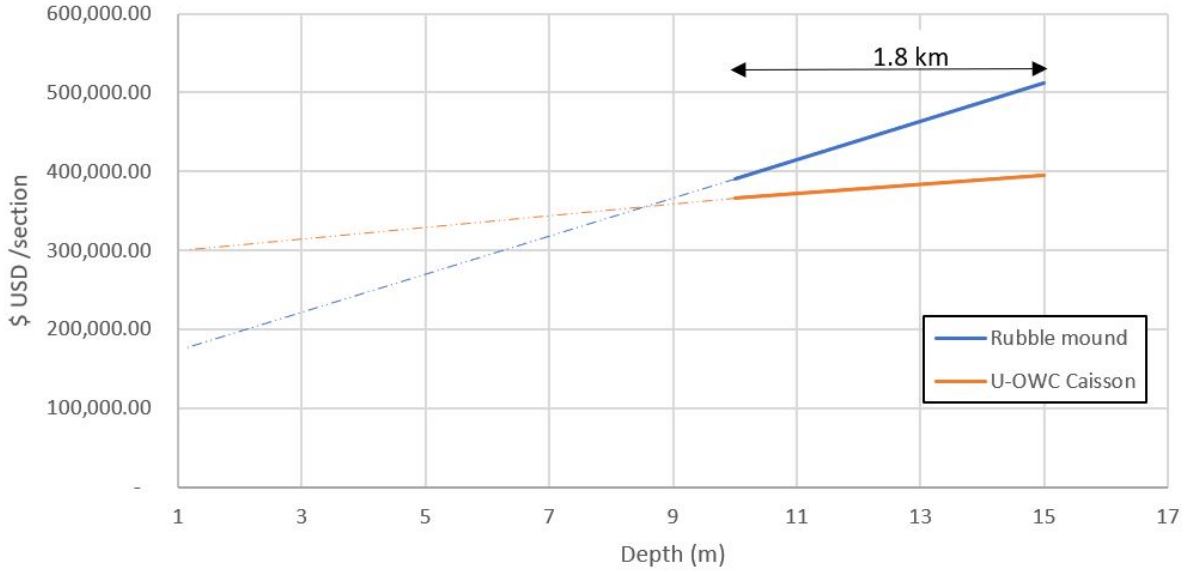

Figure 10.1: Breakwater section cost with depth, where each section is 4.8m in width.

To deal with the uncertainty in the U-OWC caisson breakwater cost, the unit rates for caisson, ground improvement, and PTO systems are increased until a cost saving of 0 is achieved - same total cost for both breakwater options. The results of this procedure are mentioned below where each parameter is increased while keeping others constant on an individual (one by one) basis.

- The max cost per caisson (285.8 m^3), inclusive of material, labour and placement, can be increased to about 231,000 USD.
- The cost of ground improvement can be increased to a maximum of 42,000 USD/m (equivalent to 840 USD/m^2) along the entire 1.8km breakwater alignment.
- The cost of the PTO system can be increase to a maximum of about 90,000 USD per caisson (chamber).

Therefore, given the results of the above, despite the uncertainty in rates for certain components, the U-OWC caisson breakwater seems to be more financially feasible compared to the rubble mound breakwater. This design not only saves cost, but can produce renewable energy as well.

10.2. Levelized Cost of Energy and Return on Investment

Based on the calculated structure cost of 145.2 million USD and annual energy production of about 6.8 GWh, the levelized cost of energy (LCOE) can be determined using equation 2.3 presented in section 2.3 .Certain assumptions have been made in the LCOE calculation and are mentioned below.

The LCOE is a function of the following variables, operation and maintenance cost (OEM), discount rate (r), and design life. To account for uncertainty in these variables, a sensitivity analysis has been performed. In this analysis the LCOE is calculated using various discount rates across a range of values for OEM cost and design life. The results of this can be seen in figure 10.2 and 10.3 where it is evident that the LCOE is highly sensitive to the discount rate and design life. Given the uncertainty involved in these parameters the LCOE is provided as a range between [1.76 - 4.49] USD/KWh, assuming a discount rate between 5-9 % and OEM cost between 1-9 % of the total cost - the design life is fixed at 50 years, decreasing it would increase the LCOE.

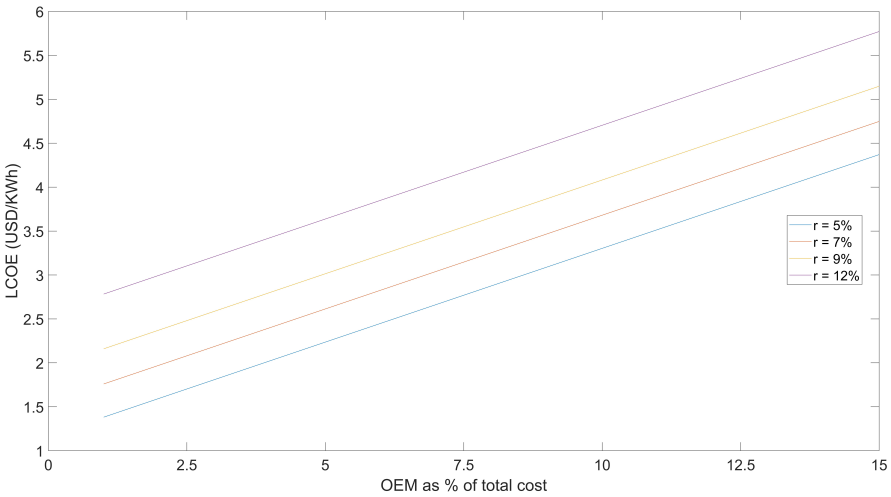

Figure 10.2: Sensitivity of LCOE for various OEM cost expressed as a % of the total cost for different discount rates - assuming fixed Design life of 50 years

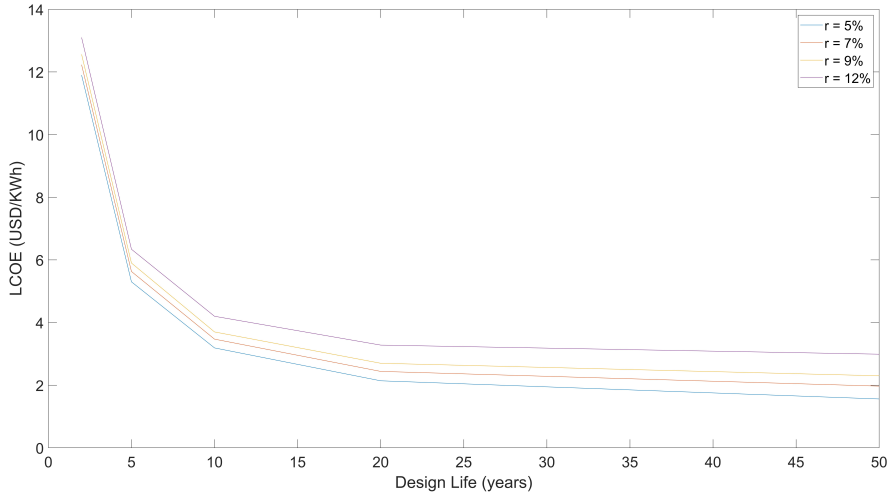

Figure 10.3: Sensitivity of LCOE on structure design life for different discount rates - assuming fixed OEM of 2%

As mentioned previously in table 2.2 (section 2.3), the typical LCOE range for initial stage WEC's is between [0.25 - 1.75]$/KWh and [0.12 - 0.47]$/KWh for mature WEC's [22]. Based on these numbers, the LCOE for the U-OWC caisson breakwater in Gwadar's low wave energy environment is not competitive in a commercial sense. Therefore, despite attempts to maximize the power conversion of the device and take advantage of the long capture width provided by the 1.8km north-eastern alignment, the disadvantage of low incident wave energy cannot be offset. Nevertheless, given that a substantial investment will be made for the creation of a breakwater in the assistance vessel basin, the U-OWC integrated caisson breakwater is cheaper than the rubble mound option and can generate renewable energy over its design life, albeit at a high cost.

Lastly, the return on investment R along with the net present value of the project is calculated using equation 10.1 and 10.2. In these equations, E represents the profits generated from selling electricity back to the utility company per year, I is the total investment cost, OEM the operational and maintenance cost per year, r is the discount rate, and N the years of device operation. The return on investment and net present value is expressed as a percentage for various electricity buy back rates the results of which are shown in table 10.3 below.

$$R = \frac{\sum_{t=1}^{N} \frac{E_t}{(1+r)^t}}{I + \sum_{t=1}^{N} \frac{OEM_t}{(1+r)^t}} \tag{10.1}$$

$$NPV_t = \sum_{t=1}^{N} \frac{(E_t - OEM_t)}{(1+r)^t} - I \tag{10.2}$$

Buy Back rate (USD/KWh)	R (%)	NPV (USD millions)
0.08	4	-173.2
0.12	6	-169.9
0.16	7	-166.5

Table 10.3: Return on Investment for various buy back rates. Buy back rates taken from [68]

In regard to the above analysis it is important to mention the following:

- The return on investment has been calculated for a discount rate of 9% (as recommended by local consultants), a design life of 50 years, and annual OEM costs of 2% of the total structure cost. The results are for the year 2022.
- The profits generated by the 6.8GWh of energy generation per year by the device greatly depend on the electricity buy back rate offered by the utility company. Unfortunately, the electricity buy back rates are not publicly available for Gwadar. Instead rates for the city of Karachi have been used as a first estimate and have been defined as a range. E_t is calculated by multiplying the annual device generation of 6.8GWh with the buy back rate and represents a yearly profit.
- The results of table 10.3 indicate a low rate of return and negative net present value across all buy back rates. This is not a surprise given the low magnitude of incident wave energy in Gwadar. However, this device is still beneficial considering that its NPV over it design life is similar to the rubble mound breakwater option, with the added advantage of renewable energy generation.
- This economic analysis presented in this report only provides first estimate values and is deemed adequate for the feasibility level. For the future, it is recommended that this analysis be developed upon further, by more accurate power estimation numbers by accounting for real time turbine performance via a control system, and more detailed costing information.

11

Conclusion

Given the world's increasing thirst for energy coupled with added pressure to de-carbonize, the findings of this thesis can help increase the global share of wave energy production by providing impetus for the potential deployment of wave energy converters in low energy environments, provided they can be integrated into proposed marine structures. This thesis availed an opportunity in Gwadar to investigate the possibility of re-designing a proposed rubble mound breakwater (option-3, see figure 5.2) with vertical caissons embedded with U-OWC chambers harnessing wave energy. The findings indicate that this option is financially more feasible compared to the rubble mound design after the 9m depth mark, giving it a lower total cost with the added advantage of renewable energy generation over its design life.

Outlined in the various sections of this thesis is a procedure undertaken to maximize the energy conversion of the U-OWC device in the low wave energy environment of Gwadar. The results indicate that despite the high cost of converting energy given the limited magnitude of the wave resource, the re-design is more sustainable as it serves the dual role of providing shelter to the assistance vessel basin and can generate clean energy.

The author of this thesis acknowledges that a series of simplifying assumptions have been made in this report, however it is worth mentioning that uncertainty in variables has been dealt with by a sensitivity analysis where appropriate and a conservative design approach has been implemented.

Considering that this is the first report to design and investigate the implementation of a wave energy converter in Pakistan, the author is hopeful that it can serve as a blueprint for future investments in marine structures to explore the possibility of integration with wave energy converters, thereby promoting sustainability in engineering design even in low wave energy environments.

11.1. Answers to Research Questions

- To determine the long term wave statistics for the region and find which sea states contain the most energy along with their frequency of occurrence?

  The results of a 10 year SWAN hindcast reveal that Gwadar experiences a summer monsoon from May through August. During these months, the Hs value ranges between 1.4 - 1.6m, and is about 0.5m in the remaining months that make up the calm season. Additionally, the average wave time period is around 6 seconds and the mean wave direction at the near shore is fairly constant throughout the year due to refraction from the Gwadar headland, the monsoon months show a slight eastward tendency in wave direction. In terms of incident power, the Gwadar wave climate has been condensed into 60 representative sea-states that have been used in the U-OWC design. Each sea-state is characterized by a value of Hs, Tp, and their joint occurrence percentage. In total, 3 KW/m of incident wave energy distributed across 60 sea-states, is available for extraction by a wave energy converter. These sea-states make up 71% of the time in a year, outside of which the wave energy is too low for energy extraction. The sea-states defined by Hs values between 0.3 - 0.5m make up the largest share of occurrence percentage.

- To determine the ideal chamber geometry and power-take-off configuration to maximize annual energy generation of the OWC device?

  The device geometry and turbine configuration has been selected to maximize the converted energy summed across all 60 design sea-states in a year. This is achieved by testing various combinations of geometric parameters sampled randomly from prescribed ranges. The parameters of combination 55 exhibit the highest converted power and have been selected for design. These parameters also resemble those of the Rocella Jonica U-OWC which is planned for deployment in a similar wave energy climate to that of Gwadar. Next, the aspect of air chamber coupling has been investigated for various turbine diameters to assess which configuration yields the highest capture width ratio. An attempt has also been made to mimic the effect of a turbine control system by identifying an ideal rotational speed for the turbine for each sea-state according to its efficiency curve. Lastly , the U-duct submergence has also been fine tuned to minimize device downtime due to joint occurrences of wave and tide conditions that can lead to uncovering of the duct. Based on the optimization, each U-OWC chamber can produce around 3KW of power accounting for array effects.
- To check if the long breakwater length providing a large capture width is enough to offset the disadvantage of low incident wave energy?

  The 1.8km north-eastern segment of breakwater option-3 is proposed as a re-design with vertical caissons integrated with 375 U-OWC chambers. Combined, these chambers can successfully convert 1.1MW of power and generate 6.8 GWh of energy based on 70.5% operational time in a year. If this structure is created it would be one of the largest in the world (see table 3.2) in terms of power production, despite being situated in a low energy environment. However it can only be feasible if a large investment is already planned for the construction of a large breakwater, as is the case for Gwadar.
- To quantify the financial cost of the vertical breakwater embedded with a U-OWC?

  Based on a simplified costing procedure the U-OWC integrated vertical caisson breakwater will cost around 145 million USD in 2018. Despite assuming conservative values for caisson, power take-off system, and ground improvement cost, this design is approximately 29 million USD cheaper than the rubble mound breakwater of option-3. Analysis also shows that the vertical caisson becomes cheaper per section after the 9m depth mark beyond which the material cost of the rubble mound breakwater increase significantly. Hence, despite the uncertainty in rates for certain components, an ample cost saving buffer remains between the vertical caisson versus rubble mound design for option-3.
- To determine the LCOE of the device and assess its financial feasibility?

  All things considered, the LCOE of the device is high and this is not a surprise considering the low wave energy environment in Gwadar. The LCOE of the device is provided as a range between [1.6 - 4.4]$/KWh given the uncertainty in variables such as the annual maintenance cost, decommissioning cost, possible design life, and interest rate. Hence, the best and worst scenario has been taken. The LCOE value for this device is inferior to that of typical wave energy converters deployed in more energetic environment (see table 2.2). Nevertheless, despite a high cost of producing energy, this device is potentially feasible considering that an investment is already planned in Gwadar for the construction of 1 out of the 3 breakwater options (see figure 5.2). The findings of this thesis have shown that re-designing the north-eastern segment of break water option-3 with vertical caissons integrated with U-OWC chambers is better and cheaper compared to the rubble mound design, with the added advantage of energy generation.

11.2. Future Recommendations

Based on the findings of this report, the research question stated at the beginning of this document have been addressed, and now it is important to expand our horizons for the future. In this regards, the following suggestions are made.

- The numerical data generated in this report has highlighted the potential for wave energy generation in Gwadar at the feasibility level. However, a realistic implementation should be evaluated using model outputs accounting for real time turbine performance.

- It has been noted that a large efficiency loss occurs at the turbine stage during power conversion. Hence further research in the design of more efficient self rectifying turbines should be undertaken, possibly turbines with variable pitch control to cater for bi-directional flow. An increase in converted power would result in a decrease in LCOE making U-OWC type devices more feasible.
- Developing countries such as Pakistan should maintain a near-shore wave model from which hindcast results are readily available for important areas along the country's coastline. In this way relatively quick assessments can be made about incident wave energy.
- All future proposed marine structures should at least investigate the feasibility of integrating a wave energy converter within them to promote a greener energy future and increase the global share of wave energy generation.
- Numerical tools for the assessment of wave energy converter design and wave models such as SWAN should be complemented with a graphical user interface to increase ease of use and popularity across various industries.

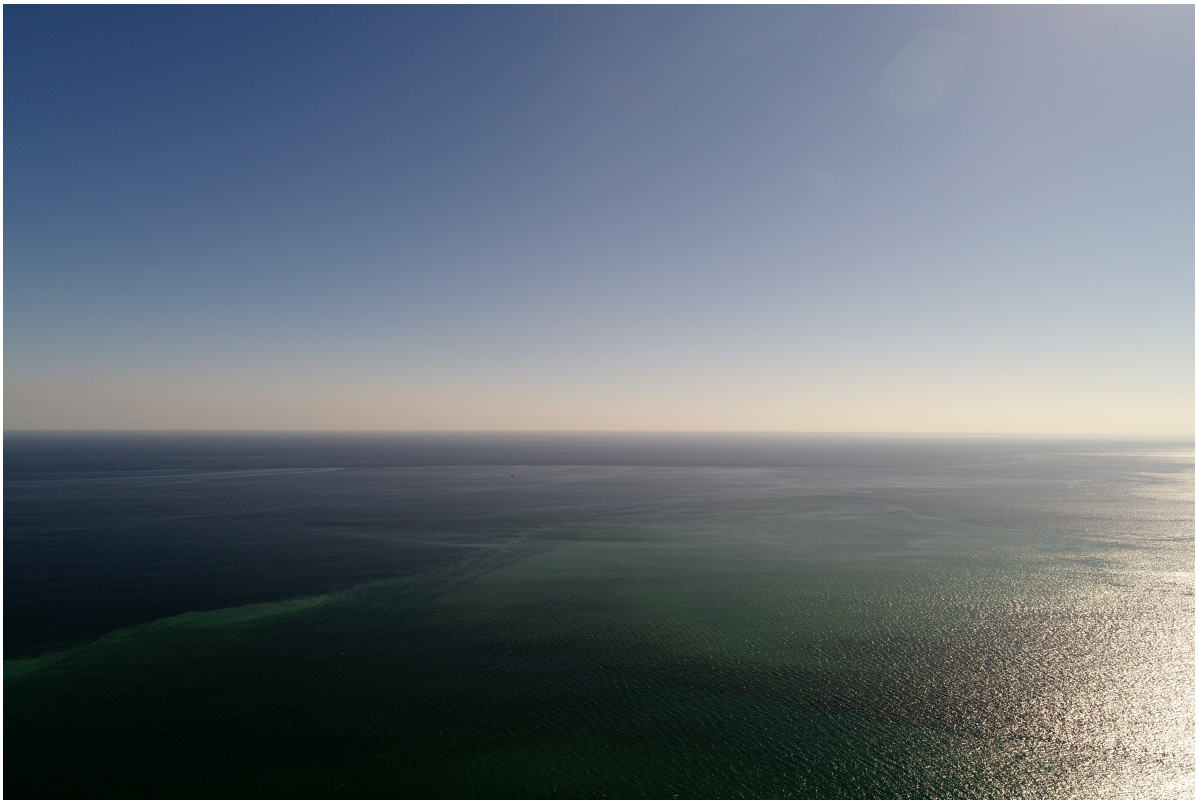

Figure 11.1: Overlooking the Gulf of Oman from the Gwadar headland, image provided by local consultants

A

Off-Shore Extreme Value Analysis

Discussed in this section is the extreme value analysis for the off-shore SWAN output point. The analysis begins by selecting a suitable threshold value by assessing the confidence interval for the σ_u and ξ parameters over a range of threshold values. Based on the dataset, a max Hs value of 3.30m is present, hence a threshold plot range between 1.5-2.8m is presented in figure A.1 below. Looking at this figure a threshold value of 2.6m has been selected, beyond this value the uncertainty begins to grow significantly.

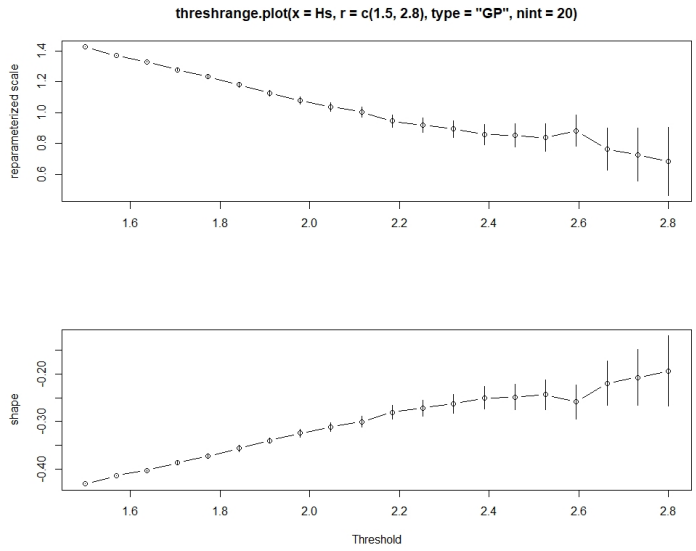

Figure A.1: Threshold sensitivity analysis for the off-shore, confidence intervals depicted as lines.

After the threshold selection, an appropriate de-cluster value needs to be determined to ensure that the captured extrema correspond to different storms and are independent in nature. For this purpose, the results of a base case with de-cluster time equal to 0 is compared to various runs where the de-cluster time is increased. Based on this table, a de-cluster time of 32 hours yields the best results as indicated by a significant increase in the EI, and major reductions in the NLL, AIC, and BIC values.

Moving forward with a threshold of $u = 2.6m$ and a de-cluster time of 32 hours, the selected extra are shown in figure A.2 as a scatter plot. Then, the GP distribution is fit to the data using a $\sigma_u = 0.338$ and $\xi = -0.428$. The results of the fitting compared against empirical data are presented in figure A.3.

Based on these results, a plot of the return period and corresponding Hs value has also been created as can be seen in figure A.4 below. The red lines indicate the 95% confidence interval calculated via bootstrapping for the associated return period. As expected, the confidence interval grows wider for larger return period values due to greater uncertainty.

de-cluster(hrs)	no. samples	EI	NLL	σ_u error	ξ error	AIC	BIC
0	1445	0.014	-1164.51	0.0066	0.0177	-2325.03	-2314.5
10	44	0.49	-26.006	0.0538	0.1243	-48.011	-44.44
24	39	0.55	-21.504	0.0611	0.130	-39.008	-35.68
32	35	0.61	-17.9	0.069	0.136	-31.84	-28.73

Table A.1: Statistical model performance for a threshold $u = 2.6m$ at the off-shore

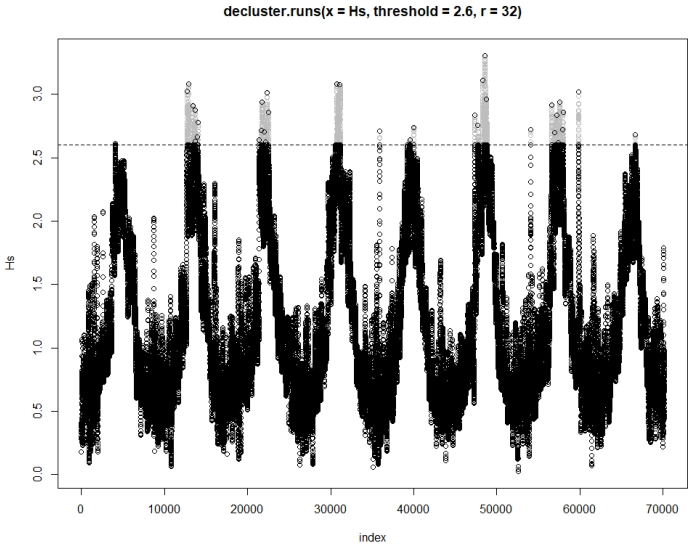

Figure A.2: Scatter plot of selected extrema at the off-shore location

For a more detailed look, table A.2 highlights the Hs values for a range of return periods including the design period of 310 years.

Return period (years)	lower bound (m)	value (m)	upper bound (m)	delta (m)
10	2.73	2.79	2.87	0.14
50	2.98	3.07	3.17	0.19
100	3.05	3.14	3.26	0.21
310	3.07	3.2	3.32	0.25

Table A.2: Return period and corresponding Hs value at the off-shore

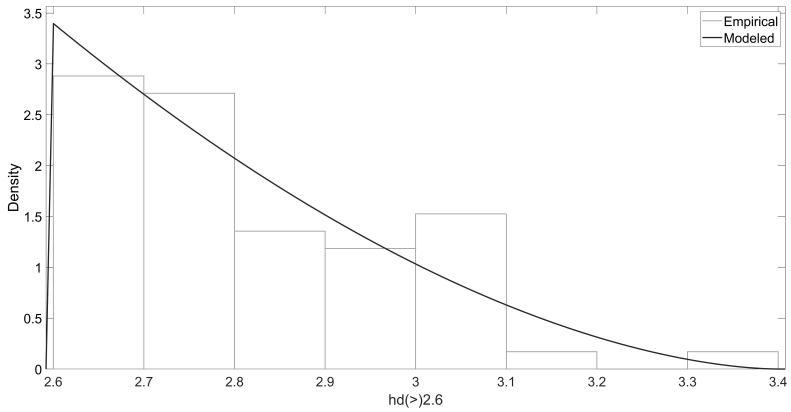

(a) Generalized Pareto distribution fit for Hs

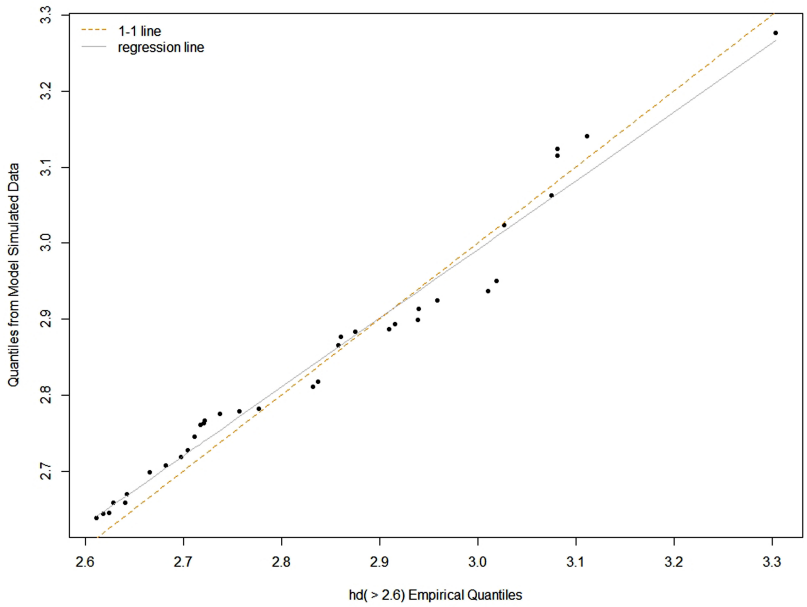

(b) Quantile comparison plot

Figure A.3: Fit of the Generalized Pareto distribution at the off-shore, Hs $>$ 2.6m

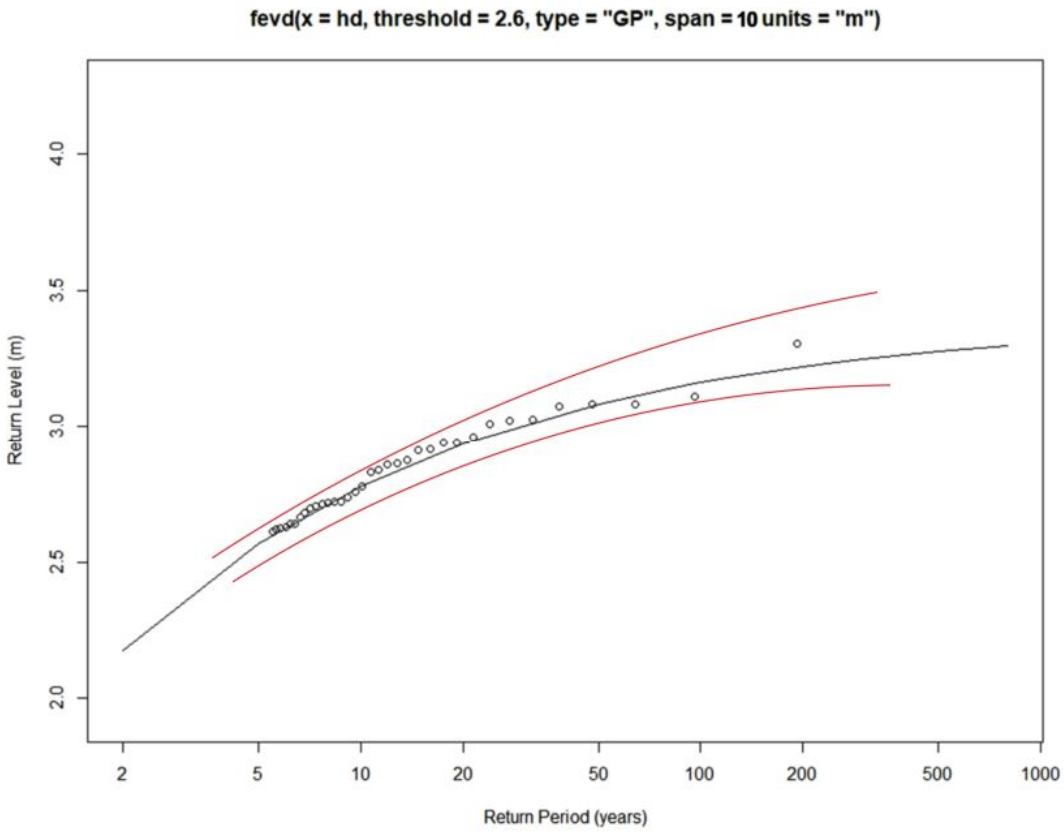

Figure A.4: Return period and corresponding Hs value for the off-shore.

B

T-Tide Results

Displayed here are the raw results as obtained from T-TIDE based on an input tidal timeseries from 07-08-2018 10:00hr to 27-05-2019 07:10hr. Tidal amplitude and phase based on 95% confidence interval.

tide	freq	amp	amp_err	pha	pha_err	snr
*M2	0.080511	0.6434	0.004	300.15	0.31	31000
*K1	0.041781	0.4074	0.004	52.81	0.58	11000
*S2	0.083333	0.2516	0.003	333.64	0.89	5200
*O1	0.038731	0.2078	0.004	49.84	1	3100
*N2	0.078999	0.1593	0.004	279.89	1.25	2100
*P1	0.041553	0.1306	0.004	47.9	1.69	1300
*K2	0.083562	0.0703	0.004	329.31	3.63	250
*SSA	0.000228	0.0537	0.02	129.48	22.63	7.2
*Q1	0.037219	0.0422	0.004	43.61	4.89	130
*NU2	0.079202	0.0316	0.004	286.88	6.55	80
*2N2	0.077487	0.0246	0.003	244.5	7.48	52
*J1	0.043293	0.0237	0.004	61.51	9.04	43
*MU2	0.07769	0.0207	0.004	247.1	9.96	31
*OO1	0.044831	0.02	0.005	95.83	11.31	19
*L2	0.082024	0.0152	0.003	320.58	13.34	24
*NO1	0.040269	0.0132	0.004	88.56	16.71	14
MSM	0.00131	0.0089	0.014	314.61	121.47	0.43
*RHO1	0.037421	0.0088	0.004	59.58	25.64	6
MM	0.001512	0.0081	0.015	154.53	130.35	0.29
*SIG1	0.035909	0.0074	0.004	43.36	25.67	3
MSF	0.002822	0.0072	0.014	4.91	158.04	0.25
*2Q1	0.035706	0.0071	0.004	38.21	32.54	4.1
*M3	0.120767	0.0068	0.002	347.34	11.14	18
*M4	0.161023	0.0068	0.001	112.46	5.08	75
*SK3	0.125114	0.0056	0.002	140.32	16.35	13
*MKS2	0.08074	0.0055	0.004	220.38	40.65	2.1
*TAU1	0.038959	0.0044	0.003	19.27	38.78	2.2
THE1	0.043091	0.0041	0.004	63.02	51.89	1.3
EPS2	0.076177	0.0041	0.003	230.83	45.32	1.8
ETA2	0.085074	0.004	0.004	341.33	60.96	1.1
MF	0.00305	0.0037	0.013	346.31	177	0.085
*MN4	0.159511	0.0033	0.001	69.65	11.77	26
SO1	0.044603	0.0032	0.003	76.25	71.84	0.95
*MO3	0.119242	0.0032	0.002	232.03	28.62	3.6
LDA2	0.081821	0.0031	0.004	338.29	67.21	0.79
OQ2	0.075975	0.003	0.003	214.14	66.06	0.85
*MS4	0.163845	0.003	0.001	199.95	15.26	19
UPS1	0.046343	0.0028	0.004	130.96	100.22	0.5
BET1	0.04004	0.0025	0.004	337.15	85.33	0.39
ALP1	0.034397	0.0023	0.004	352.76	89.88	0.39
CHI1	0.040471	0.0023	0.003	21.47	112.34	0.63
PHI1	0.042009	0.002	0.003	192.63	98.87	0.38
SO3	0.122064	0.0018	0.002	253.86	57.77	1.4
MK3	0.122292	0.0018	0.001	221.26	51.73	1.6
MSN2	0.084846	0.0015	0.003	93.21	124.27	0.29
*MK4	0.164073	0.0014	0.001	183.08	39.11	2.8
*S4	0.166667	0.0012	0.001	268.75	33.14	3.2
*2MK6	0.244584	0.0012	0	201.19	21.21	8
*2MK5	0.202804	0.001	0	275.61	30.21	5.1
*M6	0.241534	0.0009	0	190.14	21.67	5.2

Figure B.1: T-TIDE raw results for all 50 constituents

C

Raw Power Results U-OWC Device

Found below is the tabular data showing the power output, both converted and absorbed, for each of the 100 combinations from 0-99.

comb no.	b1(m)	b2(m)	h(m)	li(m)	hc(m)	Pi(KW/m)	Pa(KW/m	Pc(KW/m)
0	1.4	3.4	3.1	4.2	3.6	3.154491	1.765585	0.888364
1	1.2	4	1.5	6.4	5	3.154491	2.550041	1.119309
2	1	3	2.7	3.2	6.8	3.154491	1.686521	0.869247
3	1	3	2.3	2.2	6.4	3.154491	1.556485	0.821902
4	2	3.6	1.7	5	6	3.154491	2.386393	1.113461
5	1.2	2.2	2.1	5.4	3	3.154491	1.68719	0.859297
6	1.2	2.6	1.9	2	7.4	3.154491	1.3871	0.753404
7	1	2	2.5	6.8	4.6	3.154491	1.613548	0.824478
8	1	3.8	3.3	6	7.8	3.154491	2.307344	1.041399
9	2	2.2	1.5	2.4	6.2	3.154491	1.466508	0.790285
10	1.4	3.6	3.1	5.2	6.4	3.154491	2.017627	0.97765
11	1.6	2	2.9	7	7.8	3.154491	1.558615	0.814606
12	1.4	2	2.1	7.4	5	3.154491	1.719289	0.871076
13	1.4	3.6	2.7	3.4	6	3.154491	1.832914	0.925765
14	2	4	3.1	3.4	6.2	3.154491	1.804394	0.91841
15	1.6	4	2.5	4.8	7.6	3.154491	2.282483	1.072802
16	1.6	3.4	2.9	4	4	3.154491	1.780317	0.898485
17	1	3.4	2.3	2.8	5	3.154491	1.803523	0.911285
18	1.4	2.4	3.3	2	7.2	3.154491	1.138119	0.632946
19	1	2.8	2.9	2	6.4	3.154491	1.370461	0.740683
20	1	2.4	2.5	5.4	8	3.154491	1.759338	0.887672
21	1.2	3.6	2.7	3	7	3.154491	1.811898	0.920438
22	1.8	2	1.5	6.6	4.4	3.154491	1.894038	0.946451
23	1.6	3.6	2.7	3.6	7	3.154491	1.854171	0.93791
24	1.2	3.6	1.7	3.6	4.2	3.154491	2.087343	1.007907
25	1.6	2	1.5	5.4	5.6	3.154491	1.750526	0.899624
26	1.4	2	2.3	2	6.2	3.154491	1.132017	0.631505
27	1.4	3.2	2.1	7	3.2	3.154491	2.049129	0.975052
28	1.4	4	2.5	5.2	3	3.154491	2.05122	0.980766
29	1.2	2.4	3.1	3.8	7.6	3.154491	1.441865	0.771068
30	1	3.6	2.7	3.6	7	3.154491	1.986466	0.972693
31	1.6	2	1.5	3.8	4.2	3.154491	1.602788	0.843696
32	1.2	3.4	1.7	6	3.6	3.154491	2.173852	1.016903
33	1.4	4	2.5	5.8	6	3.154491	2.329106	1.06841
34	1.8	2.8	2.1	5.4	3.2	3.154491	1.933525	0.952308
35	1.4	2.2	2.9	2.6	5.6	3.154491	1.23805	0.680398
36	1	2.8	2.5	4.4	6.8	3.154491	1.813397	0.910066
37	1.6	2.4	2.5	3.8	7.2	3.154491	1.489214	0.795611
38	2	2.2	1.7	8	7.6	3.154491	2.071561	1.006149
39	1.6	3.8	2.7	6.4	7.6	3.154491	2.365058	1.080479
40	1.8	2.2	2.9	2.8	5.6	3.154491	1.252469	0.687753
41	1.8	2.8	2.1	4.8	7.4	3.154491	1.881577	0.950155
42	1.2	3.8	1.9	2.8	3	3.154491	1.957166	0.961346
43	1.2	2.8	2.3	4.8	7.6	3.154491	1.876349	0.937191
44	1.4	3	3.1	7.2	6.8	3.154491	1.975763	0.953575
45	2	3.2	1.9	6.4	6.4	3.154491	2.3214	1.085313
46	1.8	3.4	1.9	6.4	3.2	3.154491	2.222963	1.040025
47	1.4	2.6	1.7	3.8	6	3.154491	1.77191	0.908463
48	1.8	2.8	2.7	5.4	7.2	3.154491	1.805206	0.915531
49	1.4	2.2	3.1	4.8	3.4	3.154491	1.478973	0.779026
50	1	3.4	2.5	6.8	5	3.154491	2.054889	0.967402

51	1.2	2.6	2.1	3.6	5.8	3.154491	1.662094	0.861994
52	1	2.6	2.3	6.2	7.6	3.154491	1.949094	0.946081
53	1.6	3	1.9	2.6	5	3.154491	1.689397	0.875725
54	1.8	3.6	2.1	4.8	6.8	3.154491	2.200104	1.054334
55	1.8	3.8	1.7	6.2	7	3.154491	2.658405	1.175221
56	1.6	4	1.9	4	4	3.154491	2.186742	1.041064
57	1.6	3.2	1.5	6.4	3	3.154491	2.275158	1.054734
58	2	3.6	2.1	3.6	4.4	3.154491	1.986178	0.980615
59	2	2.6	1.7	4.6	4.8	3.154491	1.939009	0.968347
60	1.6	2.8	2.9	4	5	3.154491	1.613364	0.839034
61	2	3.6	3.1	4.4	7.4	3.154491	1.869686	0.943038
62	2	3.4	1.5	7.2	3.6	3.154491	2.52911	1.131649
63	1.2	3.4	3.1	7.6	6.2	3.154491	2.090691	0.978609
64	1	2.2	1.9	3.8	3.8	3.154491	1.597685	0.831272
65	1.4	3.2	1.7	3.2	6.4	3.154491	1.903404	0.959153
66	1.4	3.8	1.7	3.8	6.4	3.154491	2.244538	1.068859
67	1.2	3.8	3.3	3.8	7.4	3.154491	1.945278	0.959855
68	1.6	4	3.3	3.4	3	3.154491	1.760297	0.88664
69	1	2	2.7	7.4	7.2	3.154491	1.648383	0.837221
70	1.8	2.6	2.7	7	3.8	3.154491	1.816976	0.90499
71	1	3.4	2.7	5.4	7	3.154491	2.135851	1.003544
72	1.2	3.2	2.7	6.6	5.8	3.154491	2.042471	0.972649
73	1.2	2.4	2.7	3.6	6.4	3.154491	1.476577	0.785834
74	1.8	2.4	3.3	6.6	3.4	3.154491	1.620813	0.831757
75	2	3.8	2.7	3.8	3	3.154491	1.892235	0.937662
76	1.2	2	2.9	6.4	6	3.154491	1.538297	0.801303
77	1.2	2.4	2.5	5.6	7.6	3.154491	1.738996	0.88354
78	1.2	3.6	3.1	5	7.8	3.154491	2.105133	1.00332
79	1.8	3.8	3.1	5.8	4.6	3.154491	2.015243	0.975479
80	1	2	2.7	4.8	7	3.154491	1.463535	0.775942
81	2	2	3.1	3	5.4	3.154491	1.181856	0.654142
82	2	2	2.7	2.6	5.6	3.154491	1.182732	0.65567
83	1.6	2	1.7	5	6.2	3.154491	1.639307	0.85771
84	1.8	3.4	2.7	7.4	4.6	3.154491	2.097773	0.996216
85	1.4	2.6	1.5	8	5.6	3.154491	2.185723	1.022302
86	1	2.6	2.7	6.2	5.2	3.154491	1.793021	0.888936
87	2	3.8	2.1	2.4	7.4	3.154491	1.755381	0.908051
88	1.2	3.2	3.1	2.2	4	3.154491	1.506653	0.793406
89	1.8	3.6	1.5	4.6	3.2	3.154491	2.325131	1.08254
90	1.2	2.2	2.7	3.2	3.6	3.154491	1.397415	0.748734
91	1.2	2.6	1.7	5.8	3.6	3.154491	1.943821	0.948733
92	1	3.4	2.3	4.6	5.4	3.154491	2.049662	0.983787
93	2	3.2	1.7	2.4	5	3.154491	1.795972	0.918047
94	1.8	3	2.9	4.4	8	3.154491	1.717571	0.88731
95	2	3.6	2.3	6.2	7.6	3.154491	2.359952	1.095883
96	1.8	3	2.7	6.6	5.6	3.154491	1.965616	0.961361
97	1.4	3.8	3.1	6.6	7.2	3.154491	2.282572	1.046504
98	1.2	3.2	3.1	7	7.6	3.154491	2.105246	0.988787
99	1.8	2.2	2.3	7.6	8	3.154491	1.827632	0.918376

The raw power results in units of KW for the incident, absorbed, and converted power, for each sea-state have been listed in the tables below. These results are for the final U-OWC design simulated as an array with j=10 chambers. The tables list the power numbers per chamber, each with a width b3 = 4m.

ARRAY	**Pi [KW]**	b3 = 4m per chamber										
SeaState	chamber 1	chamber 2	chamber 3	chamber 4	chamber 5	chamber 6	chamber 7	chamber 8	chamber 9	chamber 10	f%	SUM x f
1	0.576853	0.576853	0.576853	0.576853	0.576853	0.576853	0.576853	0.576853	0.576853	0.576853	0.55548	0.032043
2	1.08297	1.08297	1.08297	1.08297	1.08297	1.08297	1.08297	1.08297	1.08297	1.08297	0.571448	0.061886
3	1.15337	1.15337	1.15337	1.15337	1.15337	1.15337	1.15337	1.15337	1.15337	1.15337	0.604526	0.069724
4	1.13104	1.13104	1.13104	1.13104	1.13104	1.13104	1.13104	1.13104	1.13104	1.13104	0.620495	0.07018
5	2.12222	2.12222	2.12222	2.12222	2.12222	2.12222	2.12222	2.12222	2.12222	2.12222	2.006342	0.42579
6	2.25945	2.25945	2.25945	2.25945	2.25945	2.25945	2.25945	2.25945	2.25945	2.25945	2.135231	0.482445
7	2.37547	2.37547	2.37547	2.37547	2.37547	2.37547	2.37547	2.37547	2.37547	2.37547	1.461128	0.347087
8	2.47309	2.47309	2.47309	2.47309	2.47309	2.47309	2.47309	2.47309	2.47309	2.47309	0.970663	0.240054
9	2.59619	2.59619	2.59619	2.59619	2.59619	2.59619	2.59619	2.59619	2.59619	2.59619	0.61251	0.159019
10	1.65162	1.65162	1.65162	1.65162	1.65162	1.65162	1.65162	1.65162	1.65162	1.65162	0.618213	0.102105
11	1.86945	1.86945	1.86945	1.86945	1.86945	1.86945	1.86945	1.86945	1.86945	1.86945	0.800712	0.149689
12	3.23032	3.23032	3.23032	3.23032	3.23032	3.23032	3.23032	3.23032	3.23032	3.23032	0.55662	0.179806
13	3.50884	3.50884	3.50884	3.50884	3.50884	3.50884	3.50884	3.50884	3.50884	3.50884	2.686148	0.942526
14	3.73824	3.73824	3.73824	3.73824	3.73824	3.73824	3.73824	3.73824	3.73824	3.73824	2.74546	1.026319
15	3.92889	3.92889	3.92889	3.92889	3.92889	3.92889	3.92889	3.92889	3.92889	3.92889	2.104435	0.826809
16	4.09252	4.09252	4.09252	4.09252	4.09252	4.09252	4.09252	4.09252	4.09252	4.09252	1.269505	0.519547
17	4.28681	4.28681	4.28681	4.28681	4.28681	4.28681	4.28681	4.28681	4.28681	4.28681	0.792727	0.339827
18	2.79391	2.79391	2.79391	2.79391	2.79391	2.79391	2.79391	2.79391	2.79391	2.79391	0.840633	0.234865
19	3.12553	3.12553	3.12553	3.12553	3.12553	3.12553	3.12553	3.12553	3.12553	3.12553	1.170271	0.365772
20	5.23791	5.23791	5.23791	5.23791	5.23791	5.23791	5.23791	5.23791	5.23791	5.23791	1.859202	0.973834
21	5.58487	5.58487	5.58487	5.58487	5.58487	5.58487	5.58487	5.58487	5.58487	5.58487	2.340542	1.307162
22	5.87293	5.87293	5.87293	5.87293	5.87293	5.87293	5.87293	5.87293	5.87293	5.87293	1.635642	0.960601
23	6.10847	6.10847	6.10847	6.10847	6.10847	6.10847	6.10847	6.10847	6.10847	6.10847	1.172552	0.71625
24	6.40471	6.40471	6.40471	6.40471	6.40471	6.40471	6.40471	6.40471	6.40471	6.40471	0.731134	0.46827
25	4.35492	4.35492	4.35492	4.35492	4.35492	4.35492	4.35492	4.35492	4.35492	4.35492	1.404097	0.611473
26	5.25021	5.25021	5.25021	5.25021	5.25021	5.25021	5.25021	5.25021	5.25021	5.25021	0.955835	0.501834
27	7.31294	7.31294	7.31294	7.31294	7.31294	7.31294	7.31294	7.31294	7.31294	7.31294	1.089287	0.796589
28	7.80204	7.80204	7.80204	7.80204	7.80204	7.80204	7.80204	7.80204	7.80204	7.80204	1.799891	1.404282
29	8.19505	8.19505	8.19505	8.19505	8.19505	8.19505	8.19505	8.19505	8.19505	8.19505	1.05621	0.865569
30	8.53871	8.53871	8.53871	8.53871	8.53871	8.53871	8.53871	8.53871	8.53871	8.53871	0.761931	0.650591
31	8.94277	8.94277	8.94277	8.94277	8.94277	8.94277	8.94277	8.94277	8.94277	8.94277	0.604526	0.540614
32	7.0005	7.0005	7.0005	7.0005	7.0005	7.0005	7.0005	7.0005	7.0005	7.0005	1.490784	1.043623
33	9.74468	9.74468	9.74468	9.74468	9.74468	9.74468	9.74468	9.74468	9.74468	9.74468	0.623916	0.607987
34	10.376	10.376	10.376	10.376	10.376	10.376	10.376	10.376	10.376	10.376	0.994616	1.032014
35	10.9182	10.9182	10.9182	10.9182	10.9182	10.9182	10.9182	10.9182	10.9182	10.9182	0.76079	0.830646
36	9.692	9.692	9.692	9.692	9.692	9.692	9.692	9.692	9.692	9.692	1.099553	1.065687
37	12.488	12.488	12.488	12.488	12.488	12.488	12.488	12.488	12.488	12.488	0.659275	0.823303
38	13.3456	13.3456	13.3456	13.3456	13.3456	13.3456	13.3456	13.3456	13.3456	13.3456	0.59312	0.791554
39	14.0265	14.0265	14.0265	14.0265	14.0265	14.0265	14.0265	14.0265	14.0265	14.0265	0.595401	0.835139
40	14.3953	14.3953	14.3953	14.3953	14.3953	14.3953	14.3953	14.3953	14.3953	14.3953	0.59426	0.855456
41	15.6316	15.6316	15.6316	15.6316	15.6316	15.6316	15.6316	15.6316	15.6316	15.6316	1.106397	1.729475
42	16.6467	16.6467	16.6467	16.6467	16.6467	16.6467	16.6467	16.6467	16.6467	16.6467	0.617073	1.027222
43	19.0903	19.0903	19.0903	19.0903	19.0903	19.0903	19.0903	19.0903	19.0903	19.0903	1.123506	2.144806
44	20.3437	20.3437	20.3437	20.3437	20.3437	20.3437	20.3437	20.3437	20.3437	20.3437	0.85318	1.735684
45	22.8743	22.8743	22.8743	22.8743	22.8743	22.8743	22.8743	22.8743	22.8743	22.8743	1.189661	2.721267
46	24.3807	24.3807	24.3807	24.3807	24.3807	24.3807	24.3807	24.3807	24.3807	24.3807	1.723469	4.201939
47	27.0662	27.0662	27.0662	27.0662	27.0662	27.0662	27.0662	27.0662	27.0662	27.0662	1.055069	2.855671
48	28.821	28.821	28.821	28.821	28.821	28.821	28.821	28.821	28.821	28.821	2.078201	5.989582
49	31.5662	31.5662	31.5662	31.5662	31.5662	31.5662	31.5662	31.5662	31.5662	31.5662	0.787024	2.484337
50	33.6374	33.6374	33.6374	33.6374	33.6374	33.6374	33.6374	33.6374	33.6374	33.6374	2.126106	7.151669
51	35.3502	35.3502	35.3502	35.3502	35.3502	35.3502	35.3502	35.3502	35.3502	35.3502	0.885117	3.128907
52	36.4322	36.4322	36.4322	36.4322	36.4322	36.4322	36.4322	36.4322	36.4322	36.4322	0.714025	2.60135
53	38.7914	38.7914	38.7914	38.7914	38.7914	38.7914	38.7914	38.7914	38.7914	38.7914	2.063373	8.004111
54	40.813	40.813	40.813	40.813	40.813	40.813	40.813	40.813	40.813	40.813	1.31741	5.376747
55	44.2972	44.2972	44.2972	44.2972	44.2972	44.2972	44.2972	44.2972	44.2972	44.2972	1.759969	7.79617
56	46.5964	46.5964	46.5964	46.5964	46.5964	46.5964	46.5964	46.5964	46.5964	46.5964	1.454284	6.776441
57	50.2037	50.2037	50.2037	50.2037	50.2037	50.2037	50.2037	50.2037	50.2037	50.2037	0.998038	5.010521
58	52.8122	52.8122	52.8122	52.8122	52.8122	52.8122	52.8122	52.8122	52.8122	52.8122	1.588877	8.391208
59	59.4974	59.4974	59.4974	59.4974	59.4974	59.4974	59.4974	59.4974	59.4974	59.4974	1.071038	6.372395
60	66.4396	66.4396	66.4396	66.4396	66.4396	66.4396	66.4396	66.4396	66.4396	66.4396	0.662697	4.402935
											Sum	**114.1604**

ARRAY	**Pa [KW]**	b3 = 4m per chamber										
SeaState	chamber 1	chamber 2	chamber 3	chamber 4	chamber 5	chamber 6	chamber 7	chamber 8	chamber 9	chamber 10	f%	SUM x f
1	0.076357	0.0682587	0.0655795	0.0657391	0.0734278	0.075316	0.070111	0.0706091	0.0727136	0.0794178	0.55548	0.003986
2	0.763215	0.685885	0.636635	0.607572	0.583957	0.582313	0.596922	0.614594	0.657121	0.728276	0.571448	0.036895
3	0.802487	0.762118	0.744583	0.743281	0.719724	0.721229	0.754657	0.775114	0.812477	0.872087	0.604526	0.046595
4	0.144478	0.127528	0.120222	0.11731	0.127031	0.128974	0.121458	0.126945	0.136639	0.155695	0.620495	0.008105
5	1.39616	1.27427	1.19686	1.15249	1.12573	1.13166	1.1619	1.19189	1.25717	1.36954	2.006342	0.245931
6	1.50241	1.40024	1.33575	1.29465	1.24191	1.22649	1.25567	1.27696	1.32771	1.41753	2.135231	0.283544
7	1.60982	1.54687	1.50845	1.49203	1.43355	1.43162	1.48276	1.48911	1.51654	1.57037	1.461128	0.220354
8	1.45946	1.42481	1.40909	1.41108	1.37649	1.3967	1.47051	1.49457	1.53078	1.58258	0.970663	0.14129
9	1.30036	1.28397	1.28222	1.29696	1.26078	1.27887	1.35113	1.3727	1.40146	1.43645	0.61251	0.081249
10	0.30032	0.270885	0.264314	0.266512	0.284599	0.285666	0.269248	0.26883	0.277268	0.303986	0.618213	0.017258
11	0.424266	0.376019	0.356467	0.350663	0.379742	0.380315	0.35291	0.362403	0.386699	0.439408	0.800712	0.030498
12	1.79019	1.60756	1.49149	1.42204	1.40636	1.39563	1.39293	1.45201	1.56634	1.75178	0.55662	0.085031
13	2.01185	1.85444	1.76438	1.72239	1.6989	1.69656	1.72481	1.77699	1.87414	2.03192	2.686148	0.487707
14	2.61368	2.50217	2.4442	2.43004	2.37394	2.39102	2.48447	2.5412	2.63605	2.77825	2.74546	0.691719
15	2.27031	2.15877	2.08817	2.044	1.96286	1.95052	1.99887	2.02052	2.07794	2.1635	2.104435	0.436364
16	2.20603	2.17468	2.17147	2.19985	2.13046	2.13861	2.24125	2.25061	2.28722	2.335	1.269505	0.281007
17	2.18643	2.17095	2.17207	2.18723	2.11136	2.11719	2.2164	2.23537	2.26304	2.29796	0.792727	0.174067
18	0.634347	0.573686	0.550621	0.544688	0.593117	0.596604	0.554	0.561578	0.585952	0.648221	0.840633	0.049117
19	0.83026	0.731814	0.687286	0.669959	0.730938	0.729183	0.669515	0.689374	0.73542	0.832434	1.170271	0.085502
20	3.5416	3.27247	3.09532	2.98545	2.89922	2.87289	2.90702	2.97113	3.09457	3.30813	1.859202	0.575382
21	3.46373	3.30947	3.22136	3.18501	3.10352	3.09596	3.1808	3.24752	3.36204	3.5361	2.340542	0.765486
22	3.45117	3.33835	3.27196	3.25441	3.17457	3.18487	3.27238	3.28519	3.32925	3.41246	1.635642	0.539347
23	3.51483	3.41692	3.3474	3.30569	3.18966	3.17506	3.22203	3.23982	3.29055	3.41292	1.172552	0.388289
24	3.18027	3.17807	3.18926	3.21256	3.12212	3.13883	3.26703	3.28667	3.31405	3.34684	0.731134	0.235686
25	1.52448	1.31665	1.2094	1.1604	1.23084	1.23048	1.16636	1.23127	1.35296	1.5764	1.404097	0.182522
26	2.4874	2.17246	1.99551	1.90218	1.97199	1.93602	1.82221	1.90882	2.06826	2.3461	0.955835	0.197007
27	4.39675	4.116	3.94769	3.85726	3.76683	3.746	3.79082	3.8586	4.02059	4.26468	1.089287	0.433158
28	4.26553	4.06091	3.93406	3.86911	3.77544	3.78052	3.86847	3.92503	4.02011	4.21982	1.799891	0.714899
29	4.33264	4.18187	4.08874	4.04454	3.94688	3.94871	4.05512	4.10376	4.20376	4.36668	1.05621	0.435926
30	4.50824	4.39089	4.30751	4.25413	4.11032	4.07902	4.17062	4.14939	4.17664	4.2473	0.761931	0.323013
31	4.7327	4.64575	4.57349	4.51757	4.33674	4.2992	4.39088	4.34376	4.31642	4.31084	0.604526	0.268817
32	3.46958	3.02007	2.75122	2.59996	2.69395	2.74782	2.7224	2.8871	3.17815	3.62889	1.490784	0.44275
33	5.24474	4.96543	4.79963	4.72344	4.64797	4.67047	4.7742	4.9135	5.14451	5.49341	0.623916	0.308073
34	5.89426	5.63605	5.45591	5.31896	5.15783	5.09843	5.16857	5.21263	5.34198	5.56917	0.994616	0.535639
35	5.71494	5.5564	5.46255	5.41783	5.26039	5.22722	5.34395	5.37761	5.4842	5.6283	0.76079	0.414428
36	5.08388	4.49145	4.11657	3.87717	3.88355	3.85987	3.80075	3.97865	4.32187	4.88515	1.099553	0.465099
37	6.5253	6.15078	5.91792	5.80009	5.67108	5.63598	5.73394	5.87329	6.11647	6.48176	0.659275	0.39495
38	6.65366	6.33949	6.11629	5.97403	5.7951	5.76294	5.86091	5.95462	6.14784	6.46127	0.59312	0.362195
39	6.68777	6.50624	6.40081	6.36465	6.22481	6.23002	6.41407	6.53932	6.72878	6.98827	0.595401	0.387515
40	7.41749	6.88898	6.55645	6.38741	6.34034	6.36496	6.47793	6.74475	7.1389	7.74036	0.59426	0.404439
41	8.65247	8.22445	7.93591	7.76632	7.63628	7.66558	7.78541	7.88324	8.09192	8.4358	1.106397	0.885973
42	7.58808	7.23844	7.00995	6.89339	6.76642	6.81102	7.03441	7.21371	7.49549	7.91525	0.617073	0.444084
43	9.14176	8.64777	8.3453	8.21518	8.158	8.24315	8.48987	8.81672	9.25908	9.87423	1.123506	0.979597
44	9.41677	9.16787	9.04326	9.02822	8.91794	9.00493	9.30995	9.56413	9.91813	10.3823	0.85318	0.799886
45	11.439	10.8769	10.5106	10.2929	10.063	9.9651	10.1233	10.3168	10.6617	11.1856	1.189661	1.254318
46	11.878	11.5405	11.3347	11.253	11.0892	11.1765	11.5121	11.7569	12.1049	12.5095	1.723469	2.001901
47	11.8931	11.3192	10.9557	10.7837	10.6886	10.8565	11.2189	11.5527	11.9824	12.6195	1.055069	1.20141
48	12.2891	11.8948	11.6334	11.4863	11.2063	11.132	11.3208	11.4969	11.8196	12.3051	2.078201	2.422856
49	13.5632	12.9387	12.5475	12.4331	12.2623	12.304	12.5756	12.7392	13.0912	13.6669	0.787024	1.008349
50	15.7853	15.3427	14.9459	14.6588	14.3714	14.3776	14.7245	14.9217	15.3027	15.7264	2.126106	3.192498
51	15.7778	15.3799	15.1114	14.9147	14.5786	14.5857	14.834	14.8899	15.0299	15.3377	0.885117	1.331567
52	16.5916	15.9079	15.4848	15.1881	14.9536	14.9572	15.1849	15.4365	15.8198	16.4814	0.714025	1.11392
53	16.5711	15.9345	15.4109	15.0578	14.5888	14.397	14.5108	14.6272	14.8656	15.2639	2.063373	3.120389
54	16.5556	16.0615	15.7251	15.5929	15.2003	15.1429	15.4589	15.683	16.0964	16.5825	1.31741	2.082814
55	17.6108	17.0663	16.6662	16.3044	15.8283	15.7403	16.0701	16.3809	16.867	17.4126	1.759969	2.920614
56	16.0501	15.6892	15.5218	15.5442	15.4152	15.5055	15.8821	16.1848	16.6447	17.302	1.454284	2.323068
57	19.5699	19.0508	18.681	18.4621	18.1573	18.0139	18.1852	18.4128	18.9543	19.5962	0.998038	1.867165
58	18.1533	17.578	17.1593	17.0191	16.753	16.6988	17.0066	17.225	17.6101	18.2159	1.588877	2.755416
59	19.7163	19.0703	18.5744	18.2017	17.708	17.6791	18.1008	18.2197	18.7118	19.2444	1.071038	1.983845
60	22.14	21.5112	21.1574	20.8835	20.5815	20.5311	20.9966	21.4964	21.8929	22.5903	0.662697	1.41672
											Sum	**47.28723**

ARRAY	**Pc [KW]**	b3 = 4m per chamber										
SeaState	chamber 1	chamber 2	chamber 3	chamber 4	chamber 5	chamber 6	chamber 7	chamber 8	chamber 9	chamber 10	f%	SUM x f
1	0.051513	0.0462358	0.044499	0.0446667	0.0500333	0.0518457	0.0486213	0.0499213	0.0529353	0.0594019	0.55548	0.002776
2	0.492897	0.434401	0.396319	0.374283	0.351896	0.346558	0.356066	0.357202	0.37598	0.412882	0.571448	0.022278
3	0.511184	0.490352	0.479588	0.476236	0.450184	0.450263	0.474413	0.475195	0.484355	0.502959	0.604526	0.028985
4	0.088718	0.0804473	0.0781521	0.0790143	0.0872825	0.0887889	0.0822253	0.0813662	0.0824241	0.0884746	0.620495	0.005193
5	0.972833	0.903953	0.864821	0.847925	0.81795	0.812962	0.839986	0.855091	0.88906	0.953373	2.006342	0.175714
6	1.00595	0.952364	0.920932	0.905299	0.86856	0.87469	0.91442	0.914524	0.928133	0.9593	2.135231	0.197384
7	0.906913	0.895612	0.895907	0.903804	0.871748	0.877711	0.92479	0.930068	0.946247	0.971974	1.461128	0.133325
8	0.861467	0.84908	0.842168	0.840904	0.799883	0.797928	0.837778	0.83424	0.835361	0.840696	0.970663	0.080949
9	0.794851	0.797757	0.802229	0.808352	0.772286	0.772663	0.813026	0.816605	0.815008	0.818376	0.61251	0.049069
10	0.21333	0.194898	0.192075	0.195567	0.211298	0.209728	0.19285	0.190664	0.197092	0.219598	0.618213	0.01247
11	0.308584	0.2683	0.248951	0.24037	0.259087	0.254311	0.233158	0.241807	0.263425	0.308759	0.800712	0.021033
12	1.25178	1.10173	1.00863	0.960083	0.950094	0.963291	0.997019	1.05754	1.1522	1.29447	0.55662	0.059763
13	1.36567	1.25905	1.1887	1.14815	1.09828	1.08064	1.10431	1.1323	1.19027	1.28646	2.686148	0.318411
14	1.49654	1.42924	1.38369	1.35712	1.30199	1.29557	1.34952	1.35171	1.37694	1.41942	2.74546	0.377823
15	1.48282	1.462	1.45315	1.45409	1.38951	1.37336	1.41868	1.42072	1.43563	1.46593	2.104435	0.30211
16	1.44861	1.4492	1.4497	1.45036	1.38608	1.37953	1.42491	1.40676	1.39233	1.38288	1.269505	0.179893
17	1.17614	1.17693	1.18452	1.19106	1.14438	1.14271	1.19231	1.19386	1.19673	1.20094	0.792727	0.093539
18	0.404238	0.356599	0.341793	0.343545	0.378044	0.383171	0.355114	0.356436	0.372024	0.418722	0.840633	0.031185
19	0.614256	0.535107	0.490101	0.465157	0.500173	0.501602	0.466148	0.486707	0.528878	0.608238	1.170271	0.060812
20	1.96963	1.87144	1.81639	1.79942	1.76205	1.78433	1.86567	1.93093	2.03559	2.18743	1.859202	0.353674
21	2.41207	2.32005	2.25385	2.20033	2.10025	2.06852	2.11162	2.1152	2.15003	2.21699	2.340542	0.513723
22	1.99096	1.91392	1.85849	1.81712	1.71829	1.69061	1.73008	1.73365	1.7543	1.80207	1.635642	0.294571
23	1.99166	1.97411	1.96237	1.95768	1.88191	1.87564	1.94245	1.93867	1.94101	1.94844	1.172552	0.227639
24	1.44052	1.43175	1.43343	1.44021	1.39685	1.40537	1.46831	1.48132	1.50356	1.5244	0.731134	0.106203
25	1.03378	0.865955	0.778039	0.73751	0.792314	0.796803	0.749122	0.792678	0.876783	1.03145	1.404097	0.118708
26	1.56895	1.33606	1.19284	1.11538	1.15606	1.14464	1.09392	1.17733	1.31841	1.53811	0.955835	0.120834
27	2.50329	2.34205	2.21984	2.17881	2.13312	2.15538	2.24502	2.32233	2.44789	2.62882	1.089287	0.252459
28	2.85629	2.7727	2.72428	2.70825	2.63905	2.64822	2.73397	2.75948	2.81301	2.89929	1.799891	0.495952
29	2.81027	2.72447	2.66942	2.63444	2.53299	2.52427	2.60126	2.6072	2.63954	2.6995	1.05621	0.279297
30	3.13238	3.12552	3.1169	3.13676	3.02555	3.01645	3.09642	3.06072	3.02903	3.00048	0.761931	0.234219
31	2.60375	2.57782	2.54983	2.52404	2.41123	2.38394	2.43523	2.40036	2.3617	2.32599	0.604526	0.148556
32	2.49939	2.17934	1.95926	1.81211	1.80462	1.71178	1.5883	1.64363	1.78366	2.04541	1.490784	0.283659
33	3.34297	3.23582	3.18796	3.19513	3.15282	3.19558	3.35043	3.5492	3.75198	4.00748	0.623916	0.21194
34	3.87854	3.75959	3.6686	3.60932	3.45956	3.40976	3.47781	3.48817	3.51551	3.58983	0.994616	0.356636
35	3.22801	3.17497	3.15106	3.16361	3.09398	3.13033	3.25585	3.27621	3.30993	3.35211	0.76079	0.244488
36	3.26378	2.89565	2.65757	2.51274	2.53673	2.52603	2.47335	2.57493	2.75275	3.04766	1.099553	0.299531
37	3.76023	3.61257	3.53988	3.53242	3.49834	3.56106	3.72359	3.85875	4.05407	4.31521	0.659275	0.246939
38	4.25556	4.10299	4.01462	3.96758	3.85786	3.86869	4.0056	4.072	4.16759	4.328	0.59312	0.241047
39	4.08851	4.01937	3.96157	3.94255	3.84226	3.86252	3.99452	4.02667	4.08115	4.15903	0.595401	0.23803
40	5.08145	4.67803	4.42151	4.2524	4.1381	4.13845	4.25915	4.43853	4.72898	5.13062	0.59426	0.269005
41	5.15175	4.96554	4.86351	4.82757	4.74149	4.74759	4.87376	4.9836	5.15169	5.38295	1.106397	0.549762
42	4.75657	4.60299	4.5091	4.48255	4.40471	4.46784	4.66173	4.76886	4.92201	5.11909	0.617073	0.288145
43	5.73647	5.59651	5.54478	5.5715	5.53422	5.62272	5.84363	6.02278	6.26865	6.61147	1.123506	0.655596
44	6.3576	6.26939	6.23854	6.2622	6.17981	6.24487	6.46309	6.58101	6.73155	6.91424	0.85318	0.548102
45	7.12615	6.82962	6.62465	6.49565	6.30622	6.28799	6.45358	6.51834	6.69465	6.93599	1.189661	0.788422
46	7.1258	6.93728	6.81193	6.72182	6.51786	6.50146	6.66798	6.70362	6.79836	6.94964	1.723469	1.167405
47	8.06435	7.78543	7.63902	7.58769	7.4729	7.54931	7.7783	7.91155	8.12128	8.41678	1.055069	0.8264
48	8.00448	7.91533	7.88688	7.91963	7.82916	7.93625	8.22684	8.32632	8.48487	8.70849	2.078201	1.688294
49	8.52009	8.10754	7.80194	7.59031	7.35241	7.29941	7.416	7.48687	7.67468	7.98578	0.787024	0.607859
50	9.05853	8.95491	8.85231	8.79479	8.57473	8.56104	8.73113	8.74157	8.71886	8.83508	2.126106	1.867209
51	9.65318	9.47094	9.32392	9.22004	8.93511	8.88448	9.0507	9.0406	9.08253	9.1776	0.885117	0.812884
52	9.82058	9.57822	9.46074	9.53415	9.38753	9.41968	9.67027	9.86501	10.1152	10.4721	0.714025	0.694914
53	9.7533	9.58307	9.57036	9.64339	9.55827	9.66879	10.0116	10.2488	10.5337	10.8564	2.063373	2.051563
54	9.79835	9.70542	9.67899	9.68326	9.59874	9.69893	10.0333	10.1684	10.2823	10.4199	1.31741	1.305127
55	10.5425	10.4214	10.2304	10.1226	9.93331	9.95082	10.2315	10.3522	10.4972	10.7648	1.759969	1.81359
56	10.6218	10.4091	10.2175	10.2007	10.0242	10.0392	10.3559	10.467	10.5909	10.8547	1.454284	1.509271
57	11.0844	10.9598	10.8839	10.9214	10.8062	10.9481	11.2302	11.3317	11.4885	11.7352	0.998038	1.111709
58	11.4775	11.1129	10.777	10.4016	10.0198	9.78119	9.88639	9.83104	9.87568	9.95654	1.588877	1.638444
59	11.951	11.7711	11.7611	11.7194	11.4694	11.4774	11.7346	11.828	11.9178	12.0817	1.071038	1.260734
60	14.196	13.8598	13.6259	13.6121	13.383	13.4787	13.6999	13.6832	13.6479	13.6795	0.662697	0.907007
											Sum	**29.78226**

D

Design Calculations

Discussed in this appendix are the design calculations for the Goda method. **All equations and figures have been taken from Takahashi (2002) [63] unless mentioned otherwise**. The geometric parameters required have been depicted in the figure below and their corresponding values (selected for design) are shown in the following table.

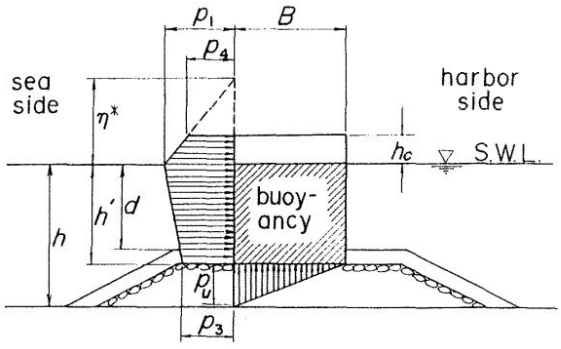

Goda geometric design parameters, Takahashi (2002)

R (years)	310
Pf,TL	0.15
h (at DWL) (m)	16.5
BM (m)	5
hc (m)	5.8
h' (m)	10.6
d (m)	9.6
theta (rad)	0
hb (m)	16.53
slope	1/360
caisson length (m)	14.5
DWL to crest (m)	5.8
DWL to caisson bottom (m)	10.6

Selected values for various parameters

The application of the Goda method is iterative in nature, as a selection of geometric parameters are needed which are then verified. These iterations have already been performed in Excel, and the final parameters have been presented here. Given that the depth varies from 10-15m along the north-eastern

breakwater segment, a cross section has been designed for a depth of 15m to which an additional 1.5m have been added to reach the design water level (DWL). The equation below shows the determination of the DWL. Here the highest astronomical tide (HAT) has been determined previously from section 8. The sea level rise (SL) has been taken as 0.17m, as no appropriate estimate is available for the region of Gwadar. Based on reference [69], a rough value of 2.2mm/year for the Arabian Gulf (close to Gwadar in a relative sense) has been presented which amounts to 11 cm over 50 years, hence the figure has been rounded up to give a DWL of 1.5m above the mean sea level (MSL). For the depth at this region, wave setup in not anticipated as depth limiting breaking will not take place.

$$DWL = HAT + SL = 1.33 + 0.17 = +1.5\ m\ MSL$$

Design Wave Height

Based on the extreme value analysis of section 7, The offshore Hs = H_0, for a return period R = 310 years, with 50 year design life , and 15% failure probability, is 3.2m. A scatter plot of Hs and Tp has been made as shown in the figure below. This has been used to find the corresponding Tp (for de-clustered data points) for an Hs = 3.2m. A power law curve fitting has been performed of the type $T_p = aH_s^b$ where a = 8 and b = 0.70. The corresponding $T_p = 15.5s$ which is converted to a T_s by the following relationship, $T_p = T_s\ \frac{1.13}{1.07}$ as taken from [70]. A value of $T_s = 14.7s$ will be used in the design

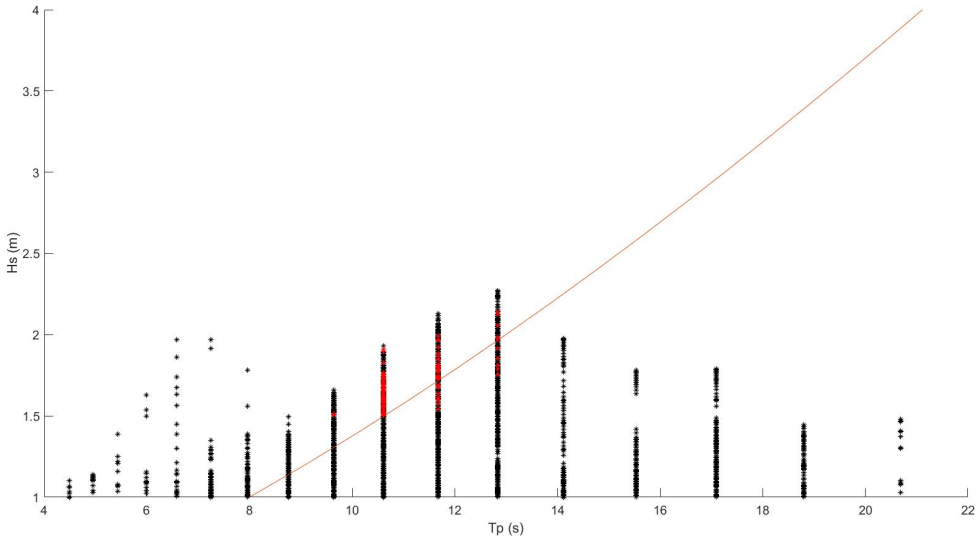

Scatter plot of Hs and Tp

Based on a $T_p = 14.7s$ the corresponding deep water wave length $L_0 = \frac{gT^2}{2\pi} = 337.4m$ is found. The wave obliquity with respect to the breakwater normal is within $12°$, however Goda suggests a reduction by $15°$ to be conservative, hence $\theta = 0$ has been selected for design.The wave heights are found using the equations listed below, where the shoaling coefficient $K_s = 1.1$ from the wave shoaling diagram below.

H_{max} Calculation Coefficients
$\beta_0^* = 0.052(H_0/L_0)^{-0.38}exp[20tan^{1.5}\theta] = 0.305$
$\beta_1^* = 0.63exp[3.8tan\theta] = 0.64$
$\beta_{max}^* = max\ [1.65,\ 0.53(H_0/L_0)^{-0.29}exp[2.4tan\theta]] = 2.05$

$$H_{max} = min[(\beta_0^* H_0 + \beta_1^* h),\ \beta_{max}^* H_0,\ 1.8K_s H_0] = 6.34m \quad (h/L_0 < 0.2)$$

$$H_{1/3} = min[(\beta_0 H_0 + \beta_1 h), \beta_{max} H_0, K_s H_0] = 3.52m \quad (h/L_0 < 0.2)$$

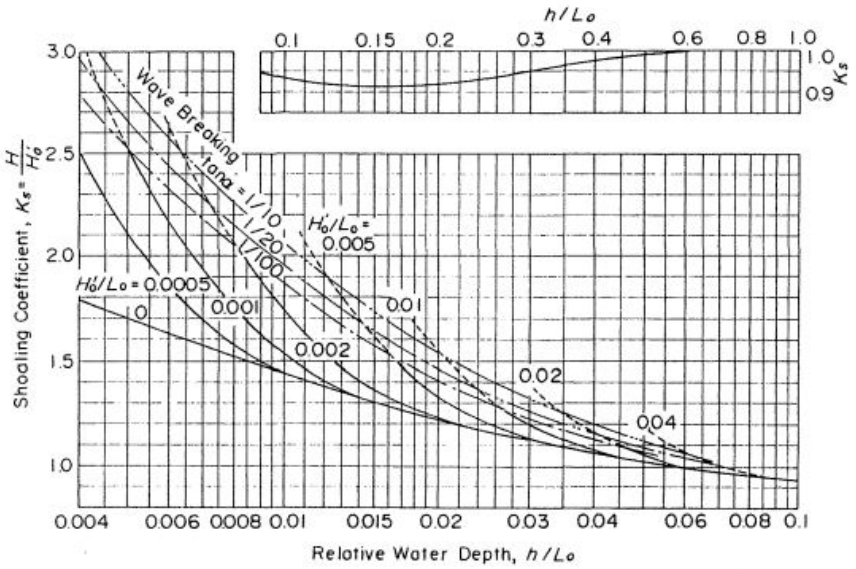

Fig. 4.24 Diagram of nonlinear wave shoaling (Goda, 1985)

Wave shoaling diagram, Takahashi (2002)

$H_{1/3}$ Calculation Coefficients
$\beta_0 = 0.028(H_0/L_0)^{-0.38}exp[20tan^{1.5}\theta] = 0.16$
$\beta_1 = 0.52exp[4.2tan\theta] = 0.53$
$\beta_{max} = max[0.92,\ 0.32(H_0/L_0)^{-0.29}exp[2.4tan\theta] = 1.24$

Based on the above, an $H_D = H_{max} = 6.34m$ has been selected for design. According to the dispersion relationship $\omega^2 = gktanh(kd)$ which has been solved iteratively, the wave length L at the location is found to be 170m.

Calculation of Pressures

At this stage the calculation of the α_I coefficient is done using the equations listed below to check for the risk of impulsive wave breaking, a conditional that can result in disaster for vertical breakwater structures. Provided, impulsive wave breaking does not occur given the selected geometric parameters, the wave pressures will be calculated.

$$\alpha_I = \alpha_{I0}\alpha_{I1} = (0.6604)(0.078) = 0.0517$$

$$\alpha_{I0} = H/d, \quad (H \leq 2d)$$

$$= 2, \quad (H > 2d)$$

$$\alpha_{I1} = cos\delta_2/cosh\delta_1, \quad (\delta_2 \leq 0)$$

$$= 1/[cosh\delta_1(cosh\delta_2)^{0.5}], \quad (\delta_2 > 0)$$

$$\delta_1 = 20\delta_{11}, \quad (\delta_{11} \leq 0)$$

$$= 15\delta_{11}, \quad (\delta_{11} > 0)$$

$$\delta_2 = 4.9\delta_{22}, \quad (\delta_{22} \leq 0)$$

$$= 3\delta_{22}, \quad (\delta_{22} > 0)$$

$$\delta_{11} = 0.93(B_M/L - 0.12) + 0.36[(h-d)/h - 0.6] = -0.1497$$

$$\delta_{22} = -0.36(B_M/L - 0.12) + 0.93[(h-d)/h - 0.6] = -0.1365$$

Based on the above working, $\alpha_I = 0.057$ and the remaining α values required in the wave pressure calculations are calculated using the equations listed below. Since α_I is less than $\alpha_2 = 0.0609$, there is no risk of impulsive wave breaking for the selected geometric design parameters.

$$\alpha_1 = 0.6 + 0.5[(4\pi h/L)/sinh(4\pi h/L)]^2 = 0.911$$

$$\alpha^* = max\ [\alpha_2, \alpha_I] = 0.0609$$

$$\alpha_2 = min[(1 - d/h_b)(H_D/d)^2/3,\ 2d/H_D] = 0.0609$$

$$\alpha_3 = 1 - (h'/h)[1 - 1/cosh(2\pi h/L)] = 0.896$$

$$\alpha_4 = 1 - h_c^*/\eta^* = 0.390$$

$$h_c^* = min[\eta^*,\ h_c] = 5.8m$$

Now the wave pressures are calculated using the equations below. Here $W_0 = \rho_{sea} g = (1025)(9.81)$, is the weight of sea water. All modification factors $\lambda_{1,2,3}$ has been taken as unity because formulations do not exist specifically for U-OWC type vertical caissons.

$$\eta^* = 0.75(1 + cos\theta)\lambda_1 H_D = 9.51m$$

$$p_1 = 0.5(1 + cos\theta)(\lambda_1\alpha_1 + \lambda_2\alpha^* cos^2\theta)w_0 H_D = 61,990.72 N/m^2$$

$$p3 = \alpha_3 p_1 = 55,582.04\ N/m^2$$

$$p4 = \alpha_4 p_1 = 24,183.6\ N/m^2$$

$$p_u = 0.5(1 + cos\theta)\lambda_3\alpha_1\alpha_3 w_0 H_D = 52,098.15\ N/m^2$$

The calculated wave pressures are depicted along with their distribution on the figure below. This figure represents the final design geometry achieved via an iterative process. Here the center of gravity of the structure (COG) has been marked with reference to the bottom left corner of the structure with $x_0 = 8.61m$ and $y_0 = 5.93m$. It has been determined using the equation below where m_i is the mass per meter width of each structural element and x_i and y_i are the centroidal distances for each element from the x and y axis. Further a wall thickness of 0.4m has been assumed for all structure walls with $150kg/m^3$ steel reinforcement where $\rho_{conc} = 2300Kg/m^3$ and $\rho_{steel} = 7800kg/m^3$. The U-OWC chamber will be filled with sea water with $\rho_{sea} = 1025kg/m^3$ up till the DWL. Lastly, the structure will make use of sand as a ballast material with $\rho_{sand} = 2600kg/m^3$.

$$x_0 = \frac{\sum m_i x_i}{m_t} = 8.61m,\ from\ bottom\ left\ corner$$

$$y_0 = \frac{\sum m_i y_i}{m_t} = 5.93m,\ from\ bottom\ left\ corner$$

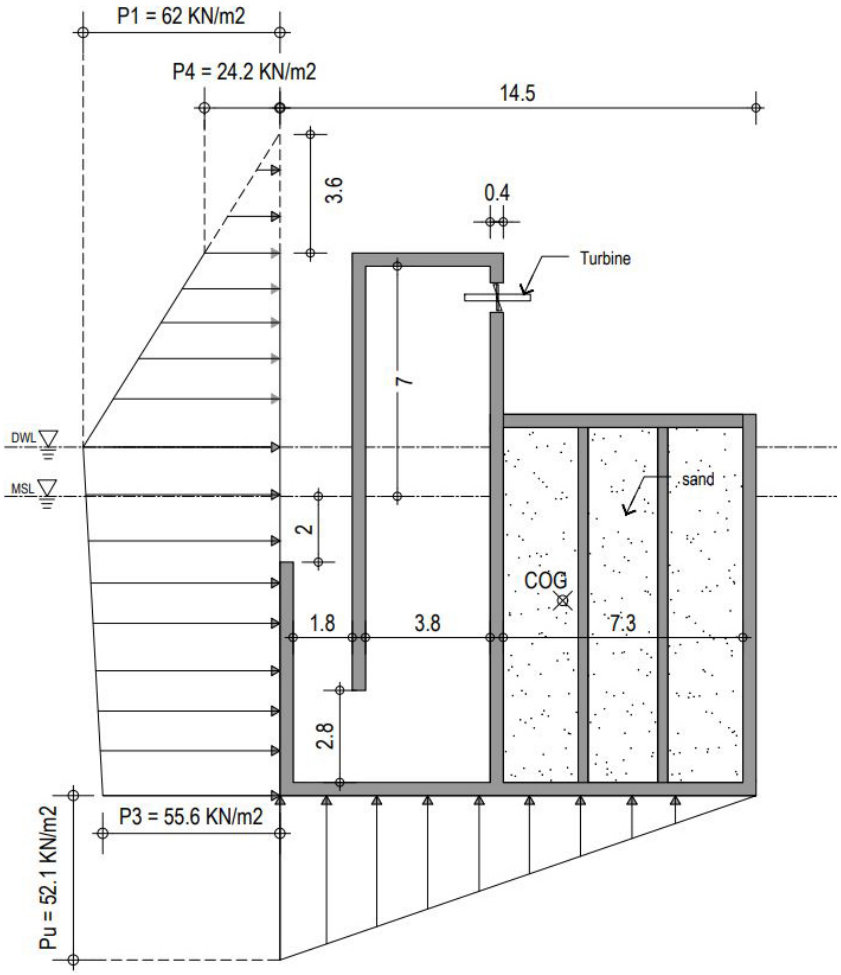

Pressure distribution on structure, as determined by Goda

Calculation of Safety Factors

Given the structure design presented in the figure above, based on the DWL the submerged weight of the structure is calculated by multiplying the volume of the submerged structure elements by ρ_{sea} to find the total buoyancy uplift mass = 96,452.5 kg/m. This is then subtracted from the total structure mass of 367,324.5 kg/m and converted to net weight by multiplication with $g = 9.81m/s^2$. Hence the structures net submerged weight $W' = 2,657,254.32$ N/m.

The safety factor against sliding (SF_s) has been determined using the equation below where all quantities are expressed per meter width. Here the coefficient of friction $\mu = 0.60$ for concrete on a rubble mound foundation, U is the total uplift force, and P the total horizontal wave force.

$$SF_s = \mu \frac{(W' - U)}{P} = 0.6 \frac{(2,657,254.32 - 377,711.57)}{873,041} = 1.57 > 1.2$$

The safety factor against overturning (SF_t) is determined using the equation below where all quantities are per meter width. Here t = 5.88m is the distance in the x direction between the COG and heel (pivot point) of the structure. M_U is the uplift moment and M_p the horizontal force moment.

$$SF_t = \frac{(W't - M_u)}{M_p} = \frac{[(2,657,254.3)(5.88) - 3,651,211.9]}{6,630,361.8} = 1.8 > 1.2$$

The check for bearing pressure at the heel of the structure to prevent a geotechnical failure has been performed using the equation below. Here a max bearing stress limit of 600 KN/m^2 has been taken as mentioned in Takahashi (2002) [63] and the caisson width B = 14.5m.

$$W_e = (W' - U) = (2,657,254.32 - 377,711.6) = 2,279,542.8N/m$$

$$M_e = (W't - M_u - M_p) = [(2,657,254.32)(5.88) - 3,651,211.9 - 6,630,361.8] = 5,366,141.7Nm/m$$

$$t_e = M_e/W_e = 5,366,141.7/2,279,542.8 = 2.35m$$

$$q = \frac{3}{4}\frac{2W_e}{3t_e} = \frac{2(2,279,542.8)}{3(2.35)} = 484.2KN/m^2$$

Rubble Mound Armour and Foot Protection Design

Foot protection block are required immediately in front of the structure due to the formation of standing waves. The size of the blocks has been determined using the figure below. Here $t'/H = 0.17$ and $d/h = 0.70$, which gives a concrete block weight of 15.6 tonnes for the trunk. The dimensions of the block are 3 x 2.5 x 1m. For added safety, the foot protection block will also be placed on the lee side of the structure. The rubble mound slope towards the seaside will be 1:3, and 1:2 for the rear side. These values are typically used for caissons resting on top of a rubble mound foundation. As previously mentioned the berm width will be 5m.

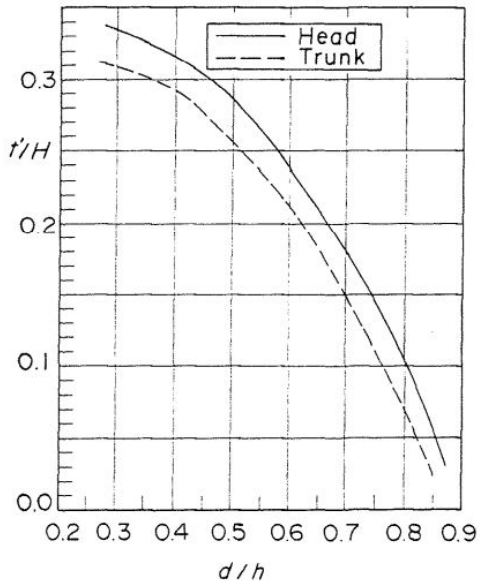

Foot protection block selection curve

In order to determine the dn50 of the armour layer, the stability coefficient N_s needs to be determined. This has been done using the equations listed below, where $k = 2\pi/L'$ and L' = 154m is the wave length at h' = 10.6m. Also $\Delta = 1.54$ has been assumed as the relative density to sea water.

$$(\kappa_2)_B = max[\alpha_s sin^2\theta cos^2(kB_M cos\theta),\ cos^2\theta sin^2(kB_M cos\theta)] = 0.046$$

$$\kappa_1 = (2kh')/sinh2kh' = 0.87$$

$$\kappa = \kappa_1(\kappa_2)_B = 0.04$$

$$N_s = max[1.8,\ 1.3[(1-\kappa)/\kappa^{1/3}](h'/H_{1/3}) + 1.8exp[-1.5[(1-\kappa)^2/\kappa^{1/3}](h'/H_{1/3}) = 10.95$$

$$dn50 = \frac{H_{1/3}}{N_s \Delta} = 0.21m$$

For the sake of conservative design, and looking at the available gradings, a dn50 = 0.34m has been selected from the LMA (40-200 kg) class. The thickness of the armour layer $t_a = 0.60m$ is determined based on the equation listed in chapter 3 of the rock manual [66]. Here n=2 is the number of layers, and $k_t = 0.87$ is a layer coefficient assuming irregular rock.

$$t_a = nk_t dn50 = 0.60m$$

Under Layer/ Filter Design

It has been opted to utilize a geometrically closer filter for the under layer design instead of a granular filter for which multiple layers would be required. The equations for filter criterion pertaining to stability, internal stability , and permeability in the presence of waves has been listed below [65]. Here the subscript f and b correspond to filter and base layer pairs for a diameter (D) passing fraction.

$$\frac{D_{15f}}{D_{85b}} \leq 4$$

$$\frac{D_{50f}}{D_{50b}} \leq 7$$

$$\frac{D_{15f}}{D_{15b}} \leq 7$$

For a particular selection of a grading, the corresponding diameter (D_y) or mass (M_y) passing fraction y are calculated using the Rosin Rammler equations mentioned in chapter 3 of the Rock manual [66], shown below.

$$D_y = D_{50} \left[\frac{ln(1-y)}{ln\frac{1}{2}} \right]^{1/n_{RRD}}$$

$$n_{RRM} = log \left[\frac{ln(1-y_{NUL}}{ln(1-y_{NLL}} \right] / log(NUL/NLL)$$

$$n_{RRD} = 3n_{RRM}$$

In these equations D can be replaced by M, so long as the appropriate uniformity coefficient n_{RRD} for diameters, and n_{RRM} for mass fractions is used. The nominal upper limit (NUL) and nominal lower limit (NLL) are defined by the standard grading. A series of iterations were performed in Excel to find the ideal grading of CP(90/250mm) for the under layer. The data along with filter criteria checks for this grading the armour layer LMA (40-200)kg are shown below. Both grading belongs to the EN 13383 family of grading requirements.

Under layer: CP (90/250mm) Grading	
y (fraction)	$D_y(mm)$
0.10	60.48
0.15	71.48
0.50	125.01
0.60	139.21
0.85	184.27

Based on the diameters (D) for the passing fractions y listed in the table above, the filter criteria can be checked as follows. It can be seen that the grading sandwich between armour and under layer is appropriate. Given the d50 of the under layer is 0.13m, three times this value has been taken for the layer thickness = 0.40m.

The material for the core will not come from a standard grading to avoid excessive cost. Based on $\frac{D_{50f}}{D_{50b}} \leq 7$, the core will be quarry run material with dn50 = 0.06m. The height of the core will be altered along the alignment of the breakwater as the depth varies between 10-15 m MSL.

Armour: LMA (40-200kg) Grading	
y (fraction)	$D_y(mm)$
0.10	0.22
0.15	0.25
0.50	0.34
0.60	0.36
0.85	0.42

$$\frac{D_{15f}}{D_{85b}} = 1.33 \leq 4$$

$$\frac{D_{50f}}{D_{50b}} = 2.7 \leq 7$$

$$\frac{D_{15f}}{D_{15b}} = 3.4 \leq 7$$

Toe Design

Typically toe design stability is assessed with the equations below taken from CIE5308 lecture notes [56]. **However this equation is only valid for** $h_t/H_s < 2$**, here** $h_t = d = 9.6m$ **and** $H_s = 3.52m$ **which gives a value of** $2.7 > 2$**.**

$$\frac{H_s}{\Delta d_{n50}} = \left(6.2\frac{h_t}{h} + 2\right) N_{od}^{1.5}, \;\; 0.4 < h_t/h < 0.9$$

$$\frac{H_s}{\Delta d_{n50}} = \left(0.24\frac{h_t}{d_{n50}} + 1.6\right) N_{od}^{0.15}, \;\; 3 < h_t/d_{n50} < 25$$

Therefore, an alternative check for toe stability has been performed. It involves the calculation of the orbital velocity u_x given an $Hs = 3.52m$ and its corresponding bed shear stress. Then given a Shield's stability value of $\psi = 0.03$, a value of dn50 is determined. These equations have been taken from the book Introduction to Bed Bank and Shore Protection [65]. Here $H_s = 3.52m$, h = 16.5 m (DWL), and L = 170m.

$$u_x = \omega a \frac{cosh[k(h+z)]}{sinh(kh)} = 1.15m/s$$

$$c_f = 0.237\left(\frac{a_b}{K_r}\right)^{-0.52} = 0.0426 \;\; k_r = 0.1 \;\; fine\ sand$$

$$a_b = \frac{0.5H}{sinh(kh)} = 2.71$$

$$\tau_w = 0.5\rho_{sea} c_f u_x^2 = 29N/m^2$$

$$dn50 = \frac{\tau_w}{\psi(\rho_s - \rho_{sea})g} = 6.25cm$$

Given that the under layer dn50 = 0.13m (CP 90/250mm), it has been decided to extent it parallel to the seabed for an additional length to ensure stability of the toe. Based on the bed shear stress calculated above, the grains are not anticipated to mobilize. The total protection length is extending to more than 0.15L and hence is safe against scour. Additionally, to prevent loss of sediment from the sea bed, a geo-textile will be placed underneath the toe to prevent loss of material. The geo-textile will have an $O90 < 3d90$ of the seabed sand (information for which is not known).

Overtopping Calculation
The overtopping discharge is calculated using the procedure outlined in the EurOtop manual (2018) using the equation mentioned below. This equation is valid under the assumption that there is no effect of the foreshore, in other words, the ratio of depth at the toe divided by Hs is greater than 4, as mentioned in the EurOtop manual. This is the case for the U-OWC caisson as 16.5/3.52 = $4.6 > 4$.

$$\frac{q}{(gH_{m0}^3)^{0.5}} = 0.054exp\left[-\left(2.12\frac{R_c}{H_{m0}}\right)^{1.3}\right]$$

Using this equation a discharge of q = 6.93 L/s per meter is found for the current design. This value seems reasonable for the vertical caisson breakwater. The EurOtop manual states that values lower than 10 L/s per meter are typically adequate. Additionally, it has been assumed that the turbine housing will be protected (water proof) from the overtopping discharge. It is also anticipated that this overtopping discharge will not create excessive disturbances in the lee side.

Design Cross Section
Based on all of the working presented above, the final design geometry is shown in the figure below. It is important to mention that geo-technical design and stability of the sub-sea soil strata are not within the scope of this report. The figure below depicts the cross section at a depth of 15m, this value then decreases to 10m towards the shore for the north-eastern segment. Given that the U-OWC duct submergence is fixed with reference to the mean sea level, The height (volume) of the core will be decreasing going towards shallow water. At the 10m depth location, either a shallow core will be created or the seabed will be excavated by 1-2m to ensure sufficient bearing strength - subject to geotechnical study. All dimension are given in meters.

Additionally, it is worth mentioning that no specific formulations exist for the design of the lee side of the rubble mound foundation. Considering that the lee side will experience tranquil conditions, the under layer material will suffice as protection, additionally, a foot protection block will also be placed at the structure heel. A transmission calculation has not been undertaken as the equation are highly empirical in nature, the coefficient for which is not appropriate for a U-OWC device which is absorbing wave energy.

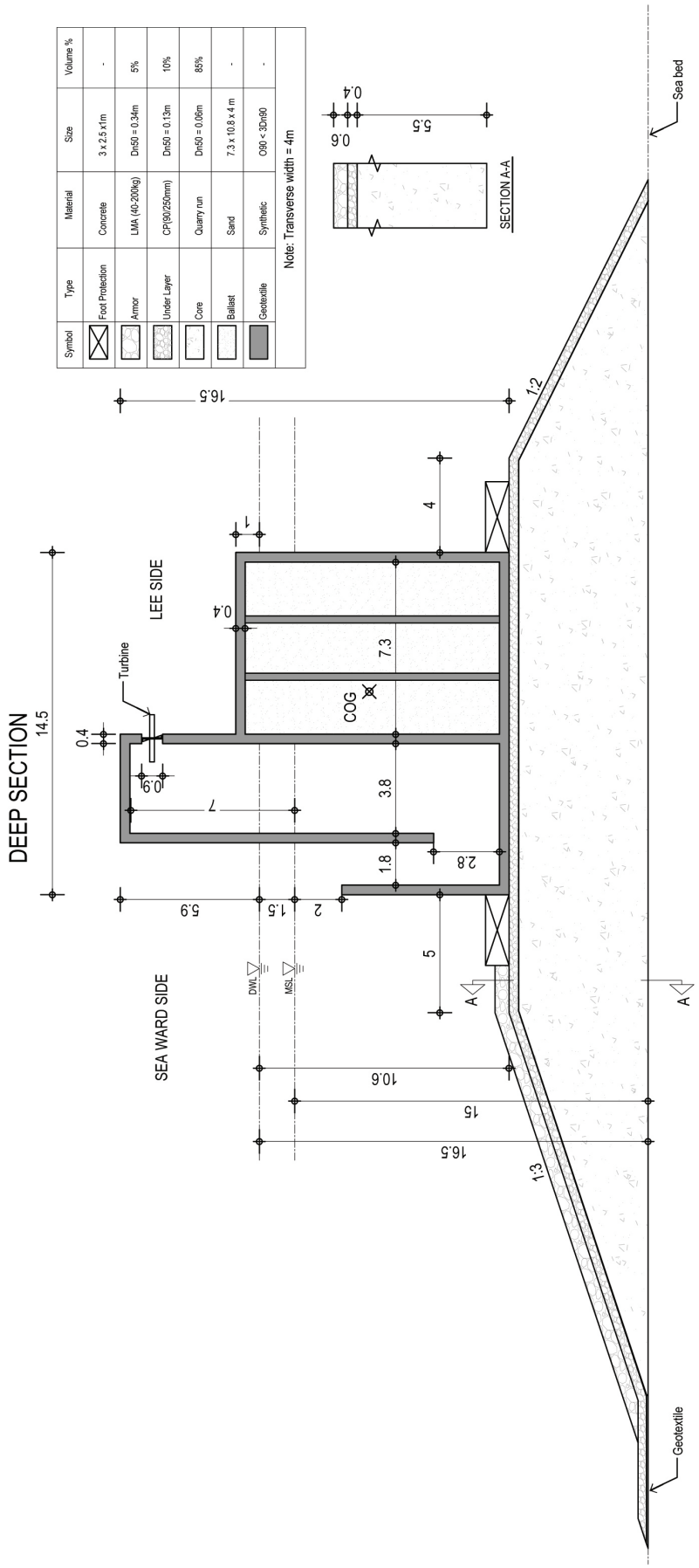

Final U-OWC caisson cross section, depth of 15m MSL

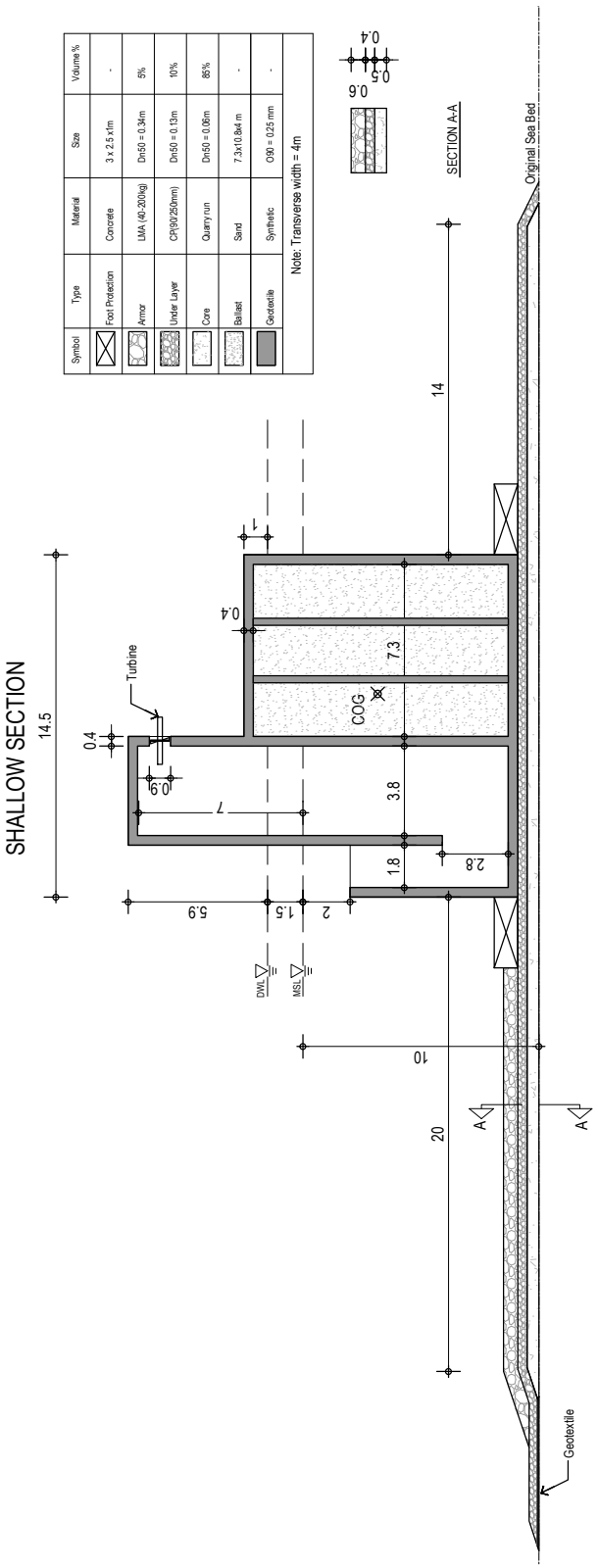

Final U-OWC caisson cross section, depth of 10m MSL

E

Material Rates and Costing Calculations

Shown in the two images below are the material rates (placement and labour inclusive) provided by local consultants for a previous breakwater project in Karachi, 2011. These rates are used to calculate the total cost of the 1.8km north-eastern segment of the proposed rubble mound breakwater, and the U-OWC caisson breakwater. A few aspects to consider have been listed below.

- The cost of the rubble mound breakwater (option-3), as mentioned is around 199 million USD for the entire structure with a length of 2.1km. This cost is valid for the year 2018 and presented as a lump sum for which a break-up is not available.
- local consultant provided material rates will be used to re-calculate the breakwater cost just for the 1.8km north-eastern segment. The provided material rate will be escalated by 9% as advised by local consultants over 7 years to bring them to the year of 2018.
- The cost of the U-OWC caisson breakwater will be calculated for the north-eastern segment for the year of 2018. It will make use of the material cost provided by local consultants for the rubble mound foundation it will sit on.
- All rates are provided in Pakistani Rupees (PKR) and will be converted to US dollars (USD) with an average exchange rate of 1 USD = 121.57 PKR in 2018 (https://www.exchangerates.org.uk/).
- The commonly know formula, $FV = PV(1 + r)^n$ for converting present values (PV) to future values (FV) over a period n with interest rate r will be used.
- The costing analysis for both breakwater option will be done by breaking them up into segments with a transverse width of 4.8m along the 1.8km alignment, giving a total of 375 segments. This is done because the each U-OWC caisson is 4.8m wide (b3 = 4m plus 0.4m wall thickness on both sides).
- The north-eastern breakwater alignment (option-3) has length of 1.8km and experiences an approximately linear depth variation between 10-15m. See figure 9.1 in section 9.1.

The first task is to calculate the cost of the rubble mound breakwater for the 1.8km north-eastern segment which experiences a depth variation between 10-15m. In order to quantify the reduction in material quantities with decreasing depth, a cross section is made at both 10 and 15 m of depth. This cross section has been re-created using information provided by local consultants. The images below show the cross section at both depths, as can be seen the 15m depth cross section comprises of significantly more material quantity.

The volume for each component in the rubble mound breakwater is calculated for a 4.8m segment at 15m and 10m depth. Next, the delta difference in volume for each component is calculated and divided by the number of segments (375) along the entire north-eastern alignment. The table below lists the volume reduction of each component in the rubble mound going from 15-10m. This has been done so that the cost variation of each segment with depth can be determined.

Now the cost for each component needs to be determined, this is done with provided rates that have been brought forward to the year 2018. The table below lists the rates for the rubble mound breakwater in USD (converted from PKR) for various components. Here, the armor unit rate is inclusive of material,

Component	Volume reduction per section (m^3)
Armour	0.19
Under layer	0.34
Core	3.9

Volume reduction going from (15-10m) per 4.8m breakwater segment, rubble mound

storage, and placement cost. Based on this table, it can be seen that the material cost of the 1.8km north-eastern segment of the rubble mound, as calculated by the provided rates, is approximately 174.4 million USD. This cost looks reasonable considering that the total cost for the entire 2.1km rubble mound breakwater as indicated in the lead consultant report was around 199 million USD.

Component	Unit	Rate (USD)	Quantity	Total (USD)
Armour unit	no.	1,054	59,718	69,973,579
Under layer	m^3	197	260,514	51,238,670
Core	m^3	50	926,705	45,566,808
Toe	m^3	197	70,038	13,775,283
Geotextile	m^2	50	16,200	796,566
Total Cost (USD) = 174.4 Million				

Material rates for rubble mound breakwater components in the year 2018

A similar procedure as mentioned above, is undertaken to calculate the cost of the U-OWC caisson breakwater for the north-eastern segment. Based on the design cross sections presented in section 9.6 (and appendix D), the volume reduction for each 4.8m long section is calculated going from 15-10 m depth. The results of this are presented in the table below. Here it has been assumed that the changes in bathymetry will be accounted for by variations in the rubble mound foundation height. The U-OWC caisson geometry, volume, and submergence with reference to MSL will be constant across the entire breakwater alignment.

Component	Volume reduction per section (m^3)
Armour	0.008
Under layer	0.01
Core	1.21

Volume reduction going from (15-10m) per 4.8m breakwater segment, U-OWC caisson

To compute the total cost of the U-OWC caisson breakwater, 3 issues need to be dealt with which are as follows. A caisson breakwater has not yet been made in Pakistan and no local rates are available for caisson construction and placement. To assist with this, the work of Tutuarima et al (1998) [67] has been used where the cost of a caisson (all in) is 500 Dutch guilders (ANG) per m^3 in 1998. Based on a global inflation rate of 3.4% [71] this cost has been brought forward to 2018 and converted to USD with an exchange rate of 1 ANG = 0.55 USD taken from xe.com. Therefore, the cost per 285.8 m^3 caisson is 153,393 USD.

The next issue pertains to the cost of ground improvement measures typically required for vertical breakwaters. Given, that limited sub-soil information is available, and to avoid significant geotechnical complexity, a cost of 25,000 USD/m (equivalent to 500 USD/m^2) for the entire alignment of 1.8km has been assumed. This value is recommended by local consultants to be conservative in case soil replacement or strengthening measures are required as vertical caisson breakwaters are more sensitive to geological conditions.

The last issue related to the cost of the PTO system per U-OWC chamber which comprises of a wells turbine, generator, and electrical accessories. An appropriate reference for PTO system cost cannot be found in publicly available information. Hence a cost of 12,500 USD/caisson for the PTO system has been assumed.

Therefore, utilizing the assumptions mentioned above, the total cost of the U-OWC caisson breakwater for the 1.8km north-eastern segment is calculated as shown in the table below. This total cost

of 145.2 million USD will be referred to as the 'base total cost,' and subject to a sensitivity analysis in section 10, where the caisson, ground improvement, and PTO cost will be altered.

Component	Unit	Rate (USD)	Quantity	Total (USD)
Armour	m^3	236	20,342	4,800,978
Under layer	m^3	236	41,348	9,758,919
Core	m^3	50	281,722	16,622,958
Geotextile	m^2	50	11,700	690,358
Caisson	no.	153,393	375	57,522,395
Foot block	no.	4,247	1,440	6,114,995
Ground improvement	m	25,000	1800	45,000,000
PTO	no.	12,500	375	4,687,500
Total Cost (USD) = 145.2 Million				

Material rates for U-OWC caisson breakwater components in the year 2018

Item	Descriptions		Unit	Estimated Quantity	Engineer's Estimate (E.E)	
					Rate (PKR)	Amount (PKR)
	Rock Armour	S 2.0	m^3			
	Supply and Place		m^3			
6.3.1	Quarry-run material	- do -	m^3	85,700	3,000.00	257,100,000.00
6.3.2	1.2t rock armour	- do -		29,900	6,500.00	194,350,000.00
6.3.3	3.0t rock armour	- do -		3,300	6,500.00	21,450,000.00
	CORE-LOC™ units	S 2.3.0 to S 2.4.10	No.			
	Precast mass concrete CORE-LOC™ units as primary armour, $3.9m^3$		No.			
6.3.10	Supply materials and cast unit	- do -	No.	3,908	35,000.00	136,780,000.00
6.3.11	Handle, transport and store	- do -	No.	3,908	10,000.00	39,080,000.00
6.3.12	Handle, transport and place	- do -		3,908	35,000.00	136,780,000.00
6.3.13	Set formwork for unit handed over to employer	- do -		1	600,000.00	600,000.00
	Geotextile Fabric		m^2			
6.3.30	Geotextile materials and placing	- do -		8,300	3,000.00	24,900,000.00
	Provisional Items		hrs			
	Standing time on the instructions of the Engineer					
6.3.40	Rock placing Plant: (Bidder to specify)		hrs	100	3,000.00	300,000.00
	Standing time on the instructions of the Engineer					
6.3.41	CORE-LOC™ Units placing Plant: (Bidder to specify)			100	6,000.00	6,000.00
	Bill 6.3 Summary Carried to GRAND SUMMARY					**811,940,000.00**

Breakwater project rates for 2011 from Karachi, provided by local consultants

Item	Descriptions	Unit	Estimated Quantity	Engineer's Estimate (E.E)	
				Rate (PKR)	Amount (PKR)
	Rock Armour				
	Supply and Place				
6.4.1	Quarry-run material	m^3	301,600	3,000.00	904,800,000.00
6.4.2	0.3t rock armour	m^3	33,600	6,500.00	218,400,000.00
6.4.3	0.6t rock armour	m^3	25,300	6,500.00	164,450,000.00
6.4.4	1.2t rock armour		61,300	6,500.00	398,450,000.00
6.4.5	3.0t rock armour		58,400	6,500.00	379,600,000.00
	CORE-LOC™ unit				
	Precast mass concrete CORE-LOC™ units as primary armour, 3.9m^3				
6.4.10	Supply materials and cast unit	No.	8,083	35,000.00	282,905,000.00
6.4.11	Handle, transport and store	No.	8,083	10,000.00	80,830,000.00
6.4.12	Handle, transport and place		8,083	35,000.00	282,905,000.00
6.4.13	Set formwork for unit handed over to employer	No.	1	600,000.00	600,000.00
	CORE-LOC™ unit				
	Pre Cast Mass Concrete ***CORE-LOC™ units as Primary Armour 0.7 m^3***				
6.4.14	Supply Material and Cast unit	No.	19926	-	-
6.4.15	Handle, Transport and Store	No.	19926	-	-
6.4.16	Handle, Transport and Place	No.	19926	-	-

Breakwater project rates for 2011 from Karachi, provided by local consultants

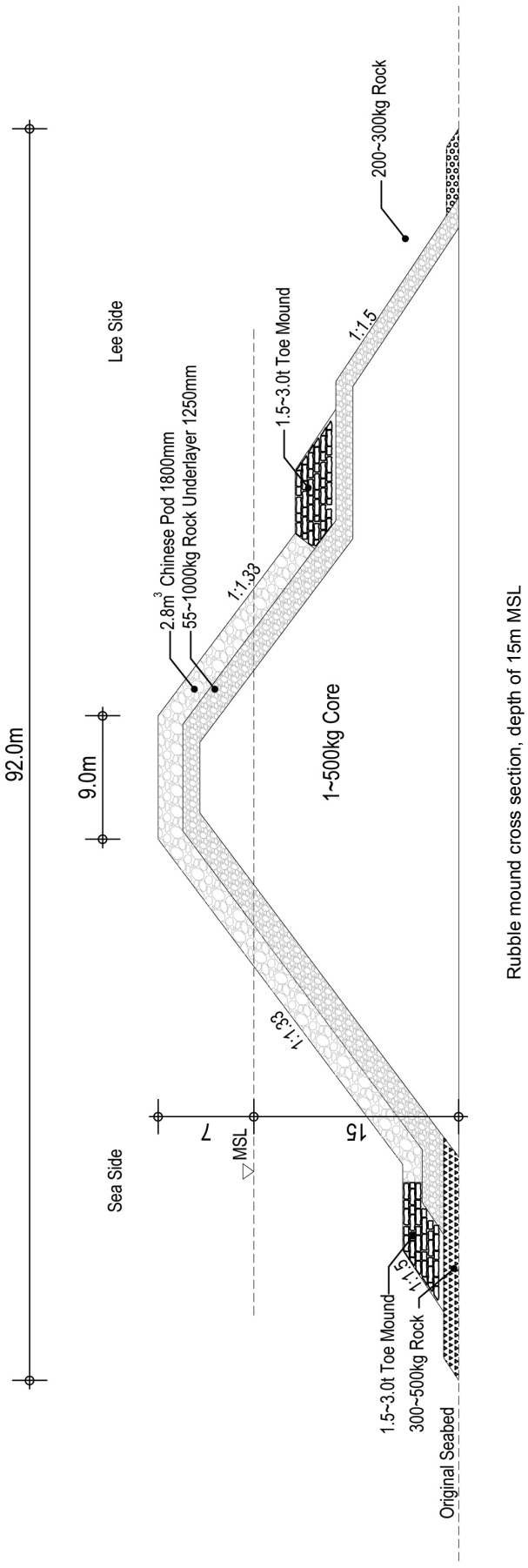

Rubble mound cross section, depth of 15m MSL

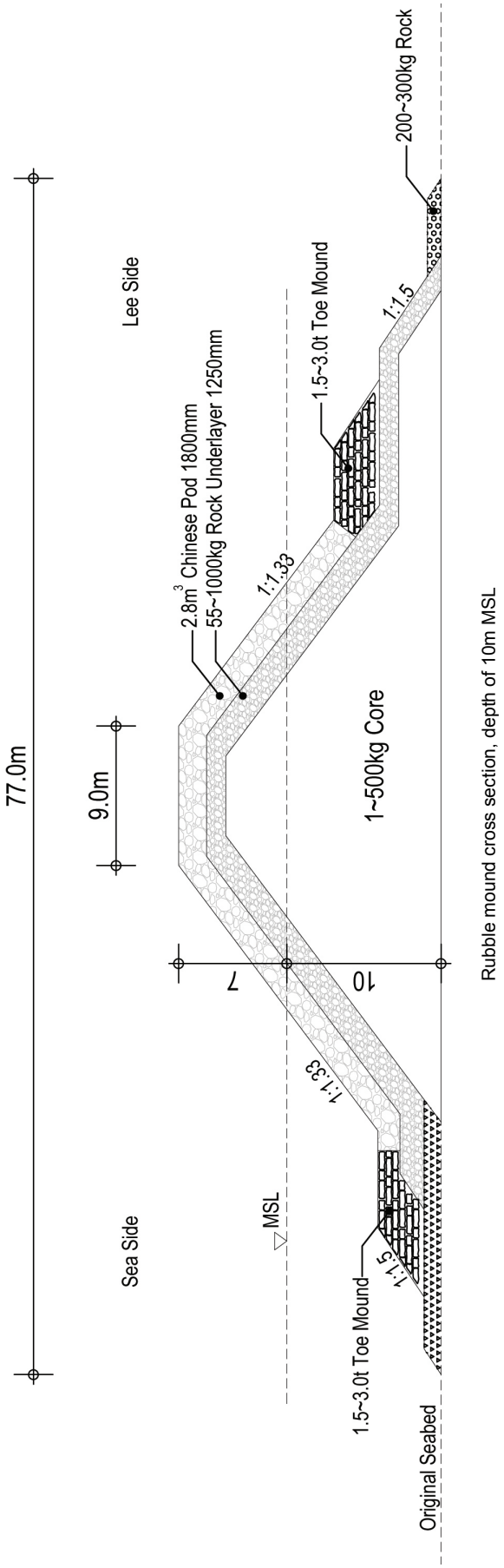

Rubble mound cross section, depth of 10m MSL

References

[1] Behrang Chenari, Seyedeh Shiva Saadatian, and Almerindo Ferreira. “Wave energy systems: An overview of different wave energy converters and recommendation for future improvements”. In: *Proceedings of the 8th International Technology, Education Development Conference, Valencia, Spain*. 2014, pp. 10–12.

[2] George Lavidas and Kornelis Blok. “Shifting wave energy perceptions: The case for wave energy converter (WEC) feasibility at milder resources”. In: *Renewable Energy* 170 (2021), pp. 1143–1155.

[3] Frank Neumann Ruud Kempener. “Wave Energy Technology Brief”. In: *Ocean Energy Technology Brief* 4 (2014).

[4] Avri Eitan. “Promoting Renewable Energy to Cope with Climate Change—Policy Discourse in Israel”. In: *Sustainability* 13.6 (2021), p. 3170.

[5] Dolf Gielen et al. “The role of renewable energy in the global energy transformation”. In: *Energy Strategy Reviews* 24 (2019), pp. 38–50.

[6] Muhammad Abid. “Gwadar Port and CPEC: Connecting China with Middle East”. In: *Note for Contributors* (), p. 18.

[7] Massarrat Abid and Ayesha Ashfaq. “CPEC: Challenges and opportunities for Pakistan”. In: *Journal of Pakistan Vision* 16.2 (2015), pp. 142–169.

[8] SGMD Hashmi and Sajid Rashid Ahmad. “GIS-Based analysis and modeling of coastline erosion and accretion along the coast of Sindh Pakistan”. In: *Journal of Coastal Zone Management* 21.1 (2018), pp. 1–7.

[9] Mazhar Hussain Baloch et al. “Hybrid energy sources status of Pakistan: An optimal technical proposal to solve the power crises issues”. In: *Energy Strategy Reviews* 24 (2019), pp. 132–153.

[10] Johannes Falnes. “A review of wave-energy extraction”. In: *Marine structures* 20.4 (2007), pp. 185–201.

[11] Seongho Ahn. “Modeling mean relation between peak period and energy period of ocean surface wave systems”. In: *Ocean Engineering* 228 (2021), p. 108937.

[12] Tunde Aderinto and Hua Li. “Review on power performance and efficiency of wave energy converters”. In: *Energies* 12.22 (2019), p. 4329.

[13] Benjamin Drew, Andrew R Plummer, and M Necip Sahinkaya. “A review of wave energy converter technology”. In: *Proceedings of the Institution of Mechanical Engineers, Part A: Journal of Power and Energy* 223.8 (2009), pp. 887–902.

[14] Diana Bull and Margaret E Ochs. “Technological cost-reduction pathways for attenuator wave energy converters in the marine hydrokinetic environment”. In: *Sandia National Laboratories, Tech. Rep* (2013).

[15] JC Martins et al. “Geometric evaluation of the main operational principle of an overtopping wave energy converter by means of Constructal Design”. In: *Renewable Energy* 118 (2018), pp. 727–741.

[16] Felice Arena et al. “Installing U-OWC devices along Italian coasts”. In: *International Conference on Offshore Mechanics and Arctic Engineering*. Vol. 55423. American Society of Mechanical Engineers. 2013, V008T09A061.

[17] Robert E Harris, Lars Johanning, and Julian Wolfram. “Mooring systems for wave energy converters: A review of design issues and choices”. In: *Marec2004* (2004).

[18] John C Mankins et al. “Technology readiness levels”. In: *White Paper, April* 6.1995 (1995), p. 1995.

[19] Davide Magagna, Riccardo Monfardini, and Andreas Uihlein. “JRC ocean energy status report 2016 edition”. In: *Publications Office of the European Union: Luxembourg* (2016).

[20] Aurélien Babarit. “A database of capture width ratio of wave energy converters”. In: *Renewable Energy* 80 (2015), pp. 610–628.

[21] Grace Chang et al. “A comprehensive evaluation of factors affecting the levelized cost of wave energy conversion projects”. In: *Renewable energy* 127 (2018), pp. 344–354.

[22] Davide Magagna, Riccardo Monfardini, and Andreas Uihlein. “JRC ocean energy status report”. In: *Publications Office of the European Union: Luxembourg* (2016).

[23] António FO Falcão and Joao CC Henriques. “Oscillating-water-column wave energy converters and air turbines: A review”. In: *Renewable Energy* 85 (2016), pp. 1391–1424.

[24] TV Heath. “A review of oscillating water columns”. In: *Philosophical Transactions of the Royal Society A: Mathematical, Physical and Engineering Sciences* 370.1959 (2012), pp. 235–245.

[25] Leo H Holthuijsen. *Waves in oceanic and coastal waters*. Cambridge university press, 2010.

[26] Simeon Doyle and George A Aggidis. “Development of multi-oscillating water columns as wave energy converters”. In: *Renewable and Sustainable Energy Reviews* 107 (2019), pp. 75–86.

[27] Damon Howe, Jean-Roch Nader, and Gregor Macfarlane. “Experimental investigation of multiple oscillating water column wave energy converters integrated in a floating breakwater: energy extraction performance”. In: *Applied Ocean Research* 97 (2020), p. 102086.

[28] Diego Vicinanza et al. “Review of innovative harbor breakwaters for wave-energy conversion”. In: *Journal of Waterway, Port, Coastal, and Ocean Engineering* 145.4 (2019), p. 03119001.

[29] A Scialò et al. “Power take-off selection for a fixed U-OWC wave power plant in the Mediterranean Sea: The case of Roccella Jonica”. In: *Energy* 215 (2021), p. 119085.

[30] Paolo Boccotti. “Comparison between a U-OWC and a conventional OWC”. In: *Ocean Engineering* 34.5-6 (2007), pp. 799–805.

[31] António FO Falcão, João CC Henriques, and Luís MC Gato. “Self-rectifying air turbines for wave energy conversion: A comparative analysis”. In: *Renewable and Sustainable Energy Reviews* 91 (2018), pp. 1231–1241.

[32] Abdus Samad and R Suchithra. “Marine power technology—wave energy”. In: (2021), pp. 241–267.

[33] Ajit Thakker and Fergal Hourigan. “Modeling and scaling of the impulse turbine for wave power applications”. In: *Renewable Energy* 29.3 (2004), pp. 305–317.

[34] A Scialò et al. “Selection of a PTO system and a relief valve for the Roccella Jonica wave power plant”. In: *Developments in Renewable Energies Offshore*. CRC Press, 2020, pp. 254–261.

[35] WAVENERGY.IT. *The first word wide application at the full-scale of REWEC3 device in the port of Civitavecchia*. `https://www.wavenergy.it/generico/the-first-worldwide-application-at-full-scale-of-the-rewec3-device-in-the-port-of-civitavecchia/`. 2014.

[36] Felice Arena et al. “Wave climate analysis for the design of wave energy harvesters in the Mediterranean Sea”. In: *Renewable Energy* 77 (2015), pp. 125–141.

[37] Giovanni Bracco. “Productivity analysis of different design for OWC nearshore in breakwater in Pantelleria”. PhD thesis. Politecnico di Torino, 2021.

[38] JCC Henriques et al. “Dynamics and control of air turbines in oscillating-water-column wave energy converters: Analyses and case study”. In: *Renewable and Sustainable Energy Reviews* 112 (2019), pp. 571–589.

[39] A Falcão. “Developments in oscillating water column wave energy converters and air turbines”. In: *Renewable Energies Offshore. London: Taylor & Francis Group* (2015), pp. 3–11.

[40] AF de O Falcão. “The shoreline OWC wave power plant at the Azores”. In: *Proceedings of 4th European Wave Energy Conference*. 2000, pp. 42–47.

[41] Matthew Folley, Richard Curran, and Trevor Whittaker. “Comparison of LIMPET contra-rotating wells turbine with theoretical and model test predictions”. In: *Ocean Engineering* 33.8-9 (2006), pp. 1056–1069.

[42] Guo Lihui. “Applicability and potential of wave power in China”. MA thesis. Kungsbäcksvägen 47, 801 76 Gävle, Sweden: University of Gavle, 2010.

[43] Dahai Zhang, Wei Li, and Yonggang Lin. “Wave energy in China: Current status and perspectives”. In: *Renewable energy* 34.10 (2009), pp. 2089–2092.

[44] Korea Ocean, Research, and Development Institute. “An OWC Project in Jeju Island,Korea”. In: *https://www.wavec.org/contents/files/15–keyyong-hong-.pdf* (2015).

[45] O Malmo and A Reitan. “Development of the Kvaerner multiresonant OWC”. In: *Hydrodynamics of Ocean Wave-Energy Utilization*. ResearchGate, 1986, pp. 57–67.

[46] Leigh D Appleyard. “Design and Construction of GreenWAVE Energy Converter for Shallow Waters off South Australia”. In: *Journal of Civil Engineering and Architecture* 9 (2015), pp. 1179–1184.

[47] Paolo Boccotti. “Caisson breakwaters embodying an OWC with a small opening—Part I: Theory”. In: *Ocean Engineering* 34.5-6 (2007), pp. 806–819.

[48] Paolo Boccotti et al. “Caisson breakwaters embodying an OWC with a small opening—Part II: A small-scale field experiment”. In: *Ocean Engineering* 34.5-6 (2007), pp. 820–841.

[49] G Malara et al. “The influence of three-dimensional effects on the performance of U-type oscillating water column wave energy harvesters”. In: *Renewable Energy* 111 (2017), pp. 506–522.

[50] Giovanni Malara and Felice Arena. “Response of U-Oscillating Water Column arrays: semi-analytical approach and numerical results”. In: *Renewable Energy* 138 (2019), pp. 1152–1165.

[51] Giovanni Malara and Pol D Spanos. “Efficient determination of nonlinear response of an array of Oscillating Water Column energy harvesters exposed to random sea waves”. In: *Nonlinear Dynamics* 98.3 (2019).

[52] John Brian Roberts and Pol D Spanos. *Random vibration and statistical linearization*. Courier Corporation, 2003.

[53] Gwadar Port Authority. *Gwadar Port Master Plan*. `http://www.gwadarport.gov.pk/masterplan.aspx`. 2022.

[54] George Lavidas and Henk Polinder. “North sea wave database (NSWD) and the need for reliable resource data: A 38 year database for metocean and wave energy assessments”. In: *Atmosphere* 10.9 (2019), p. 551.

[55] Mostafa Beyramzade, Seyed Mostafa Siadatmousavi, and Mahyar Majidy Nik. “Skill assessment of SWAN model in the red sea using different wind data”. In: *Regional Studies in Marine Science* 30 (2019), p. 100714.

[56] H.J. Verhagen J.P van den Bos. *Breakwater Design Lecture Notes CIE5308*. Delft University of Technology, 2018.

[57] Eric Gilleland and Richard W Katz. “extRemes 2.0: an extreme value analysis package in R”. In: *Journal of Statistical Software* 72 (2016), pp. 1–39.

[58] Nicholas R Moloney, Davide Faranda, and Yuzuru Sato. “An overview of the extremal index”. In: *Chaos: An Interdisciplinary Journal of Nonlinear Science* 29.2 (2019), p. 022101.

[59] Marielle Pinheiro and Richard Grotjahn. *An introduction to extreme value statistics*. 2015.

[60] Rich Pawlowicz, Bob Beardsley, and Steve Lentz. “Classical tidal harmonic analysis including error estimates in MATLAB using T_TIDE”. In: *Computers & Geosciences* 28.8 (2002), pp. 929–937.

[61] Judith Bosboom and Marcel J.F. Stive. *Coastal Dynamics I Lecture Notes CIE4305*. Delft University of Technology, 2015.

[62] Felice Arena et al. “On design and building of a U-OWC wave energy converter in the Mediterranean Sea: a case study”. In: *International Conference on Offshore Mechanics and Arctic Engineering*. Vol. 55423. American Society of Mechanical Engineers. 2013, V008T09A102.

[63] Shigeo Takahashi. “Design of vertical breakwaters”. In: *PHRI reference document nr. 34* (2002).

[64] Yoshimi Goda and Hiroshi Takagi. “A reliability design method of caisson breakwaters with optimal wave heights”. In: *Coastal Engineering Journal* 42.4 (2000), pp. 357–387.

[65] Gerrit J Schiereck. *Introduction to bed, bank and shore protection*. CRC Press, 2017.

[66] CIRIA. *The Rock Manual. The use of rock in hydraulic engineering*. CIRIA C683, 2007.

[67] WH Tutuarima and K d’Angremond. “Cost comparison of breakwater types”. In: *Coastal Engineering 1998*. 1999, pp. 1934–1944.

[68] Karachi Electric Utility. *Tariff Structure*. `https://www.ke.com.pk/customer-services/tariff-structure/`. 2022.

[69] AO Alothman et al. “Sea level rise in the north-western part of the Arabian Gulf”. In: *Journal of Geodynamics* 81 (2014), pp. 105–110.

[70] Kowo Andah. *Technical Instructions for the design of Maritime Dikes*. Ministry of public works Consiglio Superiore, 1996.

[71] *World inflation rate 1981-2022. URL: https://www.macrotrends.net/countries/WLD/world/inflation-rate-cpi*. URL: `https://www.macrotrends.net/countries/WLD/world/inflation-rate-cpi`.